Fundamental Investigation of Fuel Cell-based Breath Alcohol Sensors and the Cause of Sensor Degradation in Low-humidity Conditions

By

Laura Prest

A Thesis Submitted in Partial Fulfillment

of the Requirements for the Degree of

Master of Science

In

The Faculty of Science

Material Science

University of Ontario Institute of Technology

August 2011

Abstract

The goal of this research project was to characterize the physical and electrochemical properties of a commercially available fuel cell-based breath alcohol sensor. Characteristics of the existing sensor were compared with state of the art power generating fuel cells with the goal of understanding the factors that limit performance, lifetime and cost effectiveness of the sensors. This will guide the development of the next generation of breath alcohol sensors.

The average lifetime of the current sensor falls short of the industry standards. In particular, sensors operating in dry conditions experience more rapid loss of sensitivity and failure. Two primary causes of degradation were investigated in this study. Loss of proton conductivity as a result of membrane dehydration was shown to be reversible by rehydrating the membrane in humid conditions. Loss of electrochemically active surface area of Pt is irreversible and seems to be caused by a change in sensor morphology after long-term exposure to dry conditions.

Keywords

Breath alcohol sensor, direct alcohol fuel cell, electrochemically active surface area, proton conductivity, degradation

Acknowledgements

First, I would like to express my deep appreciation to Dr. Brad Easton for the opportunity to work on this interesting project. Thank you for your patience and guidance. After chatting with you about results I always came out with better understanding and motivation. I would like to thank Andrew Vreugdenhil, Liliana Trevani and Thamara Laredo for your valuable comments and encouragement as members of my supervisory committee.

Thank you to the faculty and students in the UOIT science department who helped make my graduate student experience more fulfilling. Thank you to the Easton lab group for memorable times and many laughs. Special thanks to Jennie and Andy for welcoming me into the group and helping me find my way. Many thanks to Steph and Shumail for rides, chats and surprise giraffes. And to Pat and Steph for delicious meals.

I would like to acknowledge all of the people who kindly trained me on instruments or helped me run samples: Michael Fleischauer at NINT for XRD, Ruiyao Wang at Queen's University for XPS, Jeffrey Powell at Trent University for BET, Debbie Lietz at Trent University for TEM, Mike Allison for ICP-OES and FT-IR, Andy Pedersen for SEM and EDS and Donald McGillivray for Raman spectroscopy.

I would also like to acknowledge an NSERC Alexander Graham Bell CGS-M scholarship and the rest of the funding that made this research possible.

Most of all I would like to thank my family for their love and support. You have always been there for me through discouraging circumstances and to celebrate with me when things are going well. I love you so much.

Table of Contents

List of Tables

List of Figures

List of Abbreviations and Symbols

A.C. – Alternating Current

BAC – Blood Alcohol Concentration

BET – Brunauer-Emmett-Teller

$B_{2\theta}$ – full width of peak at half maximum height

CFP – Carbon Fiber Paper

CV – Cyclic voltammogram

d – particle diameter

DAFC – Direct Alcohol Fuel Cell

D.C. – Direct Current

E – potential

E° – reversible fuel cell potential at standard conditions

ECSA – Electrochemically Active Surface Area

EDS – Energy Dispersive X-ray Spectroscopy

EIS – Electrochemical Impedance Spectroscopy

EW – Equivalent Weight

F – Faraday constant

FTIR – Fourier Transform Infrared spectroscopy

GDL – Gas Diffusion Layer

HFR – High Frequency Resistance

I – current

ICP-OES – Inductively Coupled Plasma – Optical Emission Spectroscopy

IPA – Isopropyl alcohol

IR – Infrared

l – membrane thickness

LSV – Linear Sweet Voltammetry

n – moles

MEA – Membrane Electrode Assembly

OCP – Open Circuit Potential

$P_{products}$ – partial pressure of product species

$P_{reactants}$ – partial pressure of reactant species

PEEK – poly(arylene ether ether ketone)

PEM – Proton Exchange Membrane or Polymer Electrolyte Membrane

PEMFC – Proton Exchange Membrane Fuel Cell

PFSA – Perfluorosulfonic Acid

PTFE – Polytetrafluoroethylene

PVC – Polyvinyl Chloride

R_g – ideal gas constant

R – resistance

R_c – contact resistance

R_m – membrane ionic resistance

RH – Relative Humidity

SEM – Scanning Electron Microscopy

T – temperature

TEM – Transmission Electron Microscopy

TGA – Thermogravimetric Analysis

XPS – X-ray Photoelectron Spectroscopy

XRD – X-ray Diffraction

Z’ – real impedance

Z” – imaginary impedance

σ_{H+} – proton conductivity

μ_{H+} – proton mobility

λ – wavelength

ρ – resistivity

θ – scattering angle

ω – frequency

Chapter 1 - Introduction

1.1 Introduction to Breath Alcohol Testing in Canada

A legal limit for ethanol concentration in a driver's blood was added to the Criminal Code of Canada (Section 235) in December 1969. Since then it has been illegal in Canada to operate a motor vehicle with a blood alcohol concentration (BAC) greater than 0.08, which is equivalent to 80 mg of ethanol per 100 mL of blood. The law also gives police the authority to perform mandatory roadside breath alcohol tests using approved devices. Approved screening devices are used to look for the presence of alcohol in a subject's breath in order to determine whether there are reasonable grounds for evidential testing. Evidential testing is a more thorough and accurate procedure involving calibrations, blank samples and more rigorous testing devices. Evidential tests typically take place at a police station and are required for conviction in a court of law; roadside screening tests are inadmissible.

Breath alcohol testing can be used to determine BAC because there is a well established ratio of 2100:1 between the concentration of ethanol in blood and the concentration of ethanol in the alveolar air deep inside the lungs.[1, 2] Breath alcohol testing is much more convenient and less invasive than blood sampling. There have been several generations of breath alcohol testing devices used in Canada over the years, for which a complete review is provided by Wigmore and Langille.[3]

Infrared (IR) spectrometry is the primary technology for evidential testing because it is presently the most accurate method. However, IR-based devices tend to be more expensive and less portable than other devices. As a result, they are not well suited to road-side breath alcohol screening tests.

The original screening devices were n-type semiconductors which relied on the change in electrical conductivity of iridium palladium wires in the presence or absence of ethanol in a breath sample.[3] This technology was found to be unreliable for breath alcohol testing because of interference from other organic species commonly present in breath, particularly acetone. Consequently, the n-type semiconductor device was removed from the list of approved screening devices in 1994 by the Attorney General of

Canada.[4] Since then it has been replaced by fuel cell-based breath alcohol sensors as the primary screening device in Canada.[3]

Fuel cell-based breath alcohol sensors are widely used in Canada and around the world. They are used in vehicle interlock systems and as roadside breath alcohol screening devices used by law enforcement officers. Fuel cell-based sensors are also used in the newest generation of approved evidential devices which combine IR technology and electrochemical sensors. If a person has consumed alcohol within 15 minutes prior to a breath test, their breath will likely contain 'mouth alcohol', causing an erroneously high result.[4] Mouth alcohol is characterized by a dramatic decrease in the ratio of ethanol to CO_2 over the course of exhalation. IR spectrometry is used to detect mouth alcohol by monitoring the relative concentrations of ethanol and carbon dioxide (CO_2) in a breath sample as the subject exhales.[3] The actual ethanol concentration in the breath sample is measured by the fuel cell sensor. These applications require breath alcohol sensors that are straight forward to use and give rapid results.[5] The sensors are also required to operate in a wide range of temperature and humidity conditions depending on geographic location and seasonal variations.

1.2 Proton Exchange Membrane Fuel Cells

Electrochemical breath alcohol sensors are an interesting application of fuel cell technology. Fuel cells are primarily designed and used for electric power generation. A fuel cell is a device that directly converts chemical energy in a fuel into electrical energy by means of an electrochemical process. The oxidation and reduction half reactions are physically separated by an electrolyte to prevent mixing of reactants. Rather than electrons being exchanged directly between reactants, the electrons are transferred from the anode to the cathode through an external circuit where they can be harnessed as electrical energy to power a device. This is similar to a battery except a battery contains stored electrochemical potential energy whereas a fuel cell requires a continuous supply of reactants and removal of products.

There are many variations of fuel cell technology. Fuel cells are typically characterized by their electrolyte and the most well known is the hydrogen-oxygen proton exchange membrane fuel cell (PEMFC). The electrolyte in a PMFC is the proton exchange membrane (PEM), also known as a polymer electrolyte membrane. Figure 1.1 is a schematic of a typical hydrogen-oxygen PEMFC. Hydrogen gas is fed into the anode side through the gas diffusion layer (GDL). Hydrogen is oxidized at the anode, generating protons and electrons as shown in equation 1.1.

$$H_2 \rightarrow 2H^+ + 2e^- \qquad \text{Equation 1.1}$$

Protons are driven across the membrane by a proton concentration gradient that decreases moving from the anode to the cathode. Electrons are driven to minimize their potential energy by forming lower-energy products at the cathode. The electrons must travel to the cathode through an external circuit because the membrane is electrically insulating. Air or oxygen gas is supplied to the cathode through another GDL. At the cathode, oxygen is reduced by combining with protons and electrons to produce water as shown by equation 1.2.

$$O_2 + 4H^+ + 4e^- \rightarrow 2H_2O \qquad \text{Equation 1.2}$$

A fuel cell is a galvanic cell, meaning spontaneous oxidation-reduction (redox) reactions take place at the electrodes. This is in contrast to an electrolytic cell which requires an input of electrical energy to drive the reaction. In both types of cells the anode is where the oxidation reaction takes place. The anode of a galvanic cell is negatively charged since it is the source of electrons and the cathode is positive. As the electrons flow from the anode to the cathode in the external circuit, protons cross the PEM from the anode to the cathode.

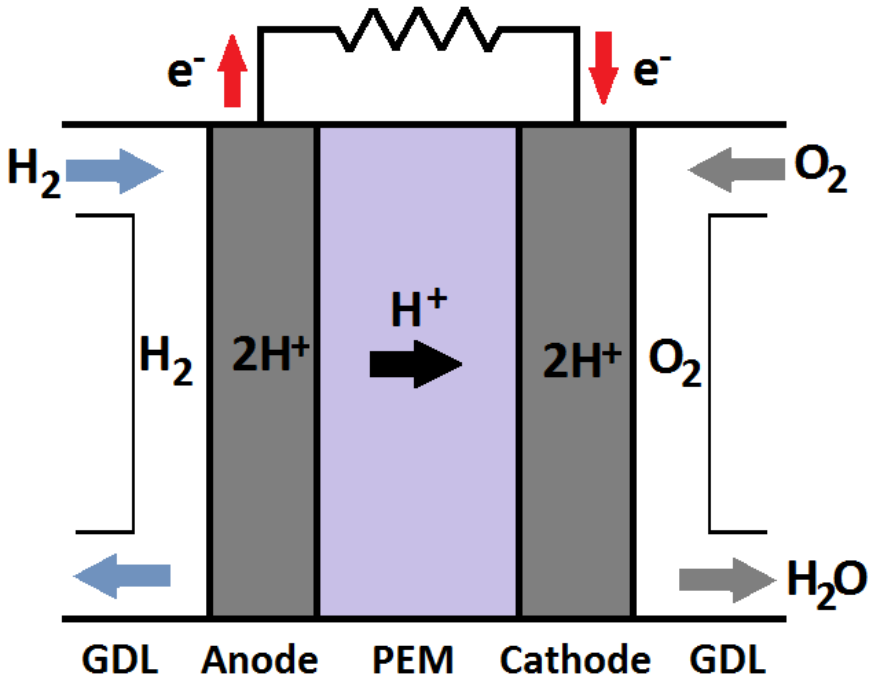

Figure 1.1: Schematic diagram of a proton exchange membrane fuel cell

The power output of a fuel cell power is the product of the cell voltage and current, P=V*I. Therefore, it is desirable to maximize the current and voltage output of a power generating fuel cell. The Nernst equation gives the theoretical maximum open circuit potential (OCP) that can be achieved by a fuel cell.[6] Equation 1.3 is the Nernst equation where E° is the reversible potential of the fuel cell at 1 atm and temperature T, R_g is the ideal gas constant, n is the number of electrons participating in the reaction, F is the Faraday constant (the charge of one mol of electrons, 9.64852 x 10^4 $Cmol^{-1}$), $P_{reactants}$ is the partial pressure of reactant species and $P_{products}$ is the partial pressure of product species. This form of the Nernst equation assumes the fuel cell is operating at relatively low pressures, which is applicable for fuel cell-based breath alcohol sensors.[6]

$$E = E^o + \frac{R_g T}{nF} ln \frac{P_{reactants}}{P_{products}} \qquad \text{Equation 1.3}$$

Fuel cells do not actually operate at the OCP predicted by the Nernst equation. There are three main sources of potential losses that lower the actual voltage of an operating fuel cell. At low current densities the activation energy of the electrochemical

reactions causes slow electrode kinetics leading to a reduction of the cell potential from its ideal value. This is referred to as activation losses. Mass-transport losses occur at higher current densities when reactants or products cannot permeate through the electrodes quickly enough to sustain the fast rate of current production. At typical operating potentials the dominant source of potential loss is ionic resistance in the membrane. This is referred to as Ohmic loss because it obeys Ohm's law; $\Delta V=IR$ where I is the current flowing through the cell and R is overall resistance of the cell, leading to a reduction, ΔV, of the overall cell potential. Ohmic losses also include electronic resistance in the electrodes, but the contribution is very small compared to the ionic resistance of the membrane. The magnitude of the Ohmic loss increases as current density increases.

1.3 Direct Alcohol Fuel Cells

Fuel cell-based breath alcohol sensors are based on direct alcohol fuel cell (DAFC) technology. DAFCs are PEMFCs which use alcohol rather than hydrogen as the fuel. However, rather than powering a portable device, a breath alcohol sensor generates a current signal that is calibrated to indicate the BAC of a breath sample. A schematic diagram of the membrane-electrode assembly (MEA) for DAFC is shown in Figure 1.2. The PEM is sandwiched between two gas diffusion electrodes containing platinum (Pt) catalyst.

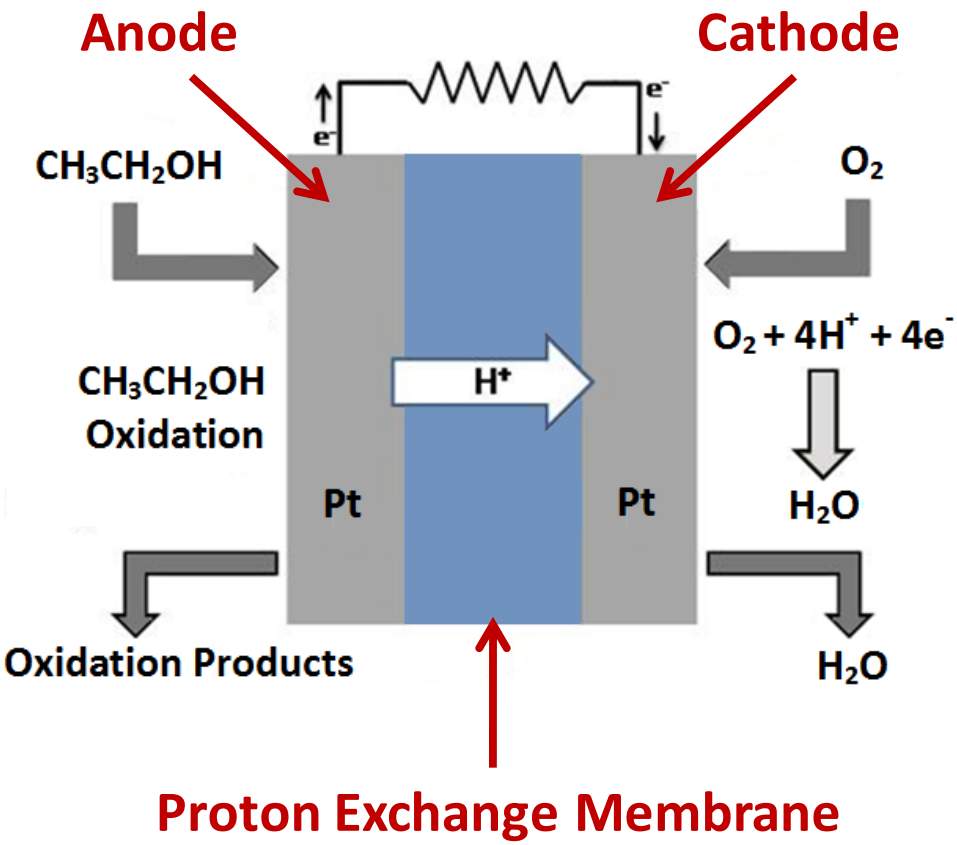

Figure 1.2: Schematic diagram of a direct alcohol fuel cell (DAFC)

The ethanol oxidation reaction is complex and generates a mixture of oxidation products including acetaldehyde, acetic acid and carbon dioxide according to reactions 1.4, 1.5 and 1.6 respectively. However, the major oxidation product of ethanol on a Pt electrode is acetic acid.[7, 8]

$$CH_3CH_2OH \rightarrow CH_3CHO + 2H^+ + 2e^- \qquad \text{Equation 1.4}$$

$$CH_3CH_2OH + H_2O \rightarrow CH_3COOH + 4H^+ + 4e^- \qquad \text{Equation 1.5}$$

$$CH_3CH_2OH + H_2O \rightarrow CO_2 + 12H^+ + 12e^- \qquad \text{Equation 1.6}$$

The electrons travel through the external circuit to the cathode. Protons permeate through the PEM from the anode to the cathode. The sensor cathode is contained within a closed compartment containing air. Oxygen reacts with protons and

electrons at the cathode surface, generating water as a by-product according to the equation 1.2 as described above for PEMFCs.

$$O_2 + 4H^+ + 4e^- \rightarrow 2H_2O \qquad \text{Equation 1.2}$$

1.4 Fuel Cell-based Breath Alcohol Sensors

Fuel cell-based breath alcohol sensors contain a DAFC MEA. Figure 1.3 depicts a commercially available breath alcohol sensor and a fuel cell MEA that has been removed from the sensor cell. The plastic cell consists of two fuel compartments separated by the MEA. The cathode compartment is on the top and contains air as a source of O_2. The anode compartment on the bottom of the cell has two inlet tubes. One tube connects to a pump which draws a fixed volume of breath into the anode compartment through the other tube. There are two platinum wires visible on the right side of the cell. The other end of each wire is in contact with the anode or cathode of the MEA inside the cell. The wires are used to electrically connect the cell to an external device.

Figure 1.3: Commercially available breath alcohol sensor (on the left) and the fuel cell MEA that has been removed from a sensor cell (on the right)

Fuel cell-based breath alcohol sensors can be operated as amperometric or voltammetric devices. Voltammetric operation requires connecting the sensor in series with a fixed load resistance and measuring the induced voltage when a breath sample is supplied.[9] The amperometric mode of operation requires the sensor to be held at a fixed potential such as 0.9 V vs. RHE so that ethanol oxidation will take place. The induced current is measured when a breath sample is provided.[7] A fixed volume of breath is passed into the anode compartment of the sensor. If there is ethanol present in the breath sample the ethanol will be oxidized on the Pt surface in the anode. The

number of electrons (charge) generated at the anode is proportional to the ethanol concentration in the sample. The signal response is calibrated against BAC calibration standards so that the output of the sensor device is a BAC based on either limiting current or total charge. All sensor performance experiments in this study were conducted in amperometric mode and charge was used as the signal.

The goal of this research is to relate the performance of commercially available breath alcohol sensors to the physical properties of the sensor materials. Comparisons will be drawn between the materials used in commercially available breath alcohol sensors and current state of the art PEMFC technology. Materials and structures used in current power generating fuel cells are discussed in detail in the following sections.

1.5 PEM Materials and Properties

1.5.1 Nafion PEMs

The state of the art PEM for power generating fuel cells is Nafion® invented by E. I. du Pont de Nemours & Co.[10] Nafion is a perfluorosulfonic acid (PFSA) polymer with the structure shown in Figure 1.4a. Nafion membranes can be made by melt-extrusion from a powder resin or by casting from a dispersion of the polymer. Membranes with different equivalent weights (EW) can be produced by varying the values of x, y and z. EW is a ratio of the weight of the polymer in grams to the moles of sulfonic acid groups. A higher EW refers to a membrane with a lower degree of sulfonation. Nafion membranes are available with EW ranging from 900 to 1400, however 1100 is the most common. Different thicknesses of Nafion membranes are also manufactured. The most common are 2, 5 and 7 mils, where 1 mil = 0.001 inch = 25.4 μm. Nafion membranes have their own nomenclature which indicates both EW and thickness of a particular membrane. For example, Nafion 112 refers to a membrane with EW of 1100 and thickness of 2 mils.

The hydrophobic perfluorinated carbon backbone of Nafion is based on polytetrafluoroethylene (PTFE or Teflon) shown in Figure 1.4b. This makes Nafion very thermally and chemically stable, electronically insulating and insoluble in water.[10] These

properties are essential for fuel cell membranes. They must be able to operate at 80 °C in the presence of oxidizing and reducing species.[6] It is essential that Nafion provides electronic insulation because otherwise the fuel cell would short circuit. If Nafion were water soluble it would dissolve during fuel cell operation since water is generated at the cathode. Additionally, Nafion has good mechanical strength which allows it to withstand the common stresses experienced by a fuel cell membrane. In an operating fuel cell, the membrane undergoes repeated swelling and contraction as its hydration state changes in varying temperature and humidity conditions.

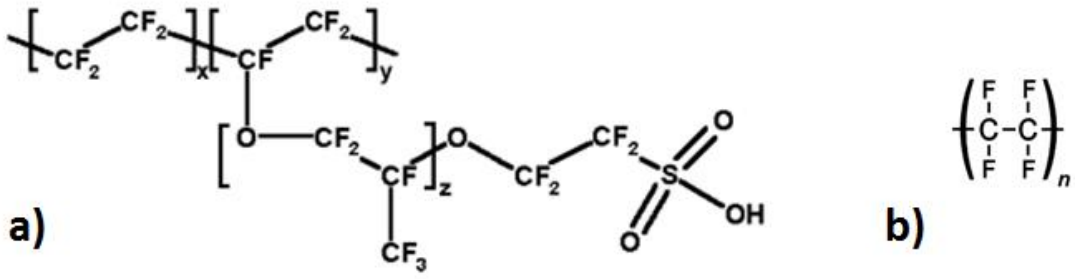

Figure 1.4: Chemical structure of a) Nafion and b) Teflon polymers

In addition to the hydrophobic backbone, Nafion possesses hydrophilic sulfonated side chains. As a result, Nafion membranes undergo nanoscopic phase separation between the backbone and side chains. This creates distinct hydrophobic regions and hydrophilic channels containing a high concentration of sulfonic acid (SO_3^-) groups.[11] In sufficiently humid conditions, the sulfonic acid groups are surrounded by a hydration sphere of water molecules. These water-filled channels containing SO_3^- groups endow Nafion with its high proton conductivity. There are alternative PEMs based on styrene[12], poly(arylene ether)s such as poly(arylene ether ether ketone) (PEEK)[13], poly(imide)s[14], and other materials. Nafion and other PFSA membranes are by far the most commonly used membranes for PEMFCs.[10]

1.5.2 Proton Conductivity in PFSA Membranes

Proton conduction in Nafion membranes is believed to occur via the Grotthuss mechanism. Although there is still debate regarding the exact mechanism, the general

idea is that a proton 'hops' from one water molecule to another along the hydrophilic channels, forming cationic species such as $H_5O_2^+$ or $H_9O_4^+$ along the way.[15] As such, the proton conductivity of a PEM is highly dependent on the water content of the membrane.

Proton conductivity (σ_{H+}) in a PEM is described by equation 1.7 where F is the Faraday constant, $[H^+]$ is the proton concentration in the membrane and μ_{H+} is proton mobility in the electrolyte. Sulfonic acid groups contain exchangeable acid protons. Therefore, increasing the number of sulfonic acid groups in the membrane increases the proton concentration and proton conductivity.

$$\sigma_{H^+} = F[H^+]\mu_{H^+} \qquad \text{Equation 1.7}$$

Overall membrane resistance R is determined by the membrane thickness *l*, cross-sectional area *A*, and resistivity ρ according to equation 1.8. Resistivity is the inverse of membrane proton conductivity and is an intrinsic property of the membrane material. Proton conductivity has units of Scm^{-1} where $1\ S = \Omega^{-1}$. It is clear that membrane resistance can be decreased by reducing the membrane thickness, increasing the cross-sectional area or by increasing the proton conductivity. Membrane thickness and cross-sectional area are fairly fixed. Proton conductivity is the variable with the most room for improvement in most current membrane materials.

$$R = \rho \frac{l}{A} \qquad \text{Equation 1.8}$$

Membrane resistance reduces the overall cell potential by causing internal losses that obey Ohm's law, $\Delta V = IR$. This is referred to as the IR drop in a fuel cell. In a power generating fuel cell the overall cell potential is very important for maintaining a high power output. Conversely, a breath alcohol sensor is not required to generate a large power output. Furthermore, the current generated by a sensor is very small, so the impact of a resistive PEM is reduced.

1.5.2 Drawbacks of Nafion

Although Nafion membranes exhibit excellent proton conductivity when sufficiently hydrated, Nafion begins to dry out and lose proton conductivity at temperatures greater than 80 °C. There is currently research into creating PEM materials that are more resistant to high temperatures and low humidity. A common technique is to prepare composite membranes by adding hygroscopic materials such as SiO_2 (silica) to the pores of Nafion.[16] These membranes have enhanced water uptake at higher temperatures and in lower humidity conditions.[17, 18] However, SiO_2 also partially blocks the pores in Nafion, reducing the proton conductivity.[19] Sulfonated SiO_2 is commonly used in an effort to counteract the reduction in proton conductivity resulting from blocked pores.[18, 20]

Another drawback to Nafion is that it allows ethanol crossover in DAFCs.[21] Ethanol permeates through the water-filled pores of Nafion and becomes oxidized at the cathode. This generates a mixed potential at the cathode, resulting in a reduced cell potential.[22] This issue is mitigated by using thicker membranes such as Nafion 117 in DAFCs rather than Nafion 112 which is typically used in H_2-O_2 PEMFCs. Another strategy is adding SiO_2 into the pores of Nafion to block ethanol molecules from crossing through to the cathode.[23] The thick PEM in commercially available breath alcohol sensors is not expected to exhibit ethanol crossover.

1.6 PEMFC Electrodes

The function of fuel cell electrodes is to facilitate transport of reactants to the catalyst surface to promote the electrochemical reactions. For the electrochemical reactions to take place the catalyst site must be accessible to gas-phase reactants, protons and electrons. These active locations are referred to as the three-phase boundary.[6] Transport of reactants to the three-phase boundary is achieved by the various elements of the electrodes. State of the art fuel cell electrodes consist of a combination of materials including a GDL and a catalyst layer. The GDL is typically Teflon-coated carbon fiber paper (CFP) or carbon cloth. It is responsible for mass

transport of gaseous reactants to the catalyst and water away from the catalyst layer. Water management is important in fuel cell electrodes because too much water causes flooding. Liquid water inhibits gas diffusion to catalyst sites, resulting in mass transport losses. CFP and carbon cloth are electronically conductive and also act as current collectors to transport electrons from the catalyst layer to the external circuit.

1.7 PEMFC Catalysts

Fuel cell catalyst layers are also designed to optimize the three-phase boundary. As shown in Figure 1.5, catalyst layers typically contain catalyst particles dispersed on a carbon support and a proton conducting binding material.[24] Catalyst particles are less active the farther they are from the PEM because it is difficult for protons to migrate through the catalyst layer. For this reason an ionomer is added to extend proton conducting pathways from the membrane to catalyst particles deeper in the catalyst layer. Nafion or similar PFSA polymer materials are the most common but other ionomers are also used.[24] The solubilized ionomer can be added to the catalyst ink before deposition or as a thin film onto existing electrodes.[25-28]

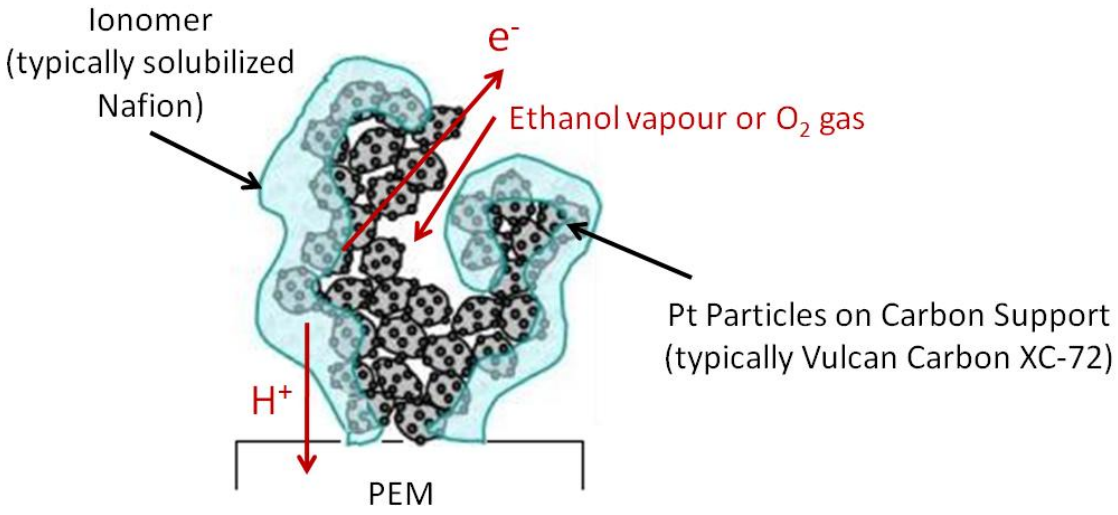

Figure 1.5: Schematic diagram of the structure of a fuel cell catalyst layer containing Nafion ionomer and platinum catalyst particles supported on carbon black

Optimal Nafion loadings in the catalyst layer depend on catalyst loading.[27] For catalyst layers containing 20 wt.% Pt on carbon black, 30-40 wt.% Nafion loading has been shown to be optimal for enhanced proton conductivity, complete wetting of the catalyst by ionomer and gas diffusion.[27-29] Nafion loadings below 30 wt.% are insufficient to make contact with the maximum amount of catalyst surface. Loadings over 45 wt.% block pores and cover catalyst sites, similar to the effects of too much water in the catalyst layer.[24] Ionomer content in the catalyst layer is an important factor in optimizing the catalyst utilization efficiency.

1.7.1 Platinum Utilization and Electrochemically Active Surface Area (ECSA)

Pt is the best catalyst for H_2 oxidation and O_2 reduction; however it is a very expensive metal. The cost of fuel cell electrodes can be greatly reduced by minimizing the mass of Pt required while maintaining the same catalytic activity. % Pt utilization is a measure of how efficiently Pt is used in an electrode and is calculated using equation 1.9. Real surface area of Pt is the amount of Pt surface area that is actually catalytically active and is estimated using cyclic voltammetry. Total surface area of Pt is calculated using the known mass of Pt and average Pt particle size determined by X-ray diffraction and the particles are assumed to be uniformly sized spheres with radius *r* and surface area $4\pi r^2$.[41]

$$\%\ Pt\ utilization = \frac{real\ surface\ area\ of\ Pt}{total\ surface\ area\ of\ Pt} \times 100 \qquad \text{Equation 1.9}$$

Another measure of Pt utilization is the electrochemically active surface area (ECSA). ECSA is a ratio of the real surface area of Pt to the mass of Pt in an electrode, reported in m^2g^{-1}. It is desirable to maximize the % Pt utilization and the ECSA of Pt by reducing the amount of inactive Pt in fuel cell electrodes. As described above, adding a proton conducting ionomer such as Nafion to the catalyst layer has a large impact on improving the % Pt utilization and ECSA.

1.7.2 Pt-based Alloy Catalysts for DAFCs

Complete oxidation of ethanol to CO_2 (reaction 1.6) requires breaking the C-C bond and occurs via several steps involving adsorbed intermediate species.[21] Pt is the most efficient catalyst for C-C bond cleavage, but it is not efficient at catalyzing the subsequent steps.[30] In particular, the final step involves oxidation of CO or CO-like species that are adsorbed on the Pt surface. This requires dissociative adsorption of water on adjacent Pt sites to provide adsorbed hydroxyl (-OH) groups as shown by reaction 1.10. On a pure Pt surface this occurs at potentials above 600 mV vs. reversible hydrogen electrode (RHE). The rest of the ethanol oxidation steps take place at potentials below 400 mV.[31] Therefore, CO-like intermediates tend to stay strongly adsorbed on Pt sites, poisoning the catalyst.[2, 5] In contrast, various Pt alloys have been shown to promote electro-oxidation of adsorbed CO to CO_2 by adsorbing hydroxyl groups at lower potentials.[32, 33]

$$Pt + H_2O \rightarrow Pt - OH + H^+ + e^- \qquad \text{Equation 1.10}$$

Many binary, ternary or quaternary Pt-based alloys have been investigated for their effectiveness at oxidizing ethanol. The most common catalysts for DAFC anodes are bimetallic PtSn and PtRu alloys.[34] In a study comparing PtSn, PtRu, PtMo and Pt electrocatalysts for DAFCs, PtSn and PtRu were both superior to Pt, with PtSn giving the best performance.[33]

1.8 Thesis Objectives

This study aims to investigate the fundamental relationships between physical and electrochemical properties and overall sensor performance and operational lifetime. Ultimately, the goal of this work is to identify modifications that could be made to improve the existing sensor or materials that could be used to develop the next generation of fuel cell-based breath alcohol sensors. Commercially available electrochemical breath alcohol sensors are based on PEMFC technology developed more than 30 years ago.[7, 35] Significant improvements have been made in power generating fuel cell materials in the past 20 years.[6, 16] Some of those advancements

could be implemented into the current breath alcohol sensors to make them more sensitive, durable and/or cost-effective. Improvements may include replacing the membrane and electrodes with materials commonly used in power generating fuel cells.

In practice, commercially available breath alcohol sensors on the market today are not meeting the ever growing industry standard for operational lifetimes. The sensors are expected to last 5-7 years before needing to be replaced. However, the sensor lifetimes typically range from 2-5 years depending on the location of their use. In particular, sensors that are assembled or used in low-humidity conditions tend to lose sensitivity and fail more quickly. Since replacing failed sensors is expensive and inconvenient, manufacturers are faced with the challenge of improving the operational lifetimes of the current sensors or designing an entirely new generation of sensors to meet the industry requirements.

This study investigates how the physical properties of a commercially available breath alcohol sensor are affected by environmental conditions such as changing humidity and long-term exposure to dry conditions. We are interested in determining the primary cause of degradation for breath alcohol sensors in dry conditions. It is hypothesized that there are two primary factors that are responsible for the loss of sensitivity: increased ionic resistance of the membrane caused by membrane dehydration and loss of ECSA of Pt resulting from morphology changes in the electrodes. Ionic resistance of the membrane was monitored using EIS and ECSA of Pt was estimated using cyclic voltammetry. Sensory performance was evaluated by dose response calibration experiments for sensors at various degrees of membrane hydration. Based on these results, modifications to the sensor composition have been proposed that could lead to the development of the next generation of fuel cell-based breath alcohol sensors.

Chapter 2 - Experimental Techniques and Instrumentation

2.1 Morphology of Sensor Electrodes and PEM

All breath alcohol sensors used in this study were provided by Alcohol Countermeasure Systems.

2.1.1 Optical Microscopy

Optical microscope images were obtained using a National Digital Microscope model DM-0754 with a 0.3 Mega Pixel camera and Motic Images Plus 2.0 software.

2.1.2 Scanning Electron Microscopy (SEM)

SEM micrographs of sensor MEAs were acquired using a JEOL JSM 6400 scanning electron microscope at a working distance of 8 mm and an accelerating voltage of 20 keV. Cross-sectional views of MEAs were obtained after cutting an MEA in half to expose a flat edge. Samples were mounted on Al SEM stubs using double-sided carbon tape.

2.1.3 Transmission Electron Microscopy (TEM)

Catalyst material was harvested from a sensor and sonicated in a small volume of dichloromethane (anhydrous, 99.8%, Sigma-Aldrich) for 30 minutes. This mixture was transferred to a micro-centrifuge tube and centrifuged for ten minutes. The liquid was decanted from the tube, leaving the wet catalyst material at the bottom of the tube. A pipette was used to deposit a small drop of the wet catalyst material onto a Formvar carbon-coated 300-mesh copper grid. The copper grid was cleaned first by dipping twice in methanol (Fisher Scientific) and letting it dry. TEM images were obtained using a JEOL 100CX STM microscope with a 3.25 by 4 inch plate film. 5’ x 7’ pictures were developed from negatives at a resolution of 200 dpi.

2.1.4 X-ray Diffraction (XRD)

Powder XRD was used to estimate the average size of Pt particles in the sensor electrodes. The catalyst layer was harvested from a fresh sensor and rinsed multiple times with water and acetone (Fisher Scientific) prior to being made into powder. XRD spectra were acquired using a Bruker D8 diffractometer with a Cu Kα X-ray source. The Scherrer equation was used to calculate particle size from the spectral line broadening.

2.1.5 Brunauer-Emmett-Teller (BET) Surface Area

BET surface area analysis was performed on catalyst material harvested from a fresh sensor. The instrument was a Gemini VII 2390 Surface Area Analyzer. The sample was degassed under vacuum overnight before collecting the BET measurement.

2.2 Material Characterization Techniques

2.2.1 Energy Dispersive X-ray Spectroscopy (EDS)

EDS was used to investigate the elemental compositions of sensor materials. The accelerating voltage was 20 keV and the working distance was 25 mm. In EDS a sample is bombarded with a beam of high-energy electrons, causing an electron to be emitted from an orbital. That orbital is then filled by an electron from a higher-energy orbital and a characteristic X-ray is emitted and detected. EDS was performed using the scanning electron microscope with a VG instruments EDS detector.

The sensor membrane was investigated using a cross-sectional piece of MEA. The electrodes were studied using a small cross-sectional piece of an MEA mounted on an SEM stub with the electrode side exposed to the electron beam.

2.2.2 X-ray Photoelectron Spectroscopy (XPS)

X-ray photoelectron spectroscopy (XPS) was used to analyze catalyst material harvested from sensor MEAs. A scalpel was used to scrape catalyst material from an MEA without removing the gold layer between the catalyst layer and the membrane. Harvested catalyst material was pressed onto double-sided copper tape on an XPS stub. All XPS spectra were collected by a Thermo Instruments 310-F Microlab spectrometer with a monochromatic Mg Kα (hv=1253.6 eV) X-ray source. Peaks were fitted using optimized Gaussian-Lorentzian curves and a Shirley background.

2.2.3 Thermogravimetric Analysis (TGA)

Thermogravimetric analysis (TGA) was performed using TA Instruments Q600 SDT thermal analyzer controlled by QSeries software. Samples were heated in alumina pans from room temperature to 1000°C at a heating rate of 20°Cmin^{-1}. The atmosphere

in the furnace was either extra dry air (Praxair) or argon (99.999%, Praxair) flowing at 50 $mLmin^{-1}$. Data processing was done using TA Universal Analysis software.

2.2.4 Inductively Coupled Plasma-Optical Emission Spectroscopy (ICP-OES)

Inductively coupled plasma-optical emission spectroscopy (ICP-OES) is an optical atomic spectrometric technique. Argon plasma is used to convert the sample into gaseous atoms or ions and to thermally excite valence electrons to higher energy states. When an excited electron relaxes back to the ground state, a photon with a characteristic wavelength is emitted. The number of photons emitted at the characteristic wavelength of a particular element is proportional to the concentration of that element in a sample.

ICP-OES was performed to obtain the weight loadings of platinum and gold in the commercially available sensors. Two sensor MEAs were individually digested overnight in approximately 15 mL of aqua regia. Aqua regia was prepared by mixing hydrochloric acid (HCl, ACS-Pur, Fisher Scientific Canada) with nitric acid (HNO_3, ACS reagent grade, 70%, Sigma-Aldrich) in a 3:1 ratio by volume. The metals completely dissolved in aqua regia resulting in orange-coloured metal solutions and leaving the insoluble membranes and white flakes of catalyst binder. The metal solutions were filtered through Wattman 42 filter paper and then diluted in 250.0 mL volumetric flasks to obtain appropriate concentrations of gold. The samples were further diluted in the ratio 1:50 to reduce the Pt concentration into the 0-20 mgL^{-1} range. A blank aqua regia solution was also filtered and diluted to the same concentration.

A series of mixed platinum and gold standard solutions in the concentration range 1 to 20 mgL^{-1} were prepared by diluting a platinum ICP standard (1000 mgL^{-1} Pt in 10% HCl, Assurance) or a gold ICP standard (1000 mgL^{-1} Au in 3% HCl, Spectropure). Calibration curves were prepared by analyzing the series of prepared standard solutions. All measurements were performed using a Varian Vista-MPX (CCD Simultaneous ICP-OES). The characteristic wavelengths investigated were 214.424 nm for Pt and 242.794

nm for Au. All measurements were performed in triplicate and the average concentration was calculated for each metal.

2.2.5 Fourier Transform Infrared Spectroscopy (FTIR) and Raman Spectroscopy

A Thermo Nicolet Avatar 370 DTGS equipped with Smart Performer ATR was used to collect IR spectra. Raman spectra were collecting using a custom Renishaw Raman microscope with argon ion (514 nm) laser. Samples were placed on a glass slide for Raman analysis or directly onto the germanium crystal for FT-IR analysis. FT-IR spectra were acquired using 20 scans and Raman spectra were collected using 40 scans.

2.3 Electrochemical Measurements

Unless otherwise stated, electrochemical experiments were performed in ambient conditions in the laboratory (pressure of 1 atm and temperature of approximately 22 °C).

2.3.1 Ethanol Oxidation Activity of Harvested Catalyst Material

A catalyst 'ink' was prepared by harvesting approximately 11 mg of catalyst material from a sensor MEA. An analytical balance was used to find the weight of catalyst material to a precision of 0.0001 g. The catalyst material was mixed with 400 µL of a 50% aqueous solution of isopropyl alcohol (IPA, histological grade, Fisher Scientific) and 100 µL of 5% Nafion dispersion (1100 EW, 5% wt. in alcohols, Ion Power Inc.). Note that this Nafion loading corresponds to 30 wt. % Nafion in the resulting ink deposits. The purpose of adding Nafion solution to the catalyst ink was to increase adherence of the catalyst material to the glassy carbon electrode. The mixture was mixed ultrasonically (Fisher Scientific, 42 kHz) for 30 minutes to create a homogeneous ink suspension.

Linear Sweep Voltammetry (LSV) was performed using the three-electrode glass mini cell shown in Figure 2.1. A high precision syringe (Hamilton) was used to deposit a 2 µL drop of ink onto a 3 mm glassy carbon working electrode (CH Instruments). A Pt wire counter electrode (0.5 mm diameter, CH Instruments) was used to generate applied potentials at the working electrode. The current generated at the working electrode was

monitored using a Ag/AgCl reference electrode (1.0 M KCl electrolyte, porous Teflon tip, CH Instruments). Linear sweep voltammograms were obtained in 0.5 M sulfuric acid and 0.5 M sulfuric acid + 1.0 M ethanol solution. The electrolyte solutions were prepared by diluting sulfuric acid (Fisher Scientific) and ethanol (95%, Commercial Alcohols Inc.). All solutions were purged by bubbling N_2 for at least ten minutes. An SI 1286 Electrochemical Interface with CorrWare 3.2c software was used to conduct the measurements. The applied potential at the working electrode was increased from 0 mV to 1200 mV vs Ag/AgCl at a sweep rate of 50 mVs^{-1}.

Given the poor conductivity of ethanol, the voltammogram in ethanol was obtained by subtracting the voltammogram in sulfuric acid from the voltammogram in sulfuric acid + ethanol. Sulfuric acid was required to form an electrolyte solution.

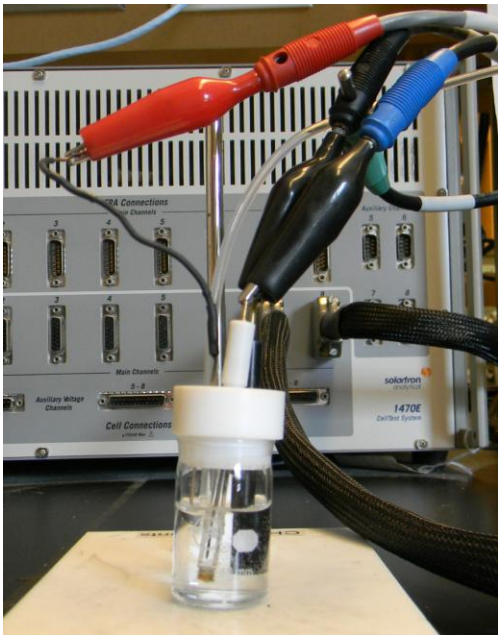

Figure 2.1: Half-cell setup for CV and LSV experiments including glassy carbon working electrode, Pt wire counter electrode and Ag/AgCl reference electrode immersed in N_2–purged 0.5 M sulfuric acid solution

2.3.2 Cyclic Voltammetry of Harvested Catalyst Material

Catalyst inks were prepared using the procedure described in 2.2.1 and the same electrochemical cell setup was used. A series of ink deposits (2-6 µL) were made onto glassy carbon working electrodes and allowed to dry for 30 minutes. Cyclic voltammograms (CVs) were obtained while the electrodes were immersed in 0.5 M sulfuric acid. The applied potential at the working electrode was cycled between -280 mV and 1200 mV vs. Ag/AgCl at a sweep rate of 100 mVs^{-1}.

2.3.3 Electrochemical Impedance Spectroscopy (EIS) Measurements of Ionic Resistance of Sensor Membranes

Impedance refers to the total opposition to the flow of current in an A.C. circuit. EIS is used to separate the real impedance (resistance) from the imaginary impedance (capacitance) in a fuel cell. The total impedance of a fuel cell contains contributions from several sources as shown by Figure 2.2. Imaginary impedance corresponds to capacitance (C_1 and C_2) resulting from an electric double layer at the catalyst-electrolyte interface in both electrodes. Capacitance is assumed to be uniformly distributed throughout an entire electrode.[36]

The real impedance has several components: contact resistance (R_c), which is the resistance of the connecting wires and contact between the wires and electrodes, resistance in the catalyst layers (R_1 and R_2) and the ionic resistance of the membrane (R_m). The resistance in the catalyst layers results from a combination of electronic and ionic resistance where ionic resistance refers to how easily protons are able to travel from Pt sites in the catalyst layer to the membrane. The electronic resistance is negligible compared to the ionic resistance. The major contribution to the real impedance is R_m.

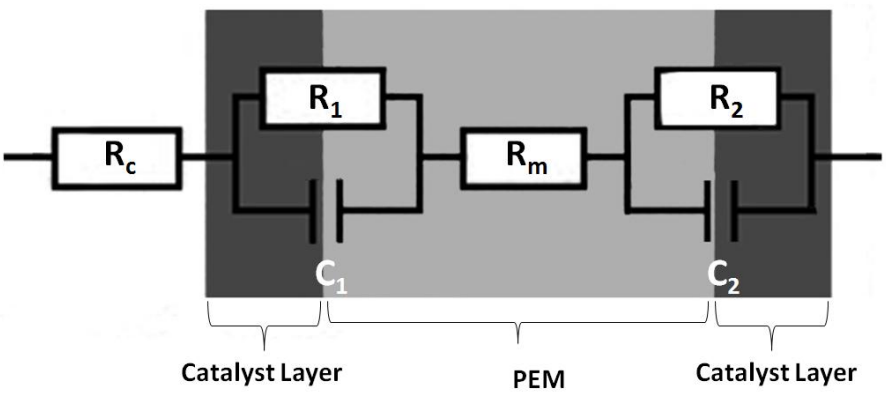

Figure 2.2: Representation of the sources of electrochemical impedance in a fuel cell. R_c is contact resistance, R_1 and R_2 are electronic and ionic resistance in the catalyst layers, C_1 and C_2 are capacitance due to electric double layers at the electrode-electrolyte interface and R_m is ionic resistance of the PEM.

EIS was used to monitor the ionic resistance of the membrane under different hydration conditions. A Solartron SI 1260 Impedance Analyzer was used in combination with a Solarton 1470 E multichannel potentiostat and Multistat 1.1d software (Scribner Associates Inc.). A constant D.C. bias of 0.0 V vs. OCP was applied across a sensor and a small A.C. perturbation was applied with amplitude of 5 mV. The frequency of the A.C. potential is scanned from high to low frequency over the range 0.1 Hz to 100 kHz and the resulting current is measured. The D.C. limit is achieved as the A.C. frequency approaches infinity. Under this condition the imaginary impedance is zero because the resistance of a capacitor is zero in a D.C. circuit. Therefore, at the high-frequency limit, the impedance is dominated by the ionic resistance of the membrane.

The result of an EIS measurement is displayed as a Nyquist with real impedance (Z') on the x-axis and imaginary impedance (Z") on the y-axis. The Nyquist plots for the breath alcohol sensors tested were nearly-vertical lines, similar to that shown in Figure 2.3. ZView software (Scribner Associates Inc.) was used to apply a line of best fit to the Nyquist plot in order to extrapolate the high frequency resistance (HFR). The HFR is given by the intercept with the real impedance axis and is assumed to be the ionic resistance of the sensor membrane.

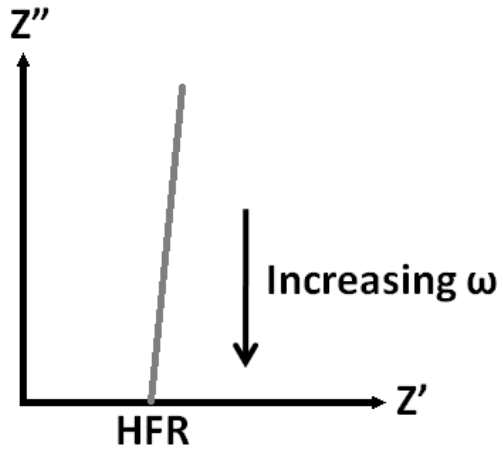

Figure 2.3: Simple Nyquist plot demonstrating the high frequency resistance

2.4 Accelerated Humidity Cycling of Sensor Membrane

2.4.1 Water Uptake of MEA Equilibrated in a Controlled Humidity Chamber

The MEA was removed from a sensor that had been stored for several months in ambient conditions in the laboratory. The original weight of the MEA was measured at 22 °C and relative humidity (RH) of less than 20%. The MEA was placed in an ESPEC SH-241 bench-top temperature and humidity chamber at 42% RH and a constant temperature of 25°C. The MEA was allowed to equilibrate under those conditions for 12 hours and then its weight was recorded. The RH setting was increased to 50% and then from 50% to 90% in increments of 10%. The weight of the MEA was recorded after equilibrating at each RH for 12 hours. The RH was then decreased from 90% to 40% in increments of 10% and the weight of the MEA was again recorded after equilibrating for 12 hours at each interval. After completing the hydration-dehydration cycle at a constant temperature of 25°C, the temperature was increased to 37°C. The initial RH was set to 40% and the same procedure was repeated.

2.4.2 Accelerated Membrane Dehydration Cycling by Equilibrating the Sensor in a Controlled Humidity Chamber

Three sensors of various ages (made in 2004, 2007 or 2010) were placed in the humidity chamber at 30% RH and a constant temperature of 25 °C. The sensors were allowed to equilibrate under those conditions for 12 hours. Each sensor was individually removed from the humidity chamber and EIS was used to measure the membrane resistance. The sensors were returned to the humidity chamber and the RH setting was increased to 40%. This process was repeated, increasing the RH by 10% increments up to 90% and the final increase was up to 95%. The RH was then decreased back to 90% and then in increments of 10% back to 50%. The membrane resistance of each sensor was measured after equilibrating for 12 hours at each setting.

2.4.3 Accelerated Membrane Dehydration by Flowing N_2 through the Sensor after Hydrating in Humidity Chamber

In the previous experiments the membrane hydration was cycled by equilibrating a sensor or MEA in a humidity chamber for 12 hours at fixed temperature and RH. In this experiment the sensor is hydrated by equilibrating in the humidity chamber and dehydrated by flowing dry N_2 through the anode compartment of the sensor.

Short-term accelerated membrane dehydration cycling was performed over the course of two successive days. A sensor was pre-conditioned by equilibrating for 24 hours at 25 °C and 95% RH in the bench-top temperature and humidity chamber. On the first day of measurements the sensor was removed from the humidity chamber and an EIS measurement was made immediately. Dry N_2 (99.998%, Praxair) was then passed through the anode compartment continuously for 100 minutes while making periodic EIS measurements to monitor the ionic resistance of the membrane. After 100 minutes the sensor was returned to the humidity chamber to equilibrate for 24 hours again at 25 °C and 95% RH. The next day the sensor was removed from the humidity chamber and the procedure from day 1 was repeated.

2.4.4 Accelerated Membrane Hydration-Dehydration Cycling by Flowing N_2 through the Sensor

In this experiment the membrane hydration was manipulated by flowing dry or humidified N_2 through the sensor rather than equilibrating the sensor in the humidity chamber. Longer term accelerated membrane dehydration cycling was done over a period of ten days. Seven hydration-dehydration cycles were performed by alternating between flowing dry or humidified N_2 through the sensor anode compartment. The schematic in Figure 2.4 shows the experimental setup for accelerated membrane dehydration cycling. A gas line from the N_2 cylinder was split using a 3-way valve. One side of the 3-way valve led directly to a flow meter to deliver dry N_2. The other side flowed through a water bubbler to humidify the N_2 before reaching the flow meter. The gas feed could be easily switched between dry and humidified gas by simply toggling the 3-way valve. During measurements the flow meter was set to a constant flow rate of 85 $mLmin^{-1}$ for dry N_2 and 100 $mLmin^{-1}$ for humidified N_2. The two different flow rates were a consequence of the presence of the bubbler and not intended for any particular reason.

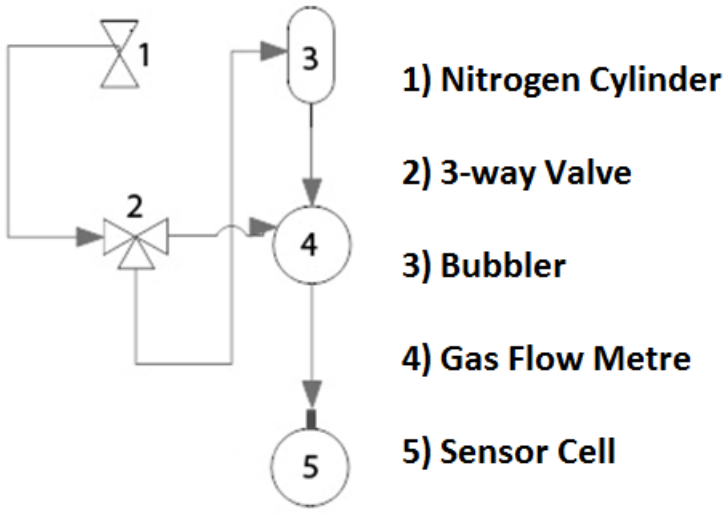

Figure 2.4: Schematic diagram of the experimental setup for accelerated membrane dehydration cycling using flowing N_2

The initial membrane resistance of a fresh sensor was measured using EIS. The membrane was then fully hydrated by flowing humidified N_2 with EIS measurements every three minutes. Once the HFR stabilized at its fully hydrated value, the gas flow was switched to dry N_2 to dehydrate the membrane. Membrane resistance was monitored using EIS while simultaneously flowing dry or humidified N_2 gas through the sensor.

Five cycles were performed in which the membrane was consistently dehydrated to a HFR of approximately 9 Ω and then rehydrated to a stable, fully-hydrated value. In the sixth cycle the membrane was dehydrated to quite a large value of 86 Ω before being rehydrated. For the seventh cycle the sensor was allowed to become extremely dehydrated, resulting in a HFR value of approximately 15800 Ω. The sensor was rehydrated again and then placed in an oven overnight at 55 °C. EIS was then used to measure the HFR after drying out the membrane in the oven overnight.

2.5 Dose Response Calibrations to Evaluate Sensory Performance

The performance of a series of sensors was evaluated using 'dose response' calibrations. An SI 1286 Electrochemical Interface with CorrWare 3.2c (Scribner Associates Inc.) software was used to collect the measurements. The sensor was operated in 2-electrode mode with the ethanol side as the working electrode while the oxygen side served as the counter and reference electrode. A constant potential of 500 mV was applied to the ethanol working electrode and the current between the electrodes was measured continuously. The baseline current was established over a period of 25 minutes before beginning ethanol injections. During this time the cell was held at the constant potential of 500 mV and the anode compartment was open to atmosphere. The magnitude of the baseline current was dependent on the membrane resistance (I=V/R) and varied slightly from one experiment to the next.

Alcohol reference solutions (Alcohol Countermeasure Systems) were diluted to prepare a series of simulated breath samples in which the concentration of ethanol vapour in the headspace above the samples ranged from 0.005 to 0.150 % BAC at 34.0

°C. The breath sample solutions were prepared in glass vials and sealed with parafilm. A 'blank' sample was prepared using distilled water to give a BAC of 0.000. To ensure the desired partial pressure of water vapour in the headspace, the samples were equilibrated in a water bath at 34.0 °C until immediately prior to use. At this temperature, concentration of saturated water vapour in the headspace was very similar to the known concentration of water vapour in human breath at 34°C.[37]

Figure 2.5 is a schematic representation of the experimental setup for dose response calibrations. Simulated breath samples were introduced to the sensor using a solenoid pump (provided by Alcohol Countermeasure Systems) attached to the outlet of the ethanol compartment. Application of 12 V D.C. (Extech Instruments power supply) to the solenoid activated the pump to draw in a set volume of 0.5 mL. A switch was used to alternate between applying 0 V or 12 V to the solenoid pump. The inlet to the ethanol compartment was attached to a short piece of tubing. The other end of the tube was inserted into the headspace of a sealed vial containing an ethanol solution. Each time the pump was activated, 0.5 mL of vapour from the headspace in the vial was drawn through the tubing into the ethanol compartment of the sensor. The current was allowed to reach its peak value and begin to decay before the voltage applied to the solenoid pump was switched back to 0 V. The pump then expelled 0.5 mL to purge the anode compartment in preparation for the next dose injection. The current was allowed to return to its baseline value before injecting the next 'dose'. Each concentration was repeated a minimum of five times before switching to the next sample. Samples were tested in order of increasing BAC to minimize the effect of contamination in the tubing by previous samples.

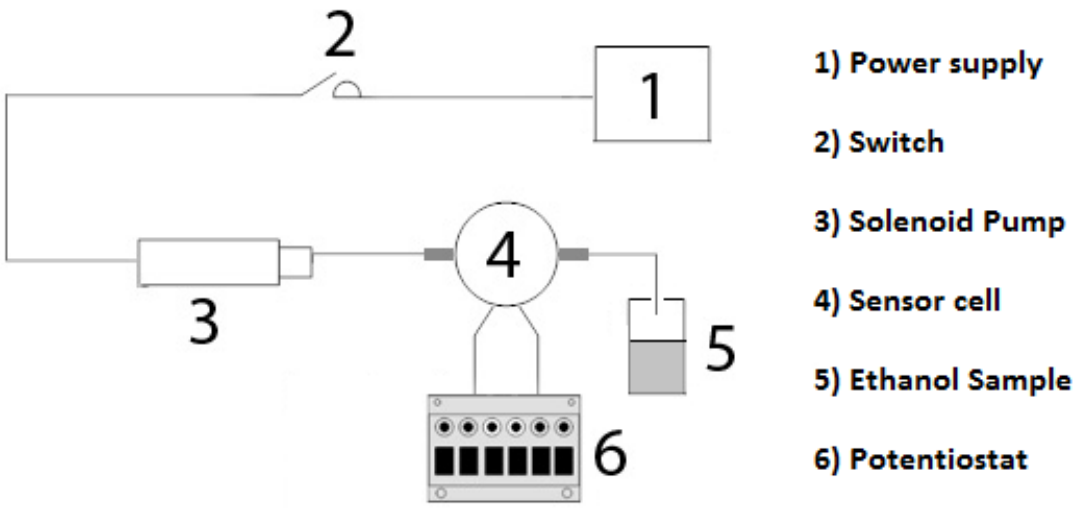

Figure 2.5: Schematic diagram of experimental setup for dose response calibrations

Peak areas were calculated for a minimum of three peaks for each sample to determine the charge produced by oxidation of alcohol at the sensor anode. The average charge for each sample was divided by the average mass of Pt in the anode as determined by ICP-OES. The moles of ethanol injected were calculated using the known concentrations of the ethanol standards and the constant injection volume of 0.5 mL. Sensitivity calibration curves were created by plotting normalized charge vs. moles of ethanol injected. The slope of the line of best fit gave the sensitivity in units of µC of charge produced per gram of Pt in the anode per nanomole of ethanol injected. This value will allow for direct sensitivity comparisons with other commercially available sensor and with new sensors that will be prepared in our lab.

Chapter 3 - Physical Characterization of the Existing Commercially Available Breath Alcohol Sensor

3.1 Morphology of MEA

3.1.1 Cross-sectional View of MEA by Optical Microscopy

Optical microscope images were acquired to show the overall MEA morphology. Figure 3.1 shows a cross-sectional view of a sensor MEA. The PEM is a thick, porous matrix of sintered polyvinyl chloride (PVC) particles.[5] Under ambient conditions the MEA is approximately 1500 µm thick depending on the membrane hydration.

The electrodes on both sides of the PEM consist of a thin layer of gold (Au) beneath a densely packed catalyst layer. The catalyst layer can be harvested by scraping it off with a scalpel without removing the Au sub-layer. The shiny layer of Au is clearly visible on both sides of the membrane once both catalyst layers have been removed. The purpose of the Au layer is likely to provide a barrier to prevent the catalyst layer from penetrating into the porous membrane when the catalyst layer is deposited. The Au layer may also increase the electrical conductivity of the electrode and provide a surface for the catalyst material to adhere to.

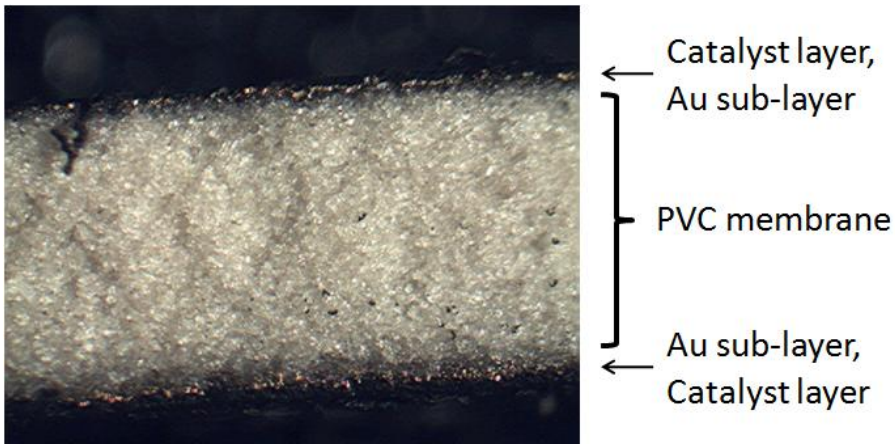

Figure 3.1: Optical microscope image of a breath alcohol sensor MEA cross-section

3.1.2 Scanning Electron Microscopy

3.1.2.1 Membrane Morphology

Scanning electron microscopy was used to take a closer look at the membrane and electrode morphology. Figure 3.2 shows an SEM cross-sectional image of a sensor MEA. Under vacuum conditions in the SEM, the dry PEM is approximately 640 µm thick. The entire MEA is approximately 680 µm thick, less than half its thickness under ambient conditions. Whether dry or wet, the sensor membrane is much thicker than a standard Nafion membrane currently used in power generating fuel cells. The most commonly used Nafion membranes range from 50 to 178 µm in thickness.[38] The thick sensor membrane is likely more resistive than a thinner PEM, but it is better for preventing ethanol crossover.

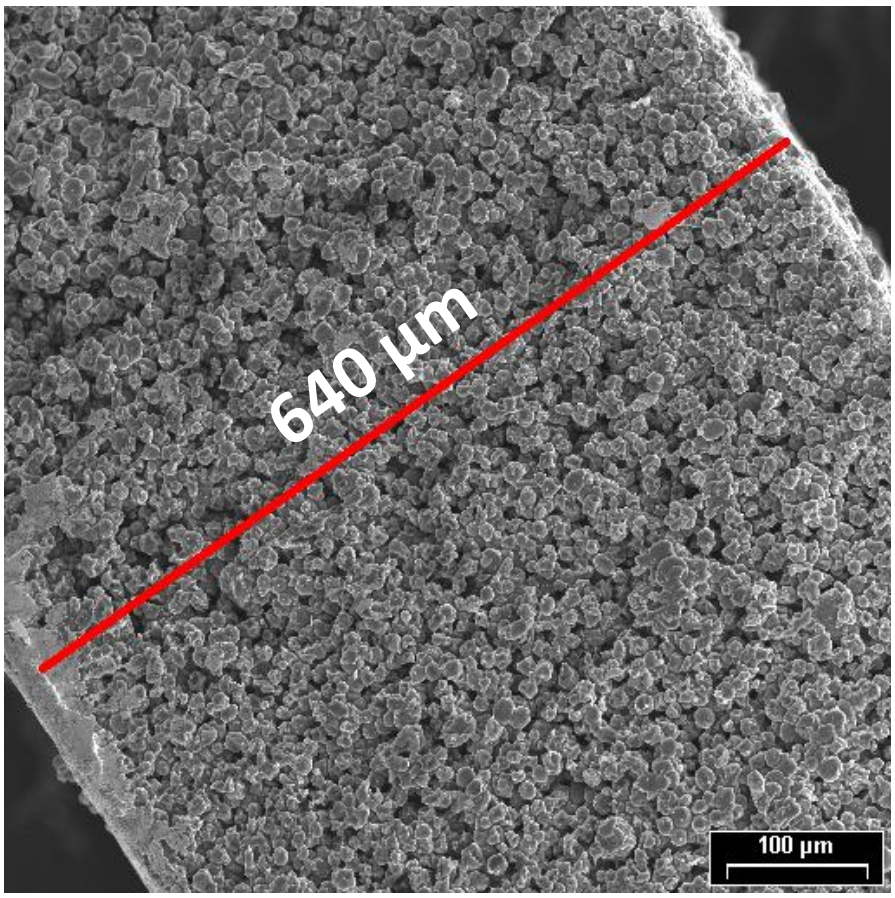

Figure 3.2: SEM micrograph of MEA cross-section

Figure 3.3 is an SEM image of the PEM showing relatively uniformly sized spherical particles approximately 10 µm in diameter. This differs from Nafion and other PFSA PEMs that are typically amorphous films rather than ordered structures with visible individual particles. Void spaces between PVC particles in the sensor PEM results in large, interconnected pores. The porous PEM is impregnated with liquid electrolyte by filling the pores with sulfuric acid solution. This makes it possible for the electrolyte to be washed out of the membrane over time. In contrast, Nafion contains hydrated fixed SO_3^- groups rather than a liquid electrolyte.

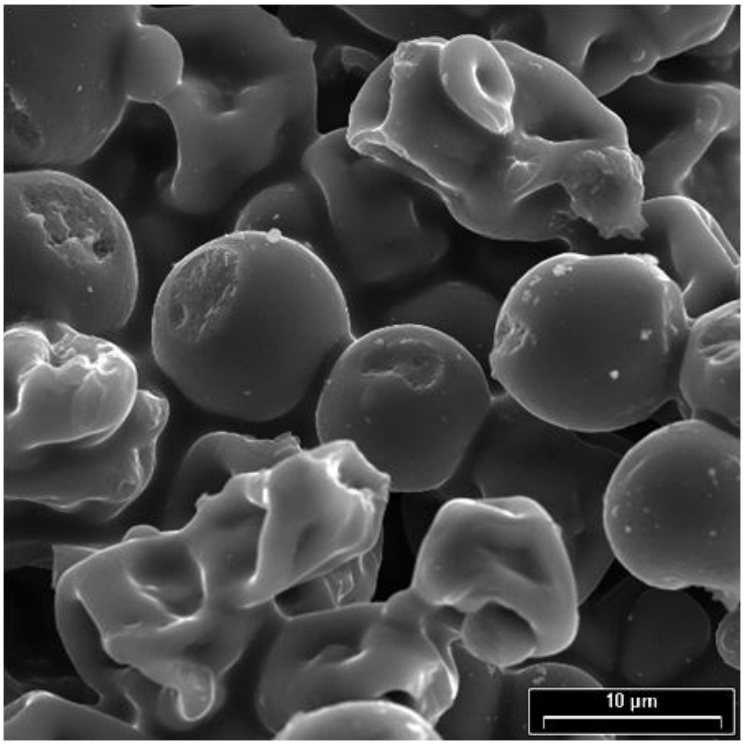

Figure 3.3: SEM image of spherical PVC particles in sensor PEM

3.1.2.2 Morphology of Sensor Electrodes

The anode and cathode catalyst layers appear to be identical in thickness, morphology and composition. Figure 3.4 shows cross-sectional views of a sensor anode and cathode. The catalyst layer is approximately 20 µm thick. In Figure 3.4 b the membrane is contracting under the vacuum conditions and beginning to pull away from the catalyst layer. The Au layer can be seen on the membrane where it has detached

from the catalyst layer. There are also visible fibers where the catalyst layer is peeling away from the Au layer. This is consistent with previous observations of fibrils in Teflon-bonded Pt electrodes.[39]

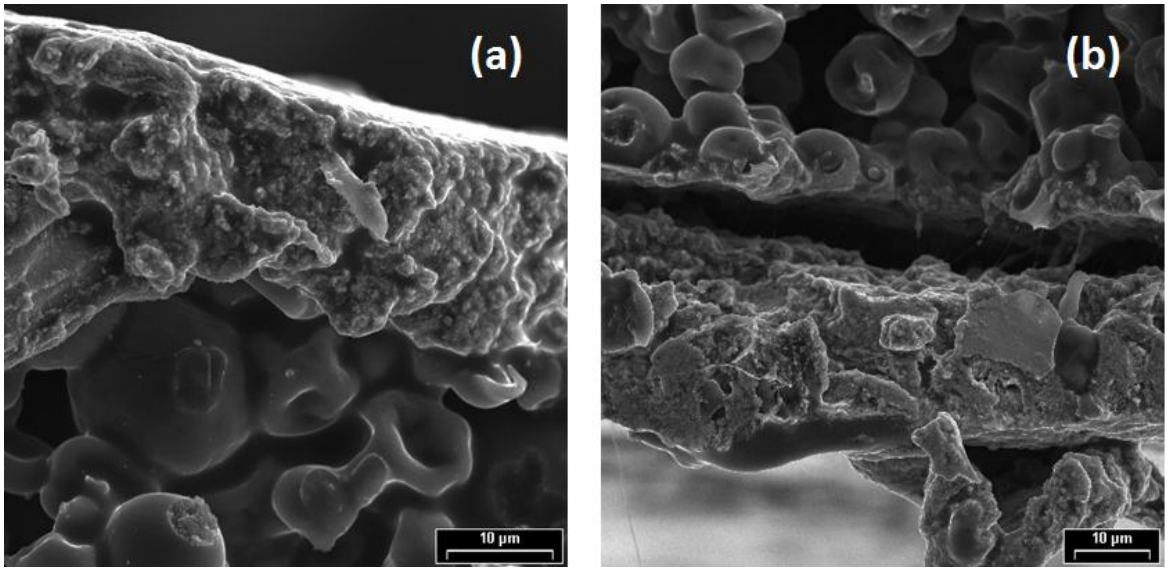

Figure 3.4: Cross-sectional SEM micrographs of sensor a) anode and b) cathode

3.1.3 Morphology of Harvested Catalyst Material

Transmission Electron Microscopy (TEM) was used to investigate the morphology of harvested catalyst material. Figures 3.5 and 3.6 show TEM micrograph images of harvested sensor catalyst material 50, 000 and 20, 000 x magnification. The dark spots appear to be 150-200 nm agglomerates of Pt particles and the white spots are likely a fluorinated organic binding material. Individual Pt particles are not distinguishable in the TEM images. The Pt particle size was determined using XRD measurements.

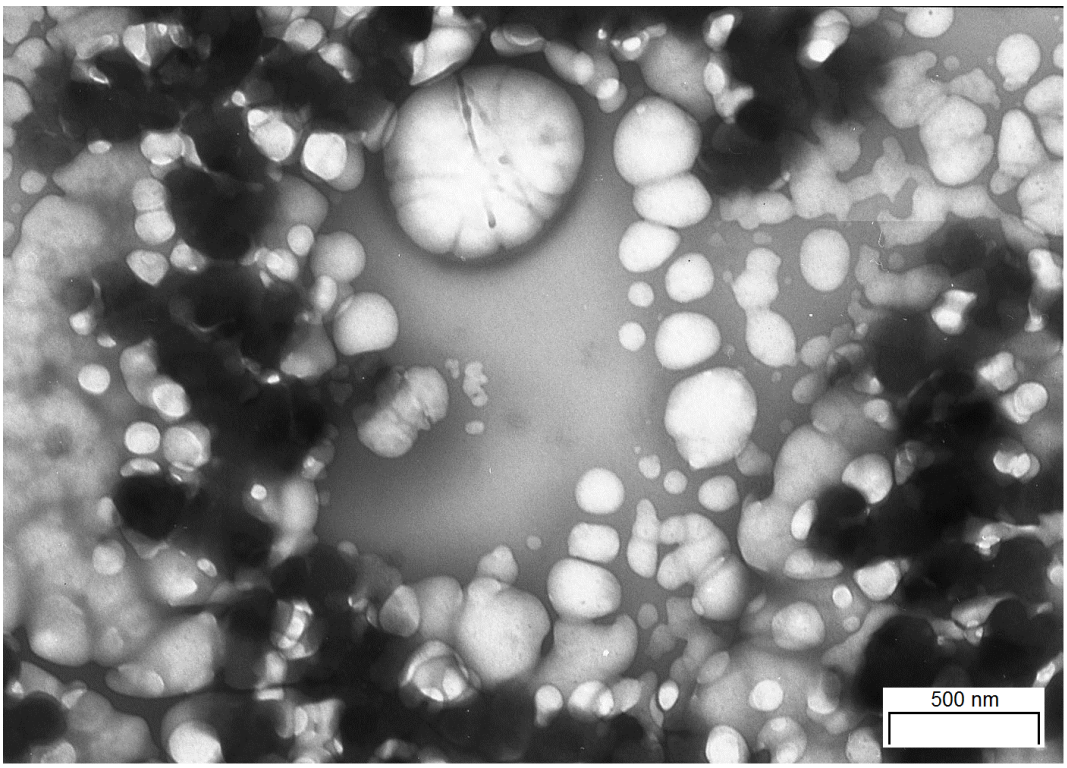

Figure 3.5: TEM micrograph of harvested catalyst material at 50, 000 x magnification

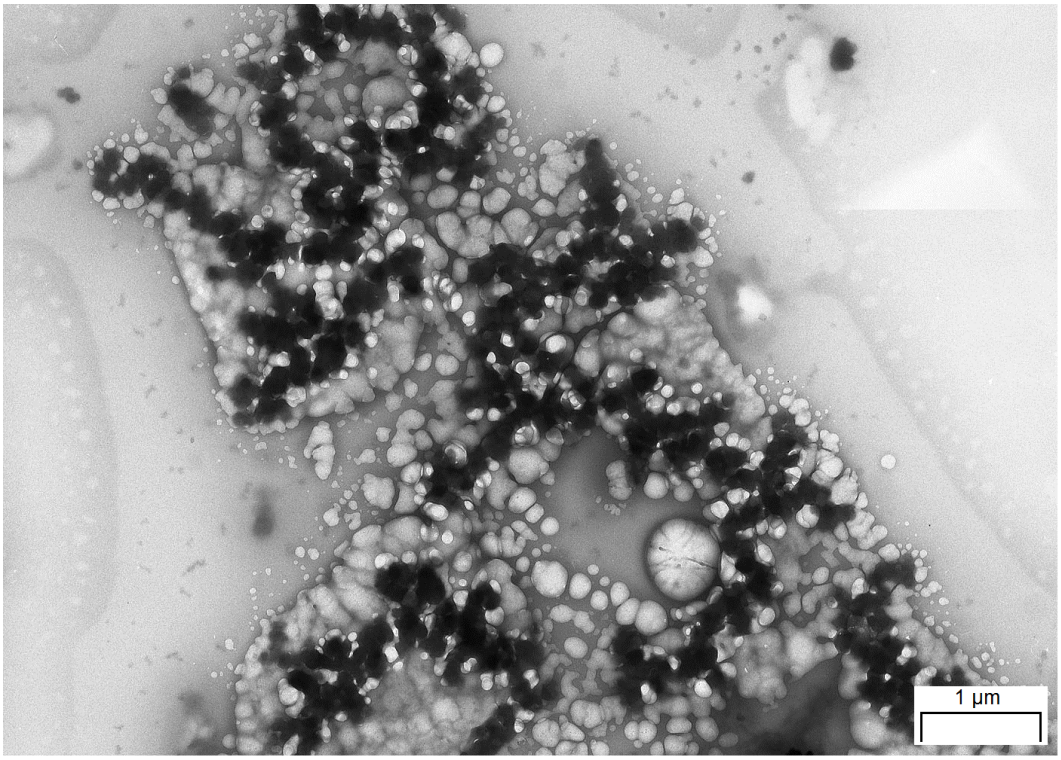

Figure 3.6: TEM micrograph of harvested catalyst material at 20, 000 x magnification

3.1.4 Pt Catalyst Particle Size

Powder X-ray diffraction was used to estimate the Pt particle size in catalyst material harvested from a fresh sensor. Figure 3.7 shows the XRD spectrum obtained for the Pt catalyst. The peaks observed at 39.9°, 46.2°, 67.6° and 81.4° were assigned to the Pt (111), Pt(200), Pt(220) and Pt(311) faces respectively of the Pt face-centered cubic crystal structure.[30] Pt particle size was calculated using the Scherrer equation[40],

$$d = \frac{0.9\lambda}{B_{2\theta} cos\theta_{max}} \qquad \text{Equation 3.1}$$

where *d* is particle size (diameter), 0.9 is an instrument calibration parameter, λ=1.5406 Å was the X-ray wavelength, ϑ is the scattering angle at the peak maximum and $B_{2\theta}$ is the width of the peak at half its maximum height. For the Pt(200) peak the peak maximum was located at ϑ =23.1° and $B_{2\theta}$ =1.3°. The result was a Pt particle size of d=6.6 nm. The Pt(111), Pt(220) and Pt(311) peaks gave particle sizes of 7.9, 6.5 and 6.3 nm respectively, for an average of 6.8 nm. The Pt particles in power generating fuel cells are typically 3-5 nm in diameter.[6] The sensor catalyst particles are of comparable size to other commercially available Pt black catalysts. For example, HiSPEC™ 1000 manufactured by Johnson Matthey is a commonly used catalyst for direct methanol fuel cells. Research conducted at Los Alamos National Laboratory reported the particle size of HiSPEC™ 1000 Pt black to be 6 nm.[41]

Comparing the XRD result with TEM images of the catalyst material, it appears the Pt particles are highly agglomerated. XRD revealed the individual Pt particles are 6.8 nm whereas the TEM showed 150-200 nm agglomerates of Pt. This is expected to greatly reduce the ECSA and Pt utilization efficiency since Pt particles inside large agglomerates would be less accessible to reagents.

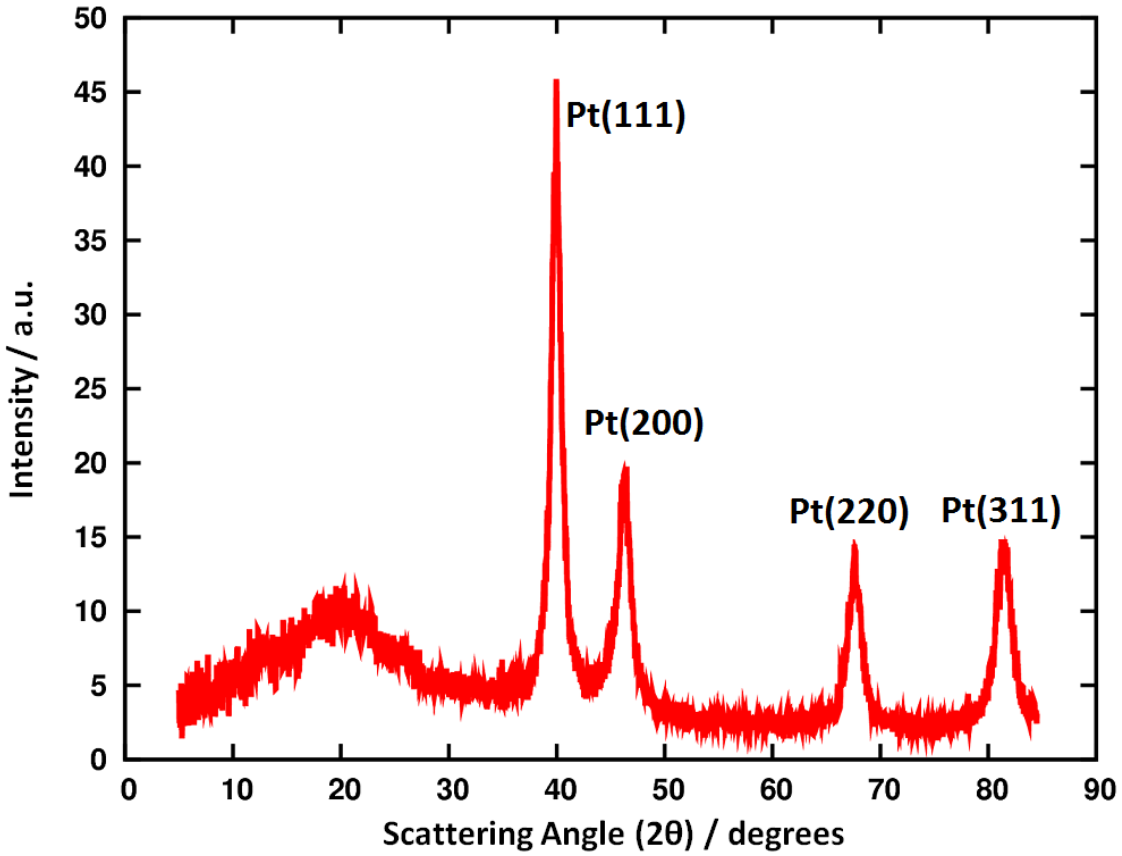

Figure 3.7: Powder XRD spectrum of catalyst material harvested from a fresh breath alcohol sensor MEA

3.1.5 BET Surface Area of Catalyst Layer

The surface area of the catalyst material was estimated by isothermal N_2 adsorption. The BET surface area was determined to be 8.28 m^2g^{-1}. This is lower than the surface area of other Pt black catalysts on the market. For example, Johnson Matthey sells a high surface area Pt black catalyst with a surface area of 28 m^2g^{-1}, more than three times that of the sensor catalyst.[42] Furthermore, the BET surface area of the sensor catalyst layer could be greatly improved by dispersing Pt black on a high surface area carbon support. Vulcan carbon XC-72, a common fuel cell catalyst support material, has a BET surface area of 232 m^2g^{-1}.[43]

3.2 Chemical Composition of PEM

3.2.1 Elemental Composition of PEM

Energy Dispersive X-ray Spectroscopy (EDS) was used to identify the elements present in the sensor PEM. Figure 3.8 shows the EDS spectrum for a sensor PEM. The presence of carbon and chlorine is consistent with identification of PVC as the PEM material. Sulfur and oxygen were also present because the PEM is impregnated with sulfuric acid electrolyte.

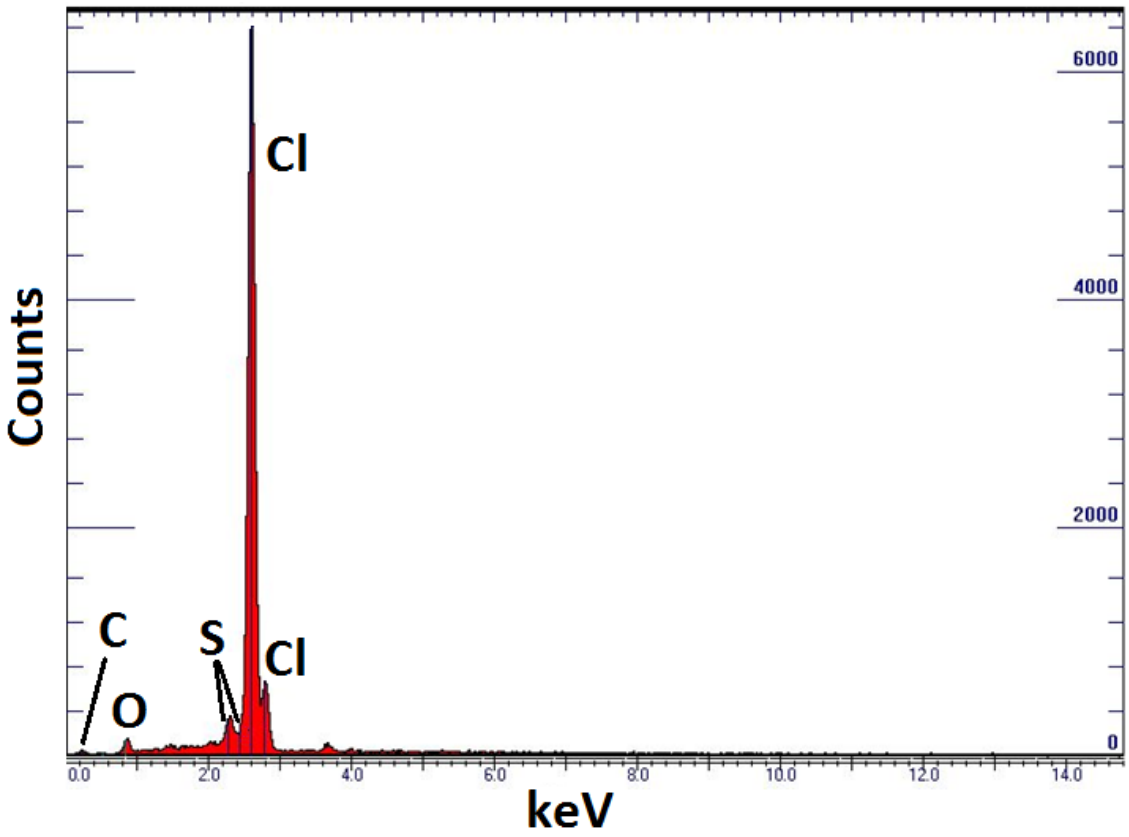

Figure 3.8: EDS spectrum for breath alcohol sensor PEM

3.2.2 Thermogravimetric Analysis (TGA) of PEM Combustion

Combustion analysis of the sensor PEM material was done as a simple test to compare it with the combustion behavior of a known PVC sample. Figure 3.8 shows the weight percent curve and derivative weight percent curves for combustion of a commercial PVC sample and sensor PEM material. The weight loss profile for the sensor

PEM looks almost identical to that of the known PVC sample. This supports the identification of PVC as the PEM material.

PVC combustion has been studied extensively in the literature.[44, 45] The peak at 300 °C is due to evolution of hydrochloric acid and possibly a small amount of benzene. At 450 °C carbon dioxide, carbon monoxide and methane are generated. Finally, at 560 °C the membrane combustion is completed with the evolution of more carbon dioxide and carbon monoxide.

PVC is much cheaper and easier to produce than PFSA membranes like Nafion. The proton conductivity could be improved by moving to a PFSA type of membrane. However, the benefit would have to be considered against the added cost. A cheaper alternative to PFSA membranes could be made from sulfonated silica material. Silica is hygroscopic and might maintain the membrane hydration and proton conductivity over a wider range of temperature and humidity conditions.

3.3 Chemical Composition of the Electrodes

3.3.1 Elemental Composition of Sensor Electrodes

The elemental composition of the sensor electrodes was investigated by performing EDS on an MEA. The EDS spectrum is shown in Figure 3.10 and the results are summarized in Table 3.1. There is evidently a large amount of Pt and some Au present in the sensor electrodes. The Au is in the sub-layer between membrane and catalyst layers. The presence of other metals such as Ru and Sn were considered but they were not observed by EDS. Therefore, the catalyst layer does not contain bimetallic alloys PtSn or PtRu which are commonly used as catalysts in direct alcohol fuel cells. The sensor catalyst is Pt black.

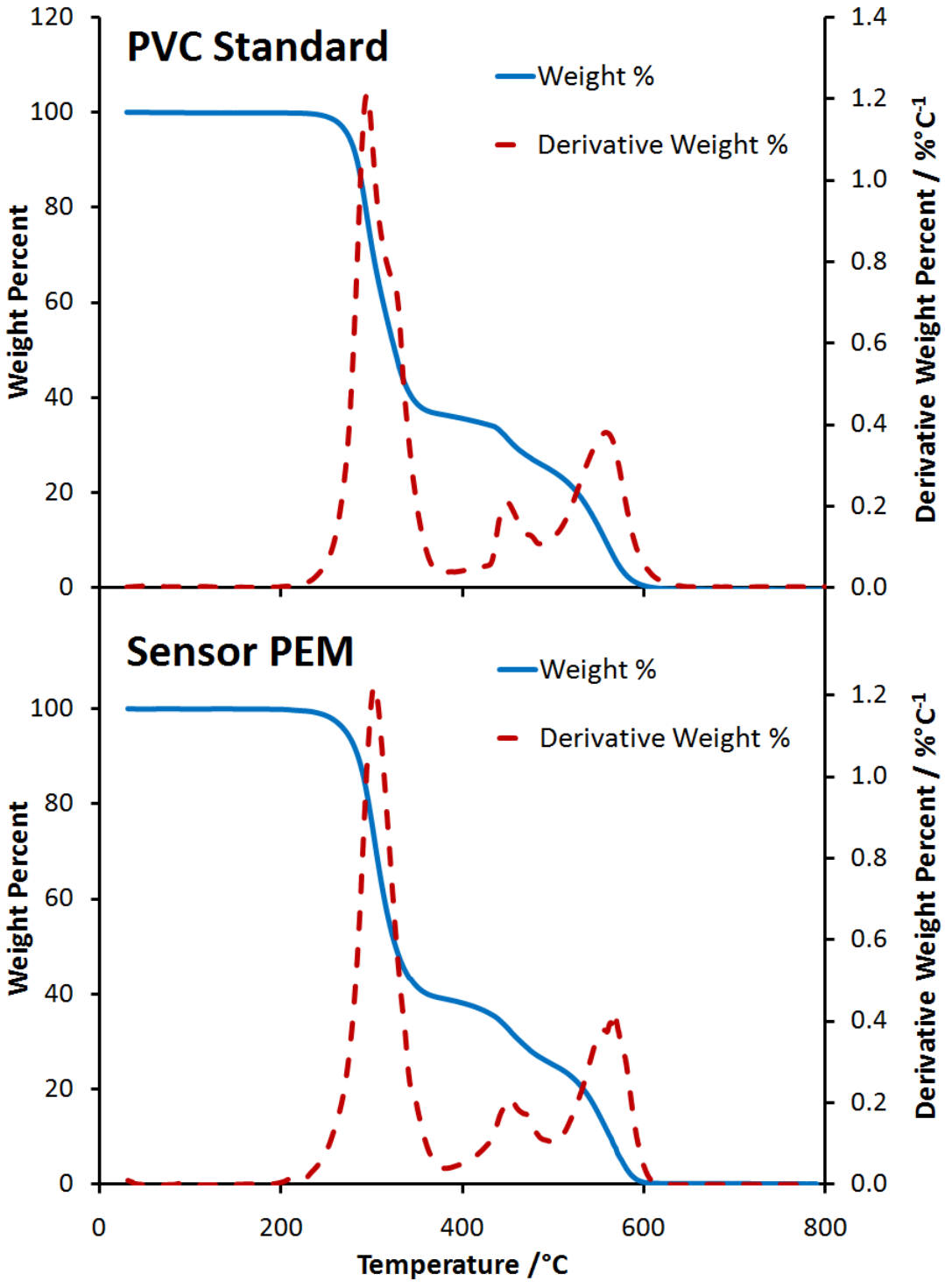

Figure 3.9: TGA weight % and derivative weight % curves for combustion of PVC standard and sensor PEM at 20°Cmin^{-1} heating rate and 50 mLmin^{-1} flowing air

EDS detected carbon and fluorine in the electrodes. The presence of fluorine suggests a fluorinated organic binding material in the catalyst layer. The most likely candidates are Teflon or Nafion. There is much precedence in the literature for Teflon-bonded platinum electrodes for ethanol oxidation[7, 8] and oxygen reduction[35, 46]. However, Nafion is commonly added to fuel cell catalyst layers as an ionomer for proton conductivity as well as a binder. The main difference between Nafion and Teflon is the SO_3^- groups in Nafion. However, absolutely no sulfur was observed in the catalyst layer by EDS, ruling out Nafion as the fluorinated polymer. This seems to confirm Teflon or a similar fluoropolymer is the organic binding material in the catalyst layer.

There was a small amount of chlorine (0.17 weight %) observed by EDS. This could be explained by some contamination of the catalyst with PVC from the membrane.

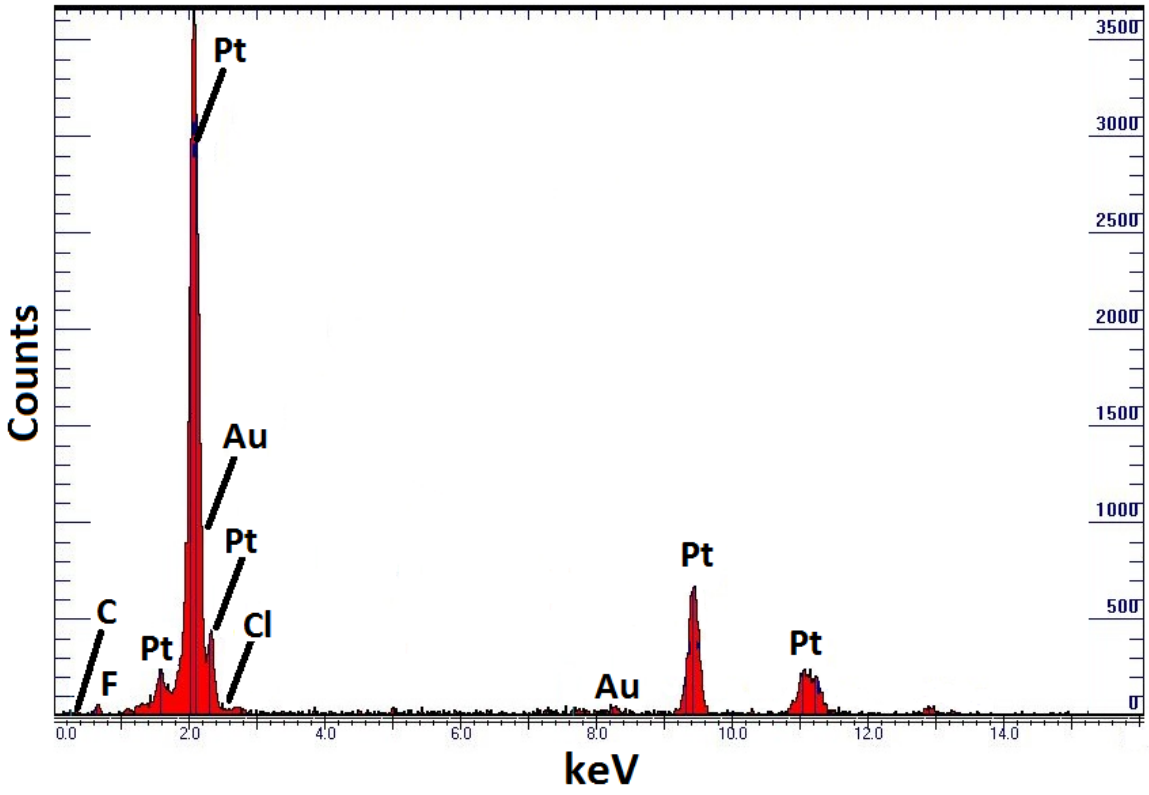

Figure 3.10: EDS spectrum of sensor electrode

Table 3.1: Tabulated EDS results for sensor electrode

Element	Counts per second	Weight Percent	Atomic Percent
Pt	60.85	97.15	93.53
Au	1.33	2.34	2.24
Ru	0.00	0.00	0.00
Sn	0.00	0.00	0.00
F	0.58	0.34	3.32
Cl	1.26	0.17	0.91
S	0.00	0.00	0.00

3.3.2 Metal Loadings in the Sensor Electrodes

Inductively coupled plasma-optical emission spectroscopy was performed to quantitatively determine the Pt and Au loadings in the sensor electrodes. A series of platinum and gold standard solutions were prepared and used to generate the calibration curves in Figure 3.11.

The ICP-OES results for two MEA samples are summarized in the tables below. The average total metal loadings in an MEA, counting both electrodes, are 52.2 mg of Pt and 1.4 mg of Au. The total electrode surface area is 3.8 cm^2, giving Pt and Au loadings of 13.7 $mgcm^2$ and 0.4 $mgcm^2$ respectively. The Pt loading is much higher than the typical catalyst loading of 2 $mgcm^{-2}$ for DAFCs.[34, 47]

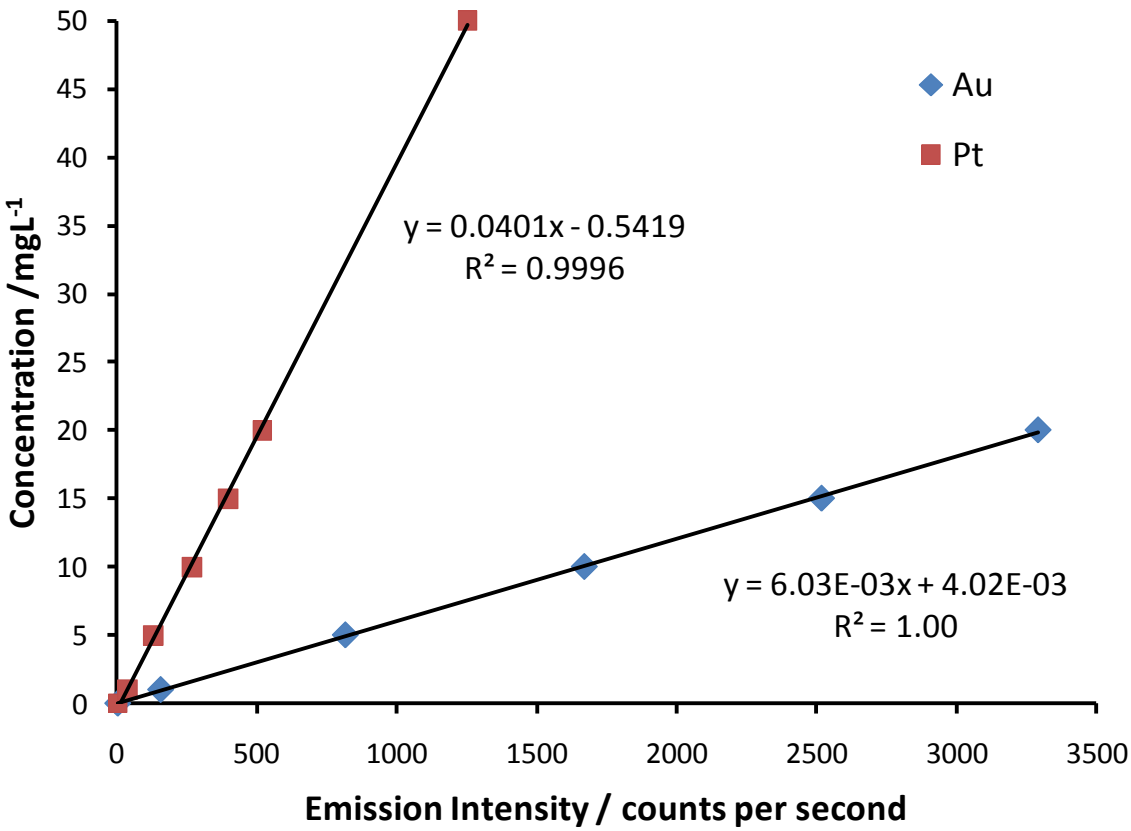

Figure 3.11: ICP-OES calibration plot for Pt and Au standard solutions

Table 3.2: ICP-OES results for Pt in sensor electrodes

Sample	Intensity at 214.424 nm / counts per s	Pt Concentration /mgL^{-1}	Total Pt Loading /mg
1	126.96	4.55	56.86
2	108.48	3.81	47.60

Table 3.3: ICP-OES results for Au in sensor electrodes

Sample	Intensity at 242.794 nm / counts per s	Au Concentration /mgL^{-1}	Total Au Loading /mg
1	783	4.73	1.18
2	1070	6.45	1.61

3.3.3 Elemental Composition of Harvested Catalyst Material

XPS was performed to determine the elemental composition of harvested catalyst material. XPS survey scan spectra are shown in Figure 3.12 for catalyst material from two MEAs. The survey spectra are very reproducible and peaks are observed in the Pt, C, O, S and F regions as expected based on the EDS results. Au peaks would appear at approximately 84 and 368 eV but none were observed because the catalyst material was harvested without removing the Au layer beneath.[48] The sulfur 2p 3/2 peak at 169.8 eV is consistent with sulfuric acid which is reported at 169.60 eV.[49] It is likely that sulfuric acid electrolyte leached into the catalyst layer from the PEM.

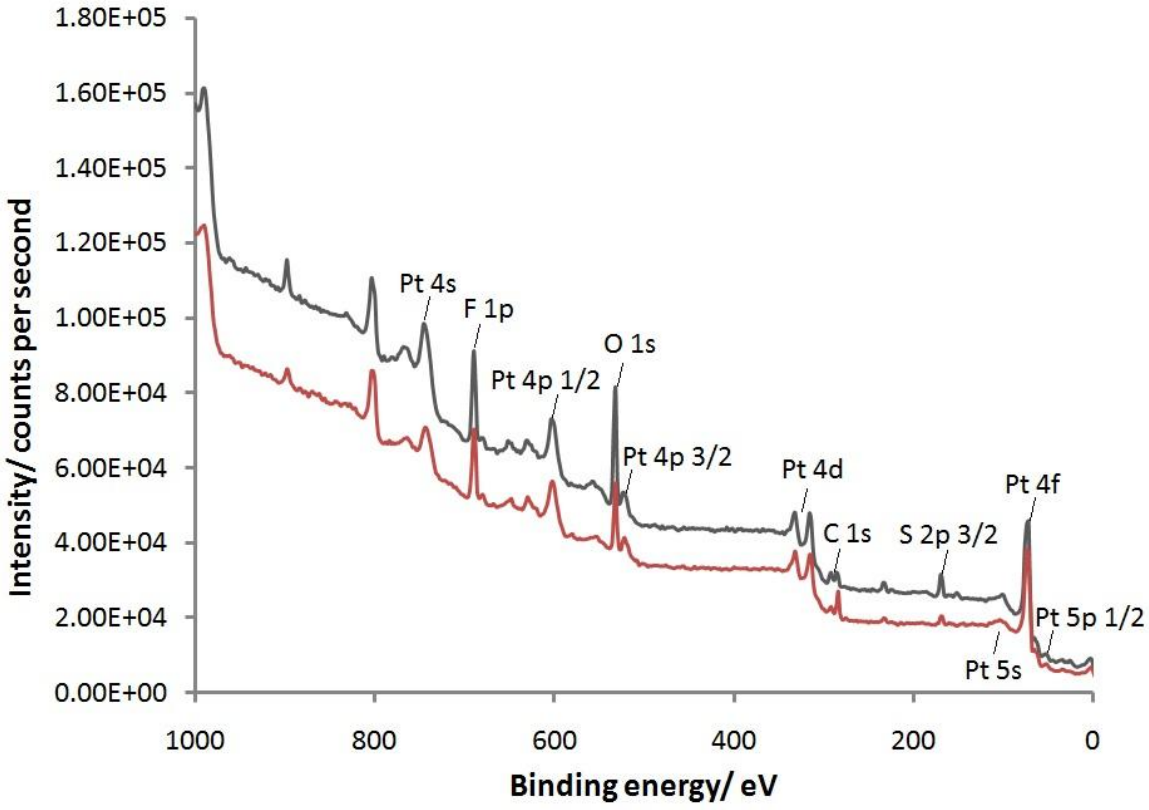

Figure 3.12: XPS survey scan spectra for catalyst material harvested from two different fresh sensors

A high resolution XPS scan in the Pt 4f region is shown in Figure 3.13. Deconvolution of the Pt peaks revealed the presence of Pt^0 and PtO. The pair of large

peaks at 71.5 and 75 eV arise from zero-valent Pt and the smaller peaks at 72.6 and 77 eV are due to PtO.[50]

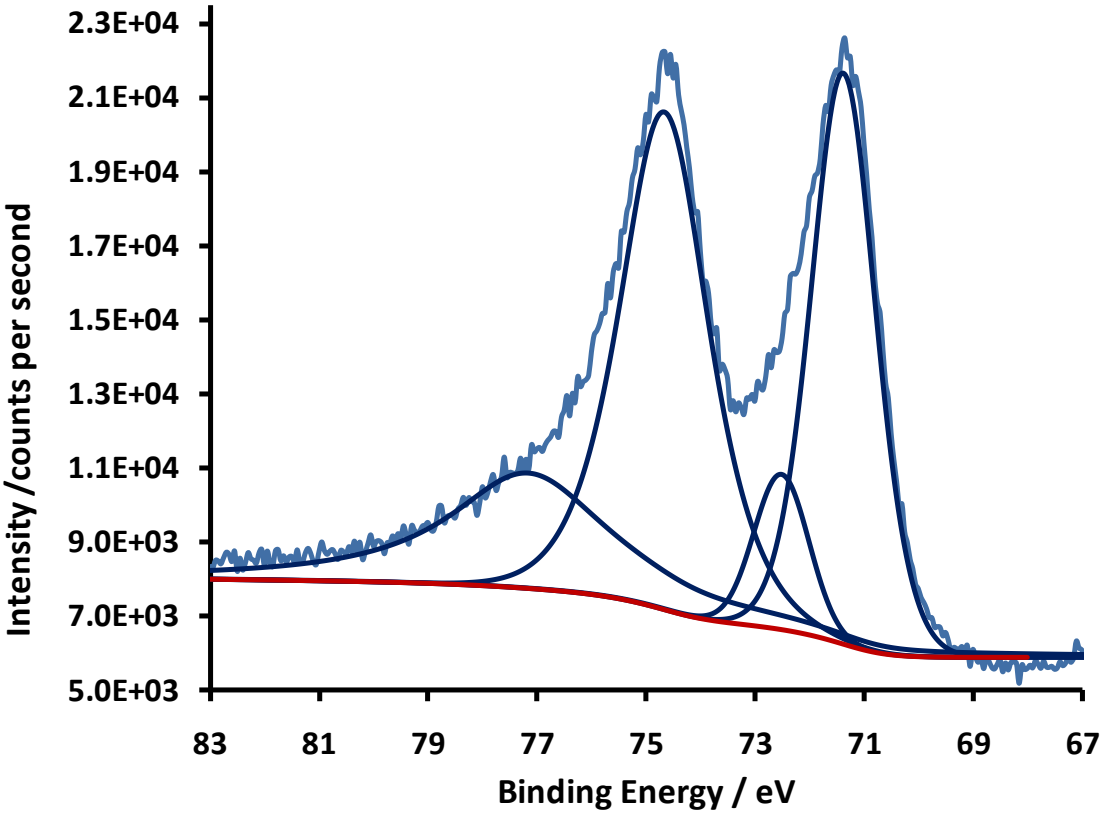

Figure 3.13: High resolution XPS spectrum in the Pt 4f region. Peak fitting was done using Gaussian-Lorentzian curves and a Shirley background.

A high resolution scan in the carbon 1s region is shown in Figure 3.14. A thin film of carbonaceous material, referred to as adventitious carbon, is typically found on the surface of samples that have been exposed to the air and is observed at 284.8 eV.[49] The peak at approximately 293 eV is characteristic of fluorinated carbon. A peak at 292.6 eV has previously been assigned to the CF_2 group of Teflon.[51] PVC was also considered as a possible binding material in the catalyst layer because PVC was identified as the membrane material. However, a high resolution scan in the chlorine 2p region revealed the absence of Cl peaks, ruling out the presence of PVC as the catalyst binder. The XPS results are consistent with EDS analysis of the sensor electrodes, suggesting Teflon-bonded Pt black electrodes.

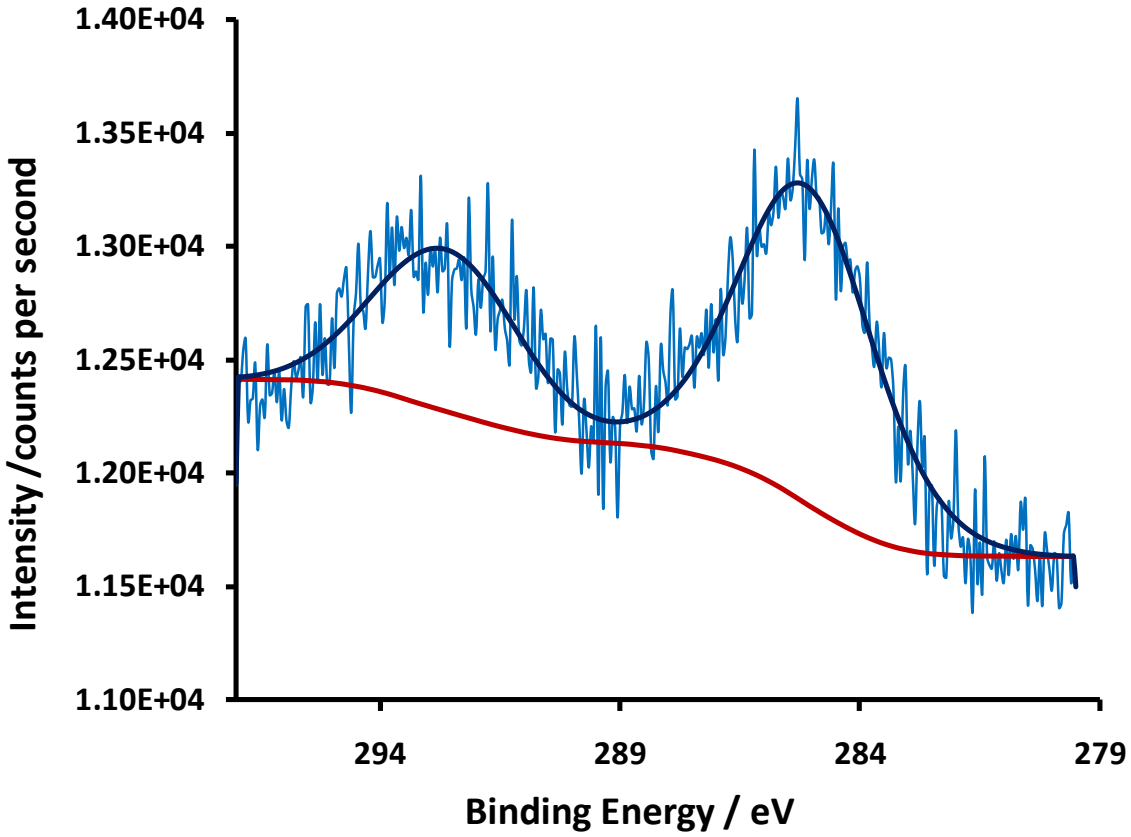

Figure 3.14: High resolution XPS spectrum of C 1s region indicating CF_2 and CF_3 in the catalyst layer

3.3.4 Thermogravimetric Analysis of Catalyst Material

TGA was used to determine the relative loadings of Pt and organic binder in the catalyst layer. Figure 3.15 depicts the weight percent curves and corresponding derivative weight percent curves for harvested catalyst material under argon or air. The weight percents have been normalized so the weight at 500 °C is the 'dry weight' of the sample once all volatile components have evaporated. In both air and argon the weight loss below 500 °C corresponds to evaporation of water and sulfuric acid. Both samples contained approximately 30% of their weight in water or other volatile substances.

There is a 10% weight loss between 500 and 600 °C in both atmospheres. This corresponds to combustion or decomposition of the fluorinated organic binding material. The final weight percent under air is equal to the mass of metal remaining

once all of the organic material undergoes combustion. 90% of the sample weight remained after heating in both atmospheres. Therefore, the dry catalyst material consists of 90% metal and 10% organic material. EDS and XPS identified the metals as Pt and Au and the organic material as Teflon or a similar fluoropolymer. The weight percent of metal in harvested catalyst material as determined by TGA is used to calculate Pt concentrations in catalyst inks for electrochemical experiments.

The derivative weight percent curves show more clearly the temperatures at which individual decomposition processes occur. The small shoulder observed just above 500 °C in the derivative weight percent curve under argon is due to de-polymerization of Teflon.[52] Under air the Teflon simply undergoes combustion. Additionally there are small weight losses at 375 °C under argon and 420 °C under air. These could be due to evaporation of sulfuric acid (b.p. 327 °C) that leached into the electrodes from the membrane.

3.4 Chemical Composition of Electrode Binding Material

3.4.1 Images of White Flakes Obtained by Aqua Regia Digestion of MEA

After soaking an MEA in aqua regia overnight in preparation for ICP-OES analysis, the PVC membrane and white flakes were removed from the metal solution by vacuum filtration. Figure 3.16 (a) shows the membrane and flakes that were obtained and Figure 3.16 (b) is an optical microscope image of a flake. Note that the white flakes in Figure 3.16 (a) originated from the digestion of two MEAs and therefore do not reflect the mass of flake material from a single MEA.

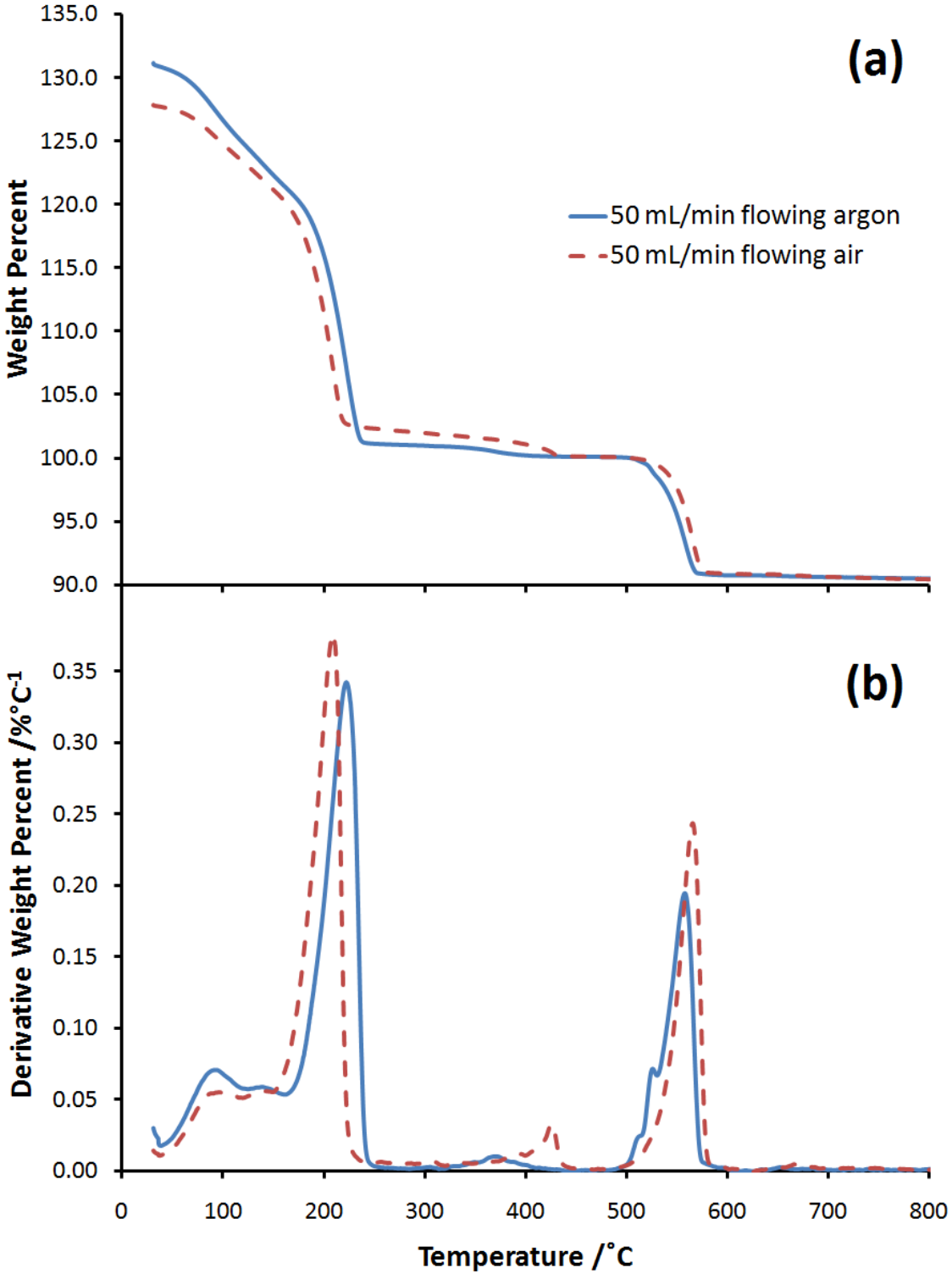

Figure 3.15: a) Weight percent and b) derivative weight percent curves for harvested catalyst material heated at 20 °Cmin^{-1} under flowing air or argon

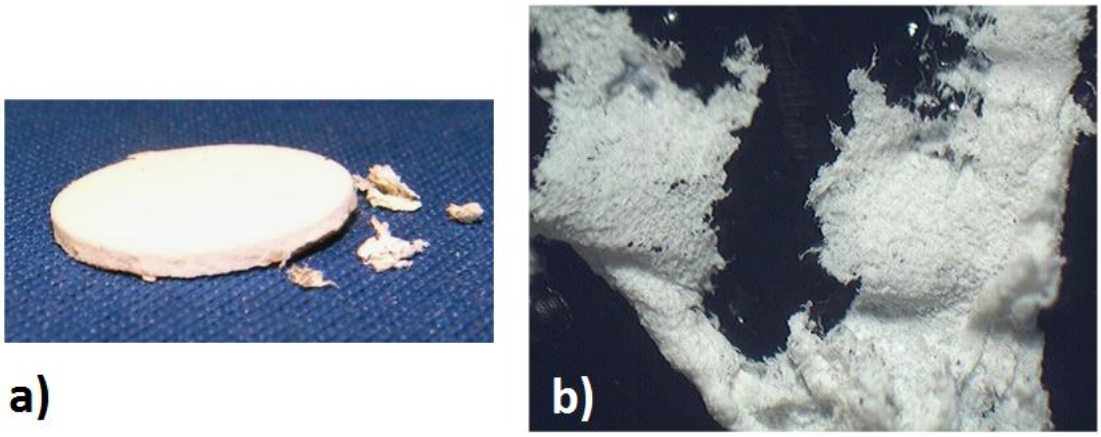

Figure 3.16: a) a PVC membrane and some white flakes retrieved from the metal solution after digesting sensor MEAs in aqua regia, and b) an optical microscope image of a flake

3.4.2 Elemental Composition of Flakes

The flakes were analyzed using EDS to identify their elemental composition. The EDS spectrum for a flake is shown in Figure 3.17 and the corresponding tabulated data is displayed in Table 3.4. These results demonstrate the white flakes are made of carbon and fluorine. They are not flakes of PVC from the PEM, otherwise they would contain chlorine rather than fluorine. They are also not Nafion because they contain essentially zero sulfur. We can conclude that the flakes are the source of the fluorine peaks in the XPS spectrum of the catalyst layer.

Table 3.4: Tabulated EDS Results for White Flakes From Aqua Regia Digestion

Element	Counts per second	Weight Percent	Atomic Percent
C	4.45	89.67	93.93
F	66.48	9.02	5.97
S	3.17	0.04	0.01
Pt	3.01	0.99	0.06
Au	0.79	0.29	0.02

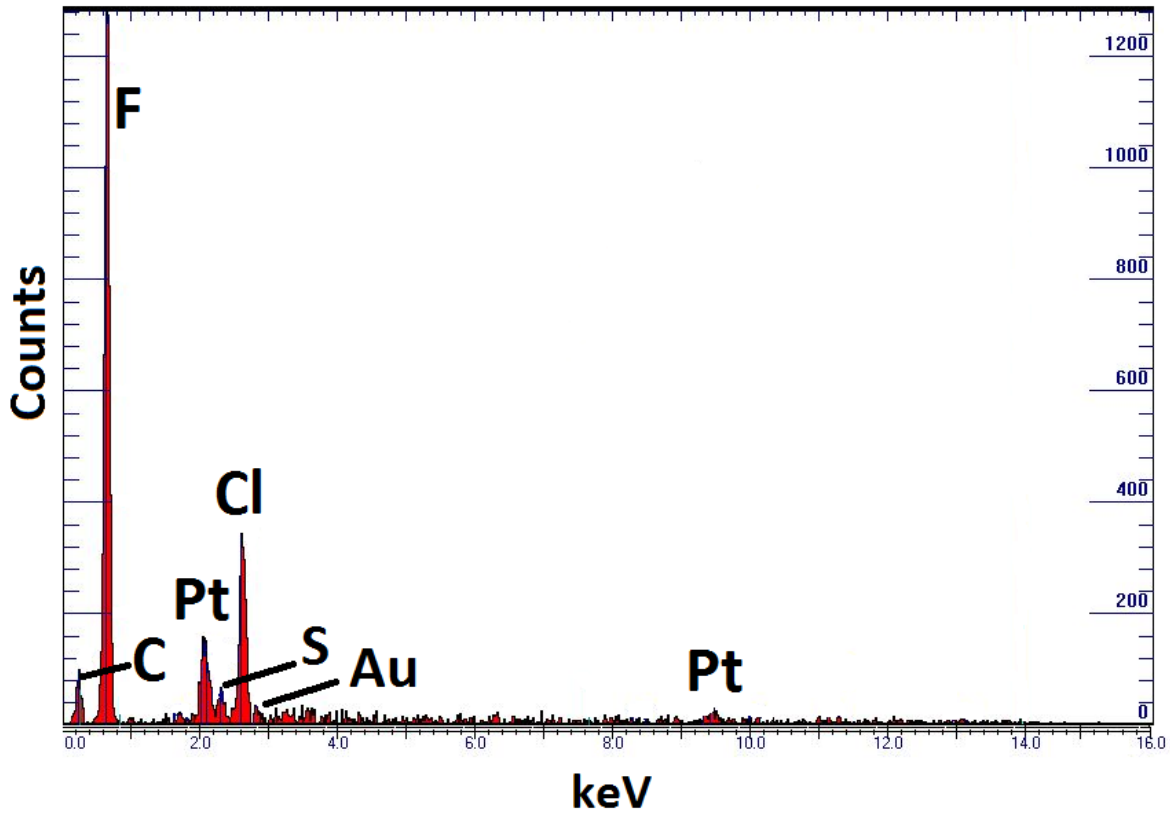

Figure 3.17: EDS spectrum for white flakes retrieved from aqua regia digestion

3.4.3 IR of Flakes

Infrared spectroscopy was used to compare a flake with a piece of Teflon. Figure 3.18 shows the two IR spectra are nearly identical. The two large peaks appearing in both spectra at 1151 and 1206 cm^{-1} are assigned to the CF_2 symmetric and asymmetric stretch respectively.[53] There are two small peaks in the flake spectrum at 872 and 1045 cm^{-1}. The source of these peaks is unclear. They likely arise from contaminants from the aqua regia digestion.

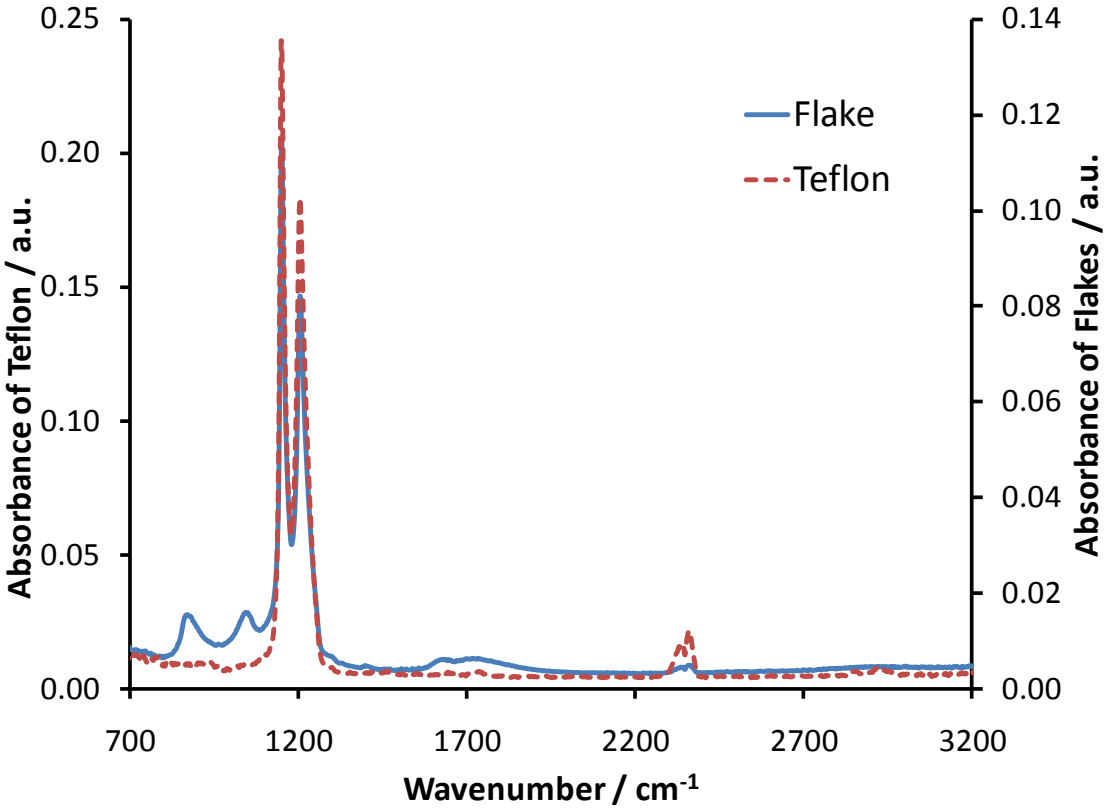

Figure 3.18: FT-IR spectra for a flake and a piece of Teflon sheet

3.4.4 Raman Spectroscopy of Flakes

The IR data supported the identification of the flakes as fluoropolymer from the catalyst layer. Raman spectroscopy was performed as an additional test to compare the flakes with Teflon. Figure 3.19 shows the Raman spectra for a piece of Teflon and a flake. The spectra are essentially identical. It can be concluded from the EDS, IR and Raman spectroscopy results that the flakes are fluorinated polymer binder, likely Teflon, from the catalyst layer.

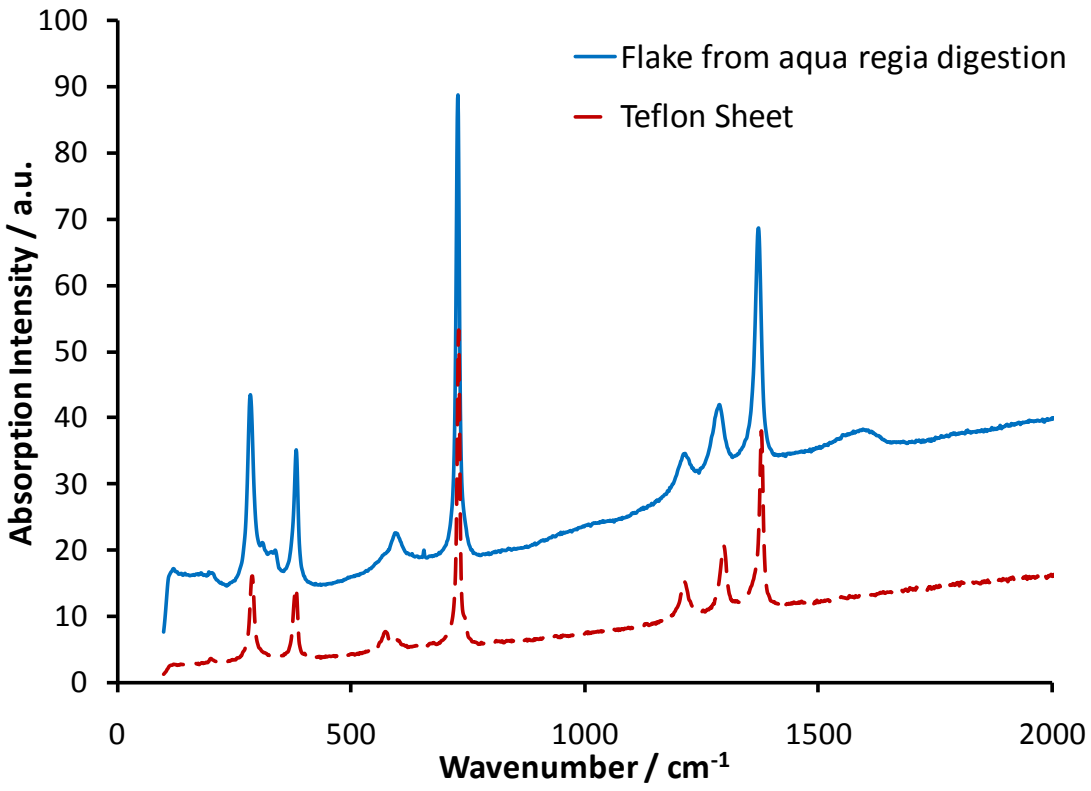

Figure 3.19: Raman spectra for a flake and a piece of Teflon sheet

3.4.5 TGA of Flakes

The white flakes obtained after digestion of an MEA in aqua regia appear to be fluoropolymer binding material from the catalyst layer. Combustion of the flake material was investigated using TGA in order to compare with the combustion of harvested catalyst material. Figure 3.20 shows the TGA and derivative weight percent curves for combustion of a flake. The flake undergoes almost complete combustion between 500 and 600 °C as expected for a Teflon-like material.[52] The TGA curves for catalyst material and flakes are shown overlaid in Figure 3.21. In both air and argon the weight loss between 500 and 600 °C for the catalyst material is attributed to the fluoropolymer 'flake' material.

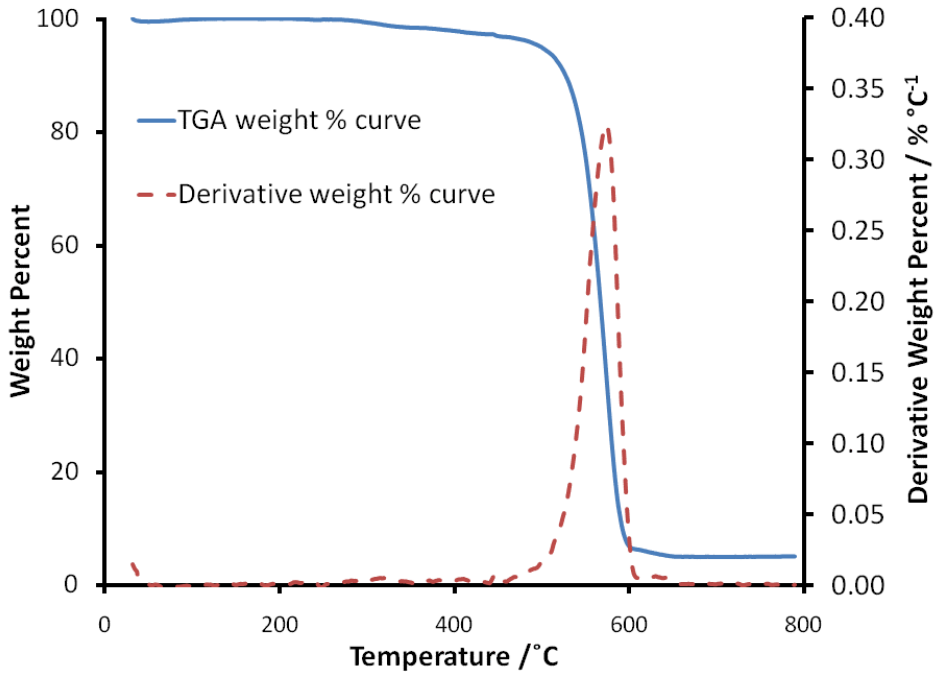

Figure 3.20: TGA and derivative weight percent curves for combustion of a flake heated at 20 °Cmin^{-1} under flowing air

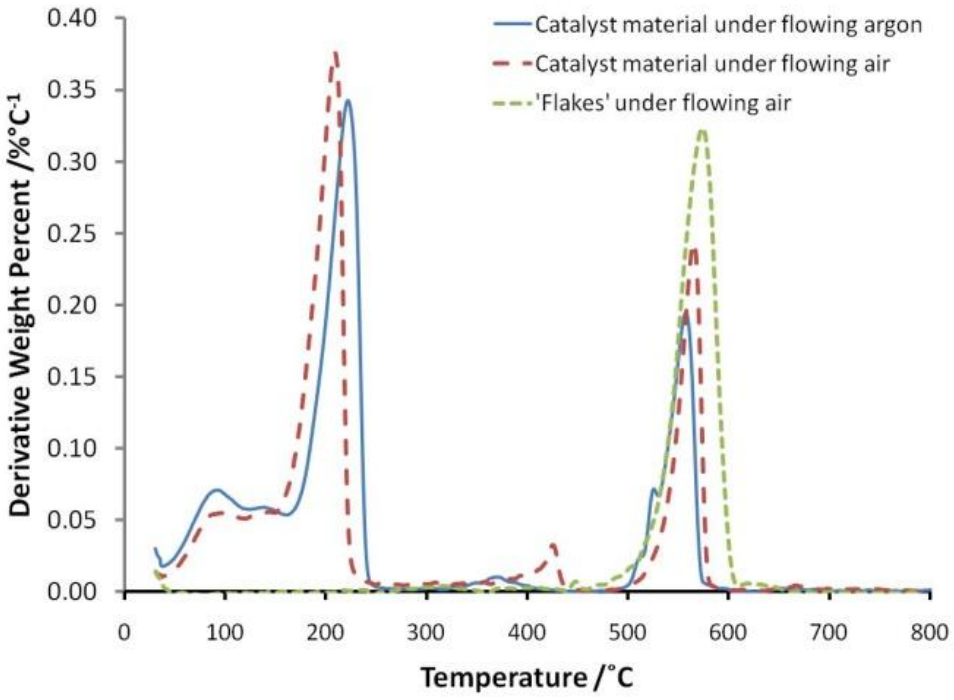

Figure 3.21: TGA and derivative weight percent curves for harvested catalyst material and combustion of a flake

3.5 Discussion of Suggested Improvements for Breath Alcohol Sensors

The materials characterization of commercially available breath alcohol sensors revealed several areas in which the existing sensor could be modified to take advantage of the recent key developments in fuel cell technology. The first improvement could be made easily by using catalyst layers based on current fuel cell technology. One way of doing is moving to a carbon-supported Pt catalyst such 20 wt.% Pt on Vulcan-XC-72 (E-Tek). This would provide a much higher specific surface area than the Teflon-bonded sensor catalyst layer. Reducing the size of the catalyst particles from 6.9 nm to around 3 nm would allow the mass of Pt to be reduced while maintaining the same Pt surface area.

The Teflon-like fluoropolymer in the sensor catalyst layer acts a binding material for the Pt black catalyst. PEMFC electrodes are sometimes fabricated by adding a layer of Nafion to a Teflon-bonded catalyst layer. Nafion or a similar ionomer could be added into the sensor catalyst layer to provide better proton conductivity in the catalyst layer. The hydrophobic fluoropolymer also prevents water condensation on the electrodes which could cover catalyst sites block ethanol vapour from reaching them. Water management in power generating fuel cells is achieved in part by Teflon-coated gas diffusion layers. The sensor electrodes are very dense. The Pt deep inside the catalyst layer right near the membrane is likely also the least accessible to ethanol vapour. The addition of a more typical hydrophobic gas diffusion layer could improve the utilization of Pt throughout the entire depth of the catalyst layer.

Chapter 4 - Electrochemical Characterization of Fresh Breath Alcohol Sensors

Electrochemical measurements were used to characterize the behavior and performance of fresh breath alcohol sensors. This was done to establish a set of values to serve as a reference for comparison with future measurements. The same set of measurements can then be performed on sensors that have undergone accelerated degradation tests to determine the changes in properties and behavior of the sensor and any new materials that will be developed. Proton conductivity of the PEM, ECSA of Pt in the electrodes and sensitivity are characterized here for fresh sensors. Chapter 5 investigates the impact of varying humidity conditions on each of these properties.

4.1 Ionic Resistance of Membranes in Sensors of Various Ages

In order to investigate the change in membrane conductivity under various conditions a baseline set of conductivity values were obtained for a series of sensors at various points in their life cycle. It was expected that older sensors would be less proton conductive as a result of being exposed to changing humidity conditions. Over time, the morphology of the membrane could change. The surface tension exerted by water evaporating from narrow pores could cause some pores to contract or collapse. If some of the proton-conducting pathways through the membrane become extremely narrow or blocked, the ionic resistance of the membrane would likely increase.

Electrochemical impedance spectroscopy (EIS) was used to compare the ionic resistance of the membranes in a series of sensors of various ages. Used sensors were analyzed from production years between 2004 and 2010 along with three unused (fresh) sensors from 2010. All of the used sensors had been removed from devices after being in use for a period of time. After being received from the provider the sensors were stored under ambient conditions (approximately 22°C and 20% RH) in the laboratory for four months. Therefore, the sensors were all equilibrated in identical conditions prior to EIS measurements.

Figure 4.1 is a sample Nyquist plot for an EIS measurement of a breath alcohol sensor. The parameters for the line of best fit were determined using ZView software. The x-intercept value of 3.3682 is equal to the HFR value in Ω.

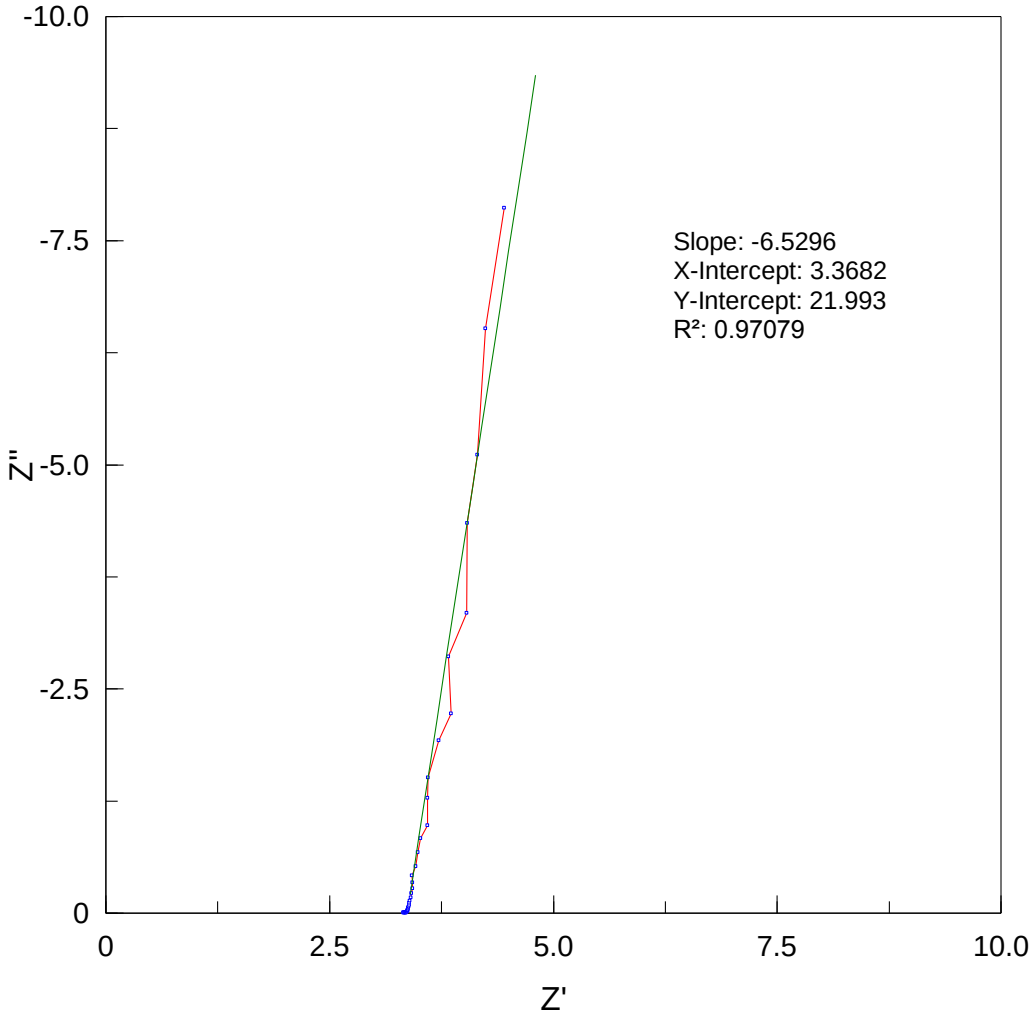

Figure 4.1: Nyquist Plot obtained by EIS measurement for a breath alcohol sensor. The Z' axis corresponds to real impedance (Ω) and the Z" axis corresponds to imaginary impedance (Ω). A line of best fit was plotted using ZView software. The HFR corresponds to the value of the x-intercept.

The HFR values were obtained from the Nyquist plots for each sensor. Proton conductivity of the membrane was calculated from the HFR using equation 4.1. The membrane thickness was estimated at 1.5 mm for a sensor at ambient conditions (section 3.1.1) and the membrane cross-sectional area is 1.91 cm^2. Figure 4.2 compares the average HFR and proton conductivity values calculated for sensors of different ages.

$$\sigma = \frac{membrane\ thickness}{(HFR)(membrane\ area)} \qquad \text{Equation 4.1}$$

The average HFR for used sensors of all ages was 2.34 ± 0.71 Ω compared with 3.11 ± 0.21 Ω for the fresh sensors. These values correspond to average proton conductivity of 0.037 Scm^{-1} and 0.025 Scm^{-1} for used and fresh sensors respectively. There did not appear to be any trend in membrane conductivity with sensor age. Sensors made in 2004-2008 exhibited similar membrane resistance. Sensors from 2009 and fresh sensors from 2010 were relatively more resistant whereas used sensors from 2010 were quite a bit more conductive. Surprisingly, the fresh sensors were all more resistant than the used sensors. However, the standard deviation for the used sensors was larger than that of the fresh sensors. This is not surprising because the fresh sensors were all assembled at approximately the same time and would have been exposed to the controlled temperature and RH conditions of the assembly laboratory. The used sensors each experienced a unique set of conditions over their operational lifetime. The different conditions could have caused changes in the PVC membrane leading to the variability in dehydration behavior.

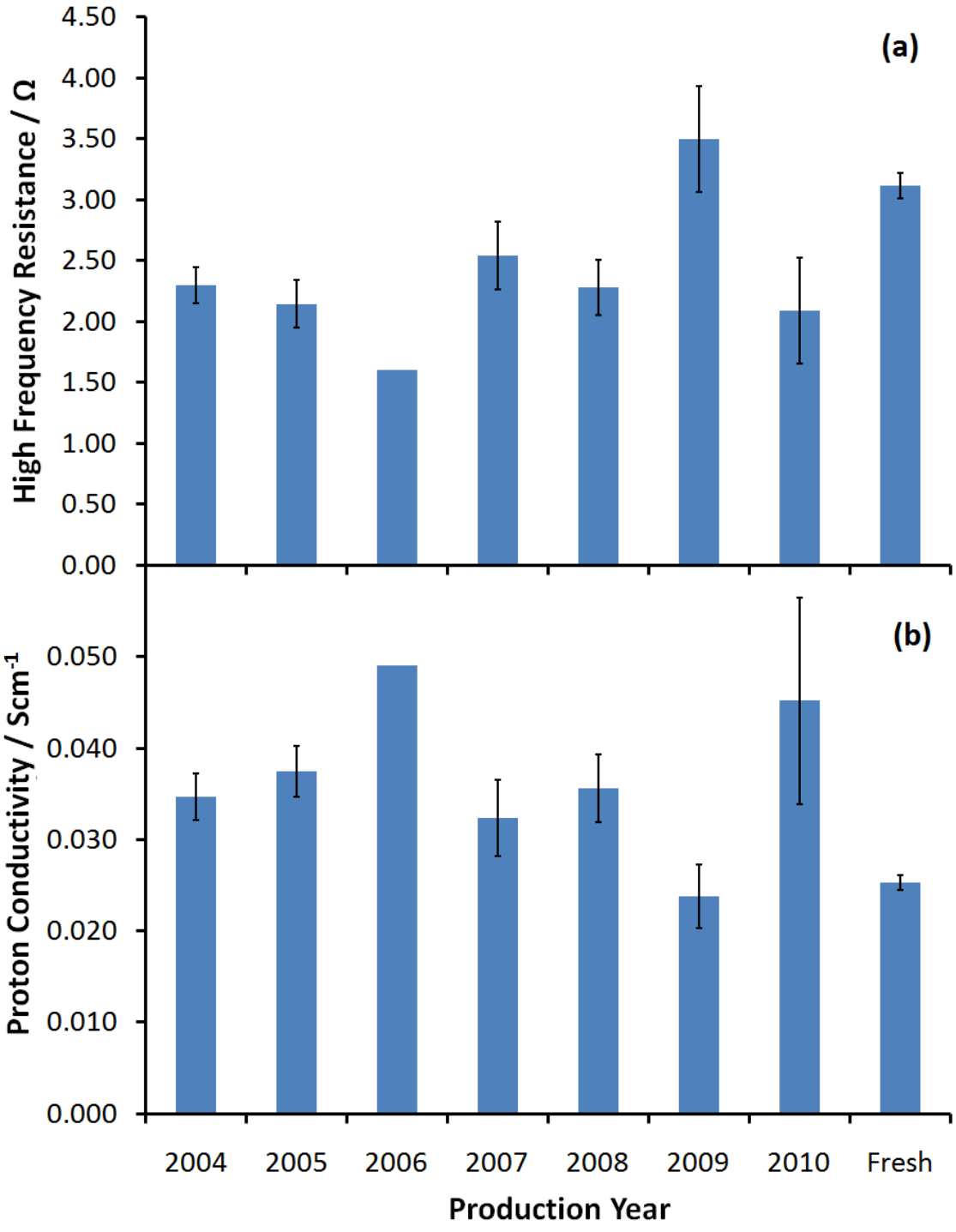

Figure 4.2: a) High frequency resistance and b) proton conductivity at ambient conditions for a series of used sensors of various ages and a fresh sensor from 2010. Error bars correspond to the standard deviation of five measurements for used sensors and three measurements for fresh sensors.

4.2 Pt Utilization and ECSA of Pt in Catalyst Material Harvested from a Fresh Sensor

The Pt utilization efficiency and ECSA of Pt was determined for catalyst material harvested from a fresh sensor and mixed with solubilized Nafion ionomer. Half-cell cyclic voltammetry was used to estimate the real surface area of Pt in the resulting catalyst ink. Figure 4.3 shows the CV for 2 µL of catalyst ink deposited on a glassy carbon electrode in 0.5 M sulfuric acid. The broad peak at 700 mV in the forward scan is due to growth of Pt oxides. Subsequent reduction of Pt oxides produces the peak at 475 mV in the reverse scan. The region of interest in the CV is the set of peaks between -280 and +100 mV. In this potential range, protons from the sulfuric acid solution adsorb and desorb from the Pt surface in the catalyst material as described by the equation 4.2. Current is generated by protons adsorbing and desorbing because a transfer of electrons occurs at the Pt surface.[39]

$$Pt - H_{ads} \xrightarrow{forward\ scan} Pt + H^+ + e^- \xrightarrow{reverse\ scan} Pt - H_{ads} \qquad \text{Equation 4.2}$$

By scanning the potential as low as -280 mV we can assume all the Pt surface that is accessible to the sulfuric acid solution will be covered in a monolayer of hydrogen atoms.[54] The area under the set of hydrogen desorption peaks gives the charge associated with the total amount of hydrogen that was adsorbed on the Pt surface. Monolayer coverage of hydrogen atoms on a Pt surface gives the known value 210 $\mu C cm^{-2}$.[54] The area under the hydrogen desorption peaks in Figure 4.3 was determined by integration using Corrview software. The peak integration indicated a charge of 836.51 µC which was divided by 210 $\mu C cm^{-2}_{Pt}$ to obtain the real Pt surface area of 3.98 cm^2. The total surface area of Pt was calculated for 6.8 nm particles as determined by XRD. The platinum utilization efficiency was estimated to be 42% when 2-5 µL of catalyst ink were deposited.

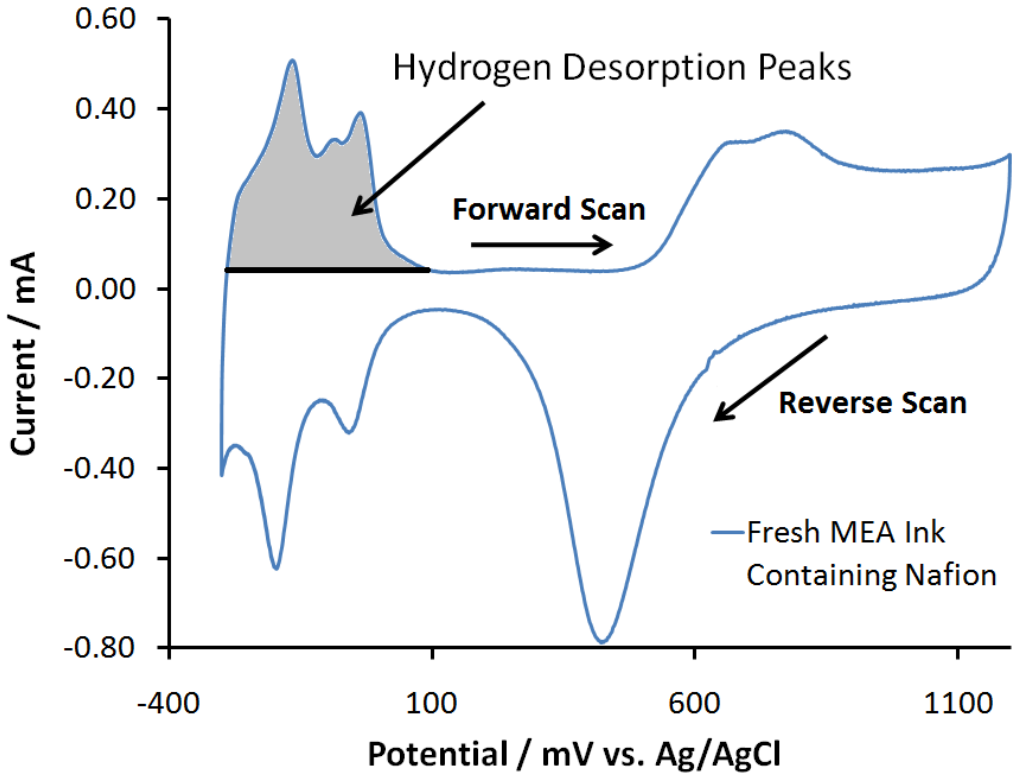

Figure 4.3: Half-cell CV for 2 µL ink deposit containing Nafion solution

The mass of Pt in the ink deposit is calculated using the weight composition of harvested catalyst material determined by TGA. The ink was prepared using 10.5 mg of dry catalyst material. Since the catalyst material is 90% Pt by weight, the total mass of Pt in the ink was 9.45 mg. The total volume of ink was 500 µL (400 µL isopropyl alcohol plus 100 µL 5% Nafion solution). Therefore, the 2 µL ink deposit contained 0.0378 mg of Pt on the glassy carbon electrode. Real Pt surface area was plotted against mass of Pt for a series of ink deposits in Figure 4.4. A line of best fit was plotted in Microsoft Excel 2007 and the slope gave the ECSA as 15.8 ± 3.4 $m^2_{Pt}g^{-1}_{Pt}$ for catalyst material harvested from a fresh sensor and prepared as an ink containing 30 wt. % Nafion. Note that the point in Figure 4.4 at 2.43 E-03 m^2 and 9.45 E-05 g is not used to find the slope because it gives a calculated ECSA of 25.7 $m^2_{Pt}g^{-1}_{Pt}$, which is more than 2 standard deviations from the average ECSA value. The total Pt loading in a sensor electrode was found to be 26.1 mg using ICP-OES. Together, the ECSA and Pt loading indicate an overall Pt surface area of approximately 0.898 m^2 per electrode.

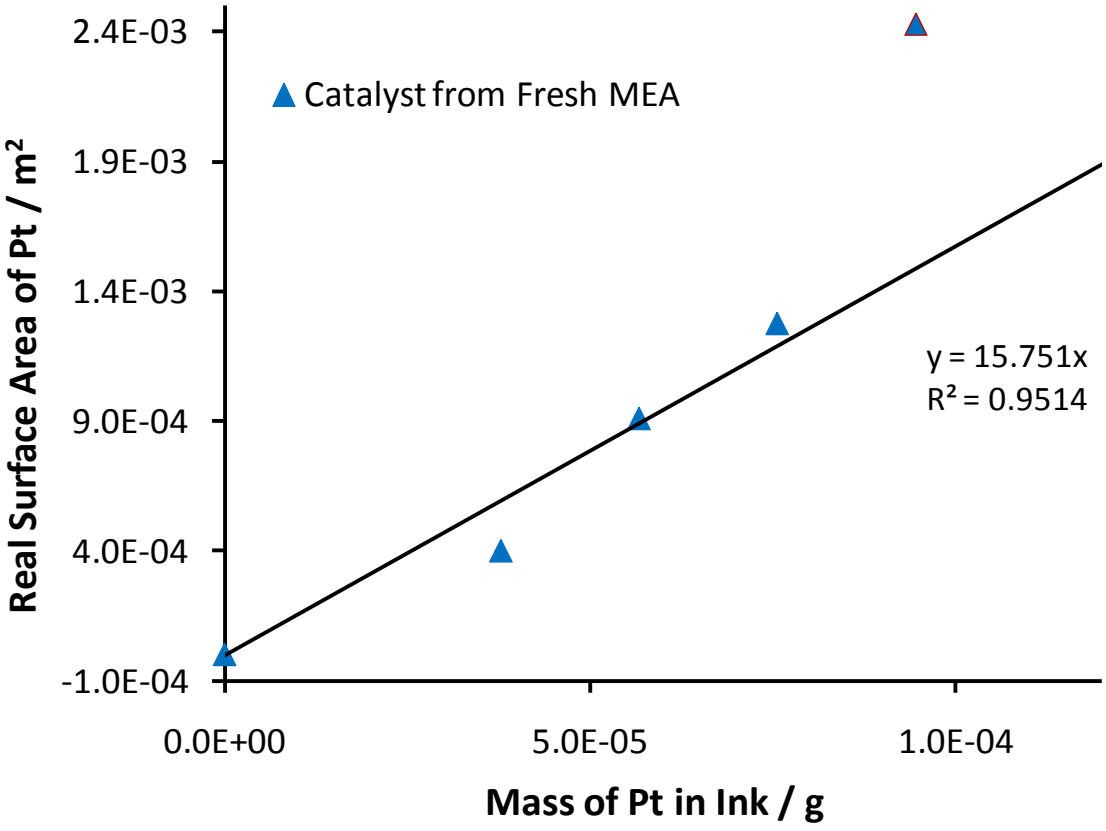

Figure 4.4: Determination of the Electrochemically Active Surface Area of Pt for a catalyst ink prepared using catalyst material harvested from a fresh sensor and 30 wt. % Nafion

The Pt utilization efficiency and ECSA of Pt determined for the sensor catalyst are low compared with other catalyst inks reported in the literature. For example, an ECSA of approximately 70 $m^2_{Pt}g^{-1}_{Pt}$ and Pt utilization of 65% were reported for a catalyst ink containing 20 wt.% Pt on Vulcan carbon XC-72 (E-Tek, 2.6 nm Pt particles) and 30 wt.% Nafion.[27] The higher ECSA of the commercial catalyst is partially due to smaller particle size (2.6 nm compared with 6.8 nm).[27] However, even with comparable Nafion content the sensor catalyst achieved less than half the ECSA of the common carbon-supported Pt catalyst. The low ECSA and Pt utilization efficiency of just 42 % for the sensor catalyst ink are not surprising considering the extent of Pt agglomeration observed by TEM (Figure 3.5).

Dispersing the 6.8 nm Pt particles on a carbon black material with high surface area such as Vulcan XC-72 would reduce agglomeration and allow the ECSA and Pt utilization to better reflect the individual Pt particle size. Alternatively, the Pt black catalyst in the sensor electrodes could be replaced with a commercially available carbon-supported Pt catalyst such as E-Tek 20 wt.% Pt on Vulcan XC-72. The overall Pt loading could then be reduced while maintaining the same ECSA because the Pt utilization efficiency would be improved. Using E-Tek 20 wt.% Pt on Vulcan XC-72 and assuming ECSA of 70 $m^2_{Pt}g^{-1}_{Pt}$ as reported above, the Pt loading in the sensor electrodes could be reduced by half. In this way, the total surface area of 0.898 m^2 that was calculated for the sensor catalyst with Nafion ionomer could be achieved using just 12.8 mg of Pt.

The ECSA of 15.8 $m^2_{Pt}g^{-1}_{Pt}$ represents the maximum achievable ECSA in the sensor electrodes. Half-cell cyclic voltammetry is performed in optimal conditions where the catalyst layer is completely wetted by the liquid electrolyte. All accessible Pt sites are in contact with the electrolyte and contribute to the ECSA measurement. In the actual sensor operating mode, the electrodes are fed with gaseous reactants. At low pressure these reactants do not necessarily reach all of the Pt sites. Therefore, the actual ECSA of an operating sensor would be smaller, even as much as 50% smaller than the value obtained using the half-cell measurement.[36] Furthermore, the presence of Nafion in the catalyst ink most likely increases the proton conductivity within the catalyst layer, resulting in a higher measured ECSA.[55] The sensor electrodes do not contain an ionomer, since the fluoropolymer binder is not proton-conducting. Therefore, the half-cell ECSA measurement is even more inflated. To investigate the improvement in ECSA resulting from adding Nafion solution to the catalyst layer, a catalyst ink was prepared without adding Nafion solution.

4.3 Effect of Adding Nafion into the Catalyst Layer on the ECSA of Pt

To prepare a catalyst ink without Nafion solution, 11.0 mg of catalyst material were harvested from another fresh MEA and mixed with 500 µL 50:50 IPA:H_2O solution. Half-cell cyclic voltammetry was performed for a series of ink deposits on glassy carbon electrodes in 0.5 M sulfuric acid. Sample CVs are shown in Figure 4.15 for 2 µL deposits of catalyst inks prepared with and without Nafion solution. The Pt loadings were approximately equivalent for the two ink deposits. The ink without Nafion contained 0.040 mg of Pt, slightly higher than 0.0378 mg for the ink with Nafion. The ink deposit containing Nafion solution generated much larger hydrogen adsorption/desorption peaks.

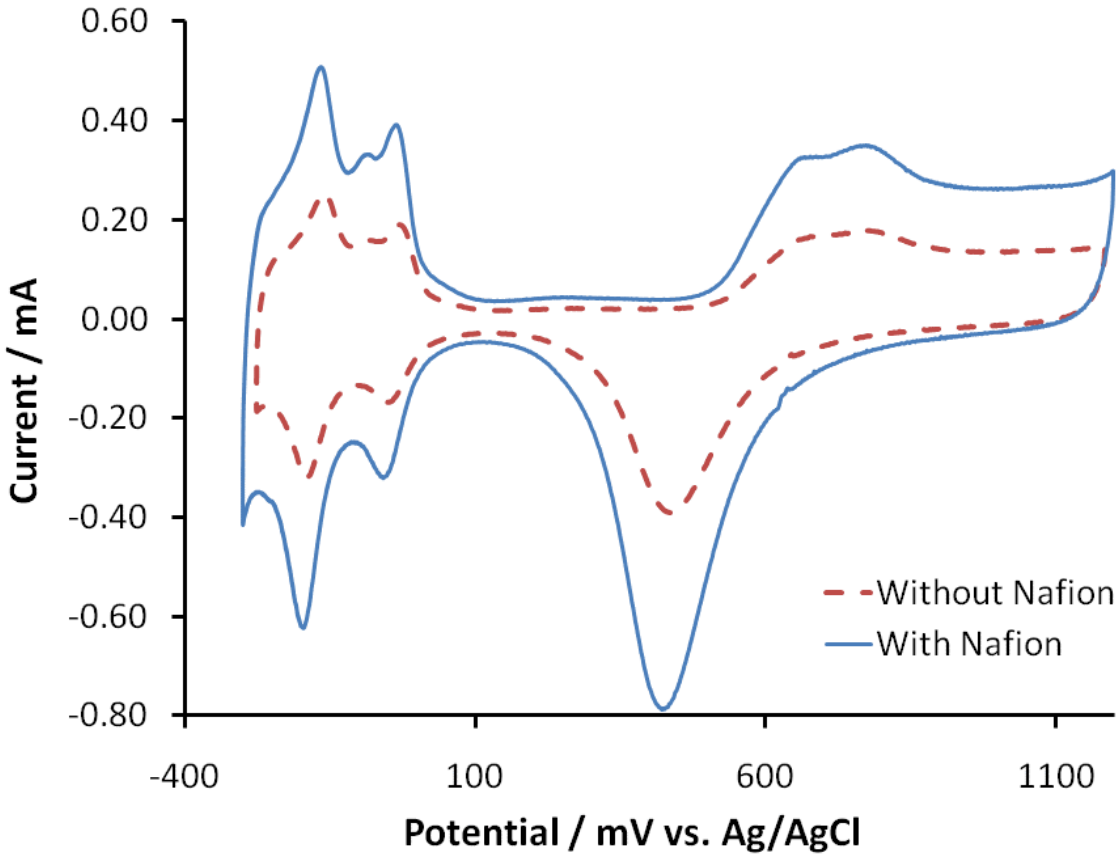

Figure 4.5: Half-cell cyclic voltammograms for 2 µL deposits of catalyst inks prepared with or without Nafion solution

The ECSA of Pt was estimated for the two ink samples using the slope of the line of best fit in Figure 4.6. The line of best fit for ink without Nafion is very poor, however the slope suggests an ECSA of 9.9 ± 5.7 m^2g^{-1}. This is slightly lower than the ECSA of 15.8 m^2g^{-1}measured for the catalyst ink containing Nafion. The addition of Nafion most likely improved proton transport through the catalyst material to the Pt surface, thereby making more of the Pt surface accessible and catalytically active.

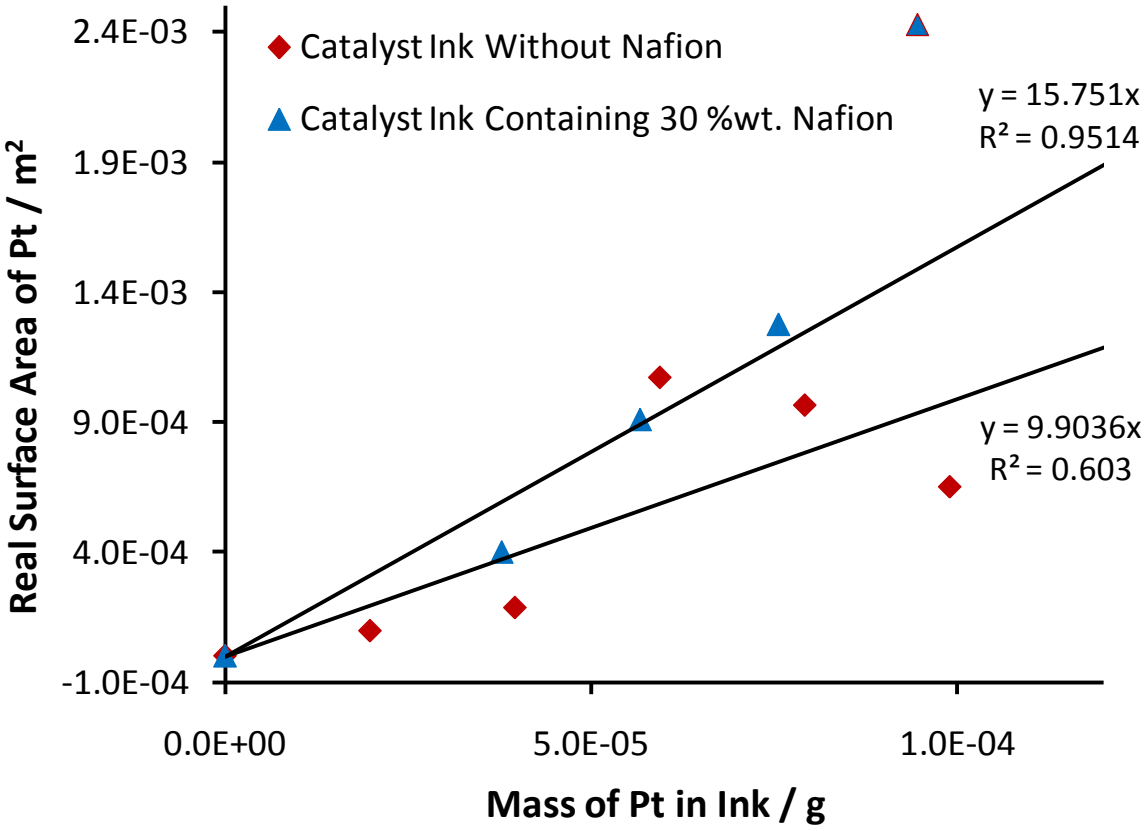

Figure 4.6: Determining ECSA for catalyst inks prepared with and without Nafion

4.4 Onset Potential for Ethanol Oxidation at the Pt Surface of Harvested Catalyst Material

Linear sweep voltammetry (LSV) was used to measure the onset potential for ethanol oxidation at the Pt surface of harvested catalyst material. Figure 4.7 shows the LSVs for a catalyst ink in 0.5 M sulfuric acid solution with and without 1.0 M ethanol solution. Subtracting the LSV for sulfuric acid from the LSV for sulfuric acid + ethanol gives the LSV for ethanol oxidation at the electrode. The onset potential for ethanol oxidation by the sensor catalyst occurs at approximately 600 mV vs. Ag/AgCl. One way to evaluate new catalyst formulations for next generation sensors would be to compare their onset potentials for ethanol oxidation against the value determined for the current sensor catalyst. Lower onset potential for ethanol oxidation is more desirable.

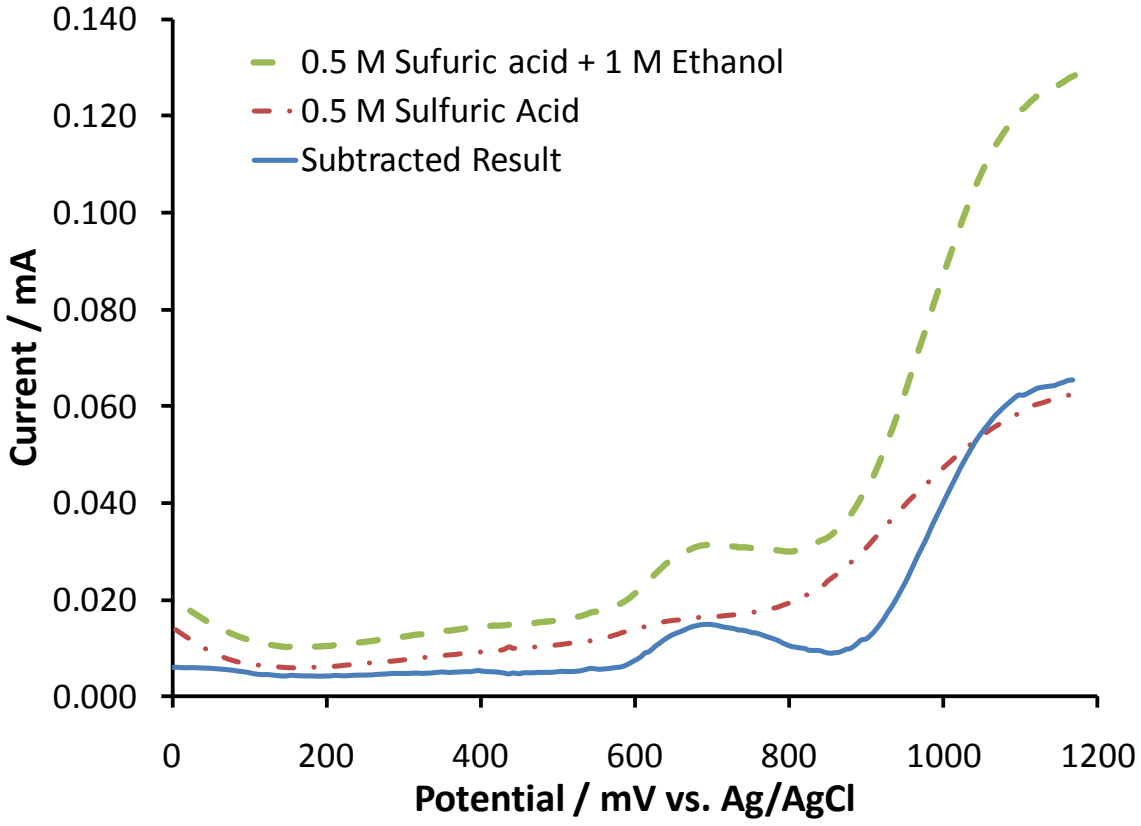

Figure 4.7: Linear sweep voltammograms for catalyst ink in 0.5 M sulfuric acid solution with and without 1.0 M ethanol to determine onset potential for ethanol oxidation

4.5 Sensory Performance Determined by Dose Response Calibration Experiments

4.5.1 Sensitivity of Fresh Sensors

A dose response calibration was performed to evaluate the sensory performance of a fresh sensor. Ionic resistance of the membrane was determined to be 3.72 Ω by making an EIS measurement of the fresh sensor before the dose response experiment. The dose response curve is shown in Figure 4.8. Injections of a blank sample did not result in any noticeable current response. Peaks with increasing height were generated as the sample concentrations increased from 0.010 BAC to 0.150 BAC. The first two peaks for a given sample seemed to be required to purge the tube connecting the sensor to the sample headspace. During these two measurements the tube contained a mixture of the previous, less concentrated vapour and the current, more concentrated vapour. This produced smaller peaks for the first two injections. However, by the third injection the peak heights tended to level off for the remaining injections.

Figure 4.9 shows an individual peak produced by a 0.150 BAC injection in the dose response experiment. As ethanol was consumed at the anode the current spiked sharply and decayed back to the baseline. The current responded almost instantly after each dose injection and returned to baseline within approximately 15 seconds. This allowed for rapid dose response data acquisition.

Corrview software was used to integrate the area under the peak in Figure 4.9 to determine the charge produced. The integration limits were manually selected to include the entire peak until the current returned to the established baseline. All peak integrations to determine charge were done using the peaks with reproducible heights.

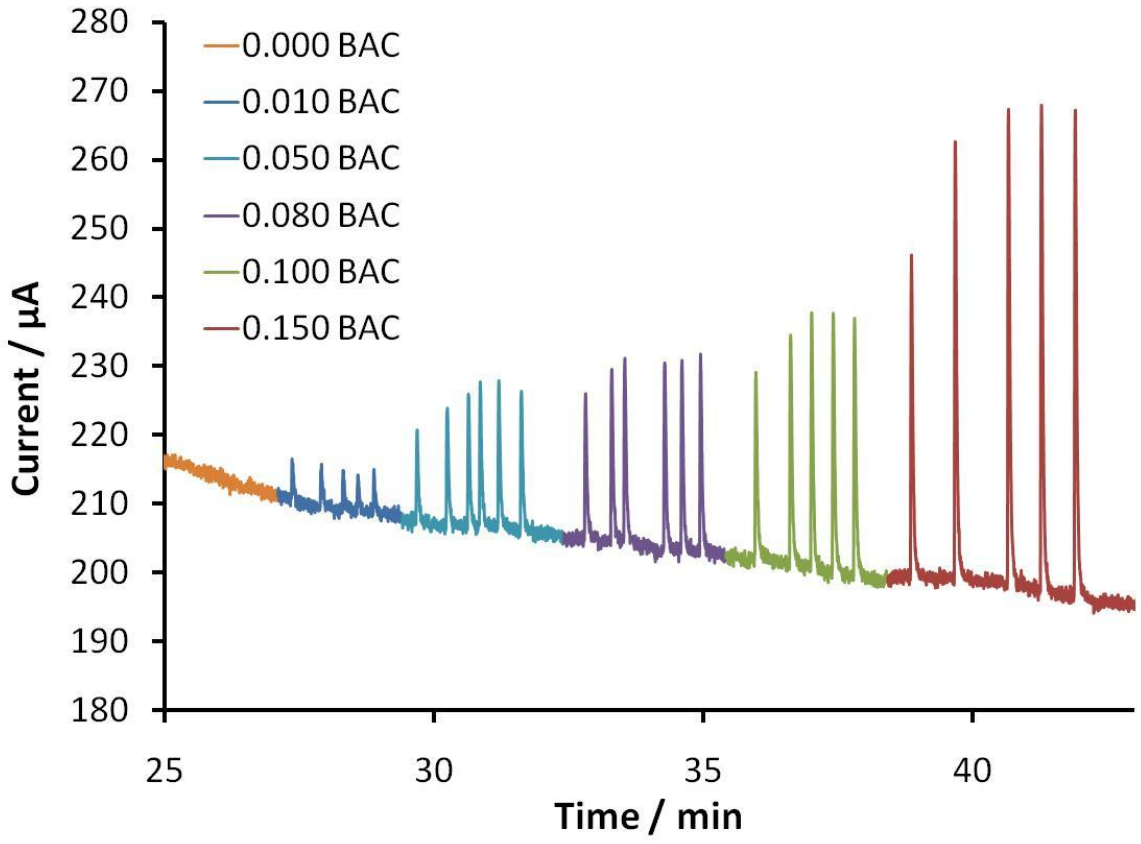

Figure 4.8: Dose response calibration plot for a fresh sensor

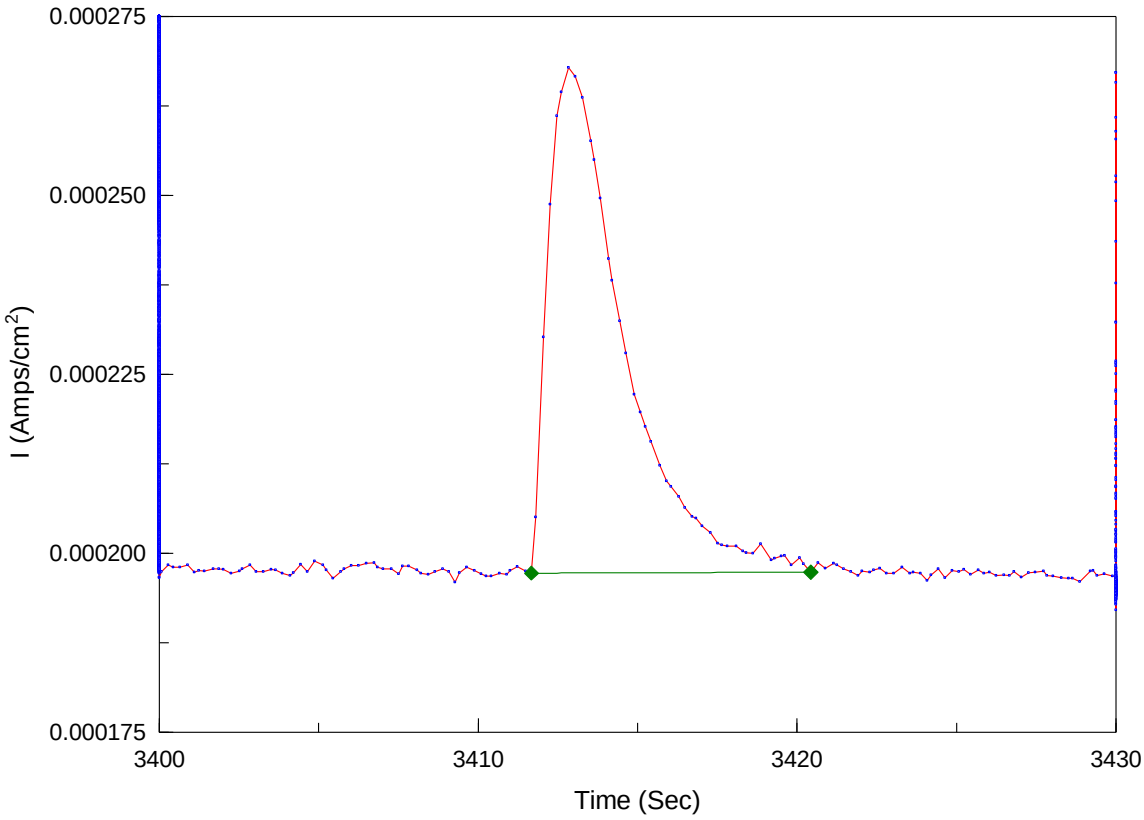

Figure 4.9: Zoomed view of an individual peak produced by a dose response for a 0.150 BAC sample

After calculating the charge for each peak, the average charge for each sample concentration was plotted vs. the amount of ethanol injected. The sensitivity calibration plot for the fresh sensor is shown in Figure 4.10. The slope of the line of best fit indicates a sensitivity of 0.91 µC g_{Pt}^{-1} $nmol_{ethanol}^{-1}$. This value serves as a reference with which to compare the sensitivity after accelerated membrane dehydration testing.

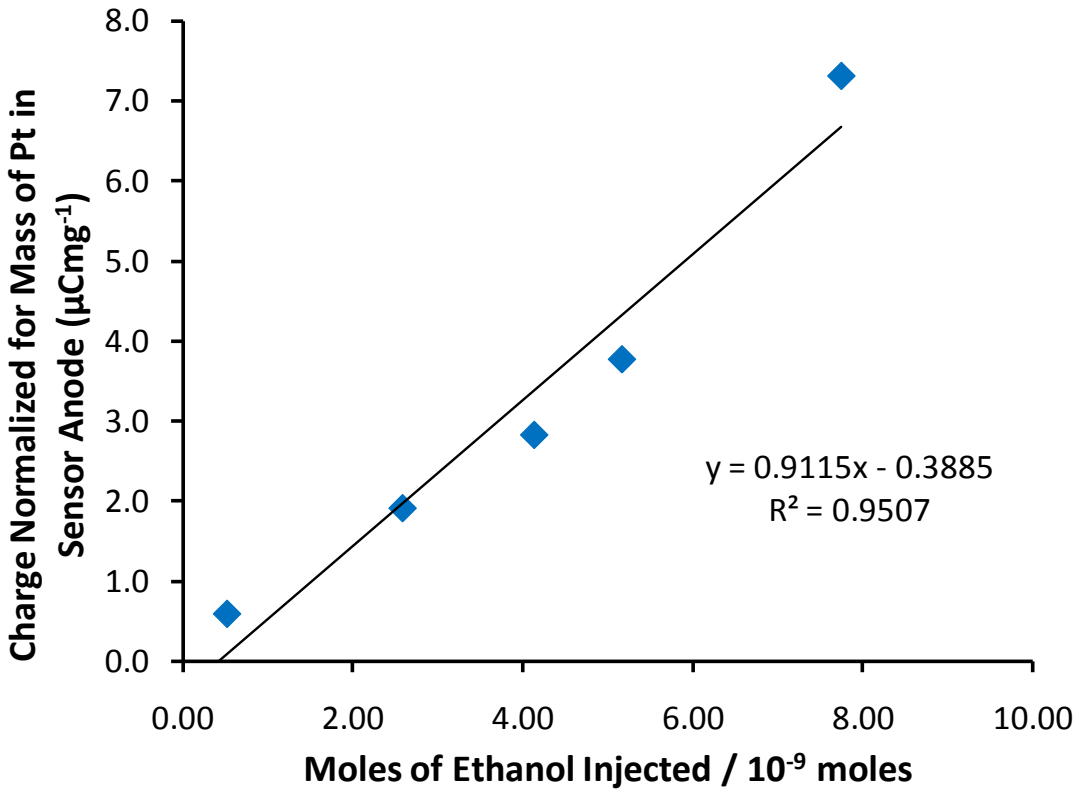

Figure 4.10: Sensitivity calibration plot for fresh sensor with a high frequency resistance value of 3.72 Ω

4.5.2 Sensitivity of Sensors of Various Ages

Dose response experiments were performed to determine the sensitivity of a series of sensors of various ages. It was expected that older sensors would be less sensitive than newer sensors as a result of degradation over time. Figure 4.11 displays the sensitivity values obtained for a fresh sensor from 2010 and a series of used sensors made between 2003 and 2008. There is no real trend in sensitivity with sensor age. The sensors from 2005 and 2006 displayed higher sensitivity than the fresh sensor. The 2004 sensor was somewhat less sensitive than the fresh sensor and the sensors from 2003 and 2008 were much less sensitive. These results are in agreement with the results from section 4.1 which showed the ionic resistance of the membrane is not determined by the age of the sensor. Degradation of sensor performance seems to depend on the specific conditions the sensor was exposed to over its lifetime including the in-plant

humidity conditions where the sensors were assembled. This will be discussed in more depth in chapter 5.

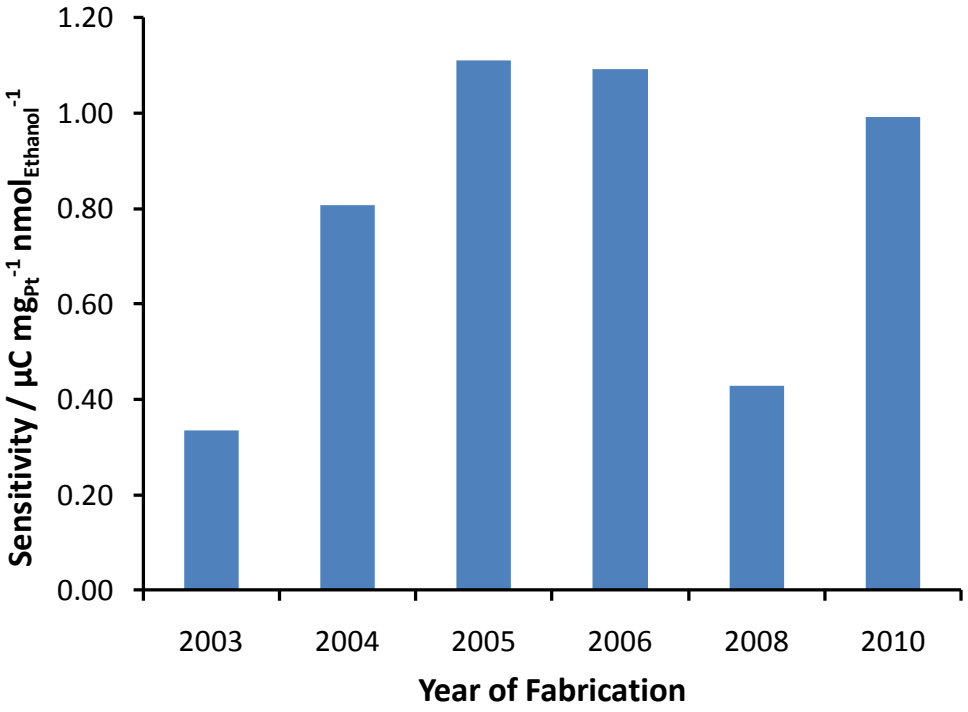

Figure 4.11: Sensitivity comparison among a fresh sensor made in 2010 and used sensors made between 2003 and 2008

Chapter 5 - Investigation of Sensor Degradation in Low-humidity Conditions

5.1 Introduction to Accelerated Humidity Cycling of Breath Alcohol Sensors

Accelerated humidity cycling tests were conducted to simulate extremely dry or humid conditions and the impact on sensor properties and overall sensory performance was investigated. Accelerated humidity cycling was performed on fully assembled sensors or MEAs removed from the sensor cells. Removing the MEA from a sensor allows the entire MEA to be fully and equally exposed to the imposed conditions. The anode is most vulnerable to humidity fluctuations because the anode compartment of the cell is open to the atmosphere. The membrane can also become hydrated and dehydrated when the sensor is exposed to varying humidity conditions. Since the cathode is sealed within an air-tight compartment on the far side of the membrane, it is least accessible to humidity from the atmosphere.

Sensors and MEAs were exposed to humidity cycling using two different techniques. One method was to allow sensors or MEAs to equilibrate for 12 hours in the humidity chamber at constant temperature and relative humidity. The other method involved purging dry or humidified N_2 over the anode inside an assembled sensor. Both techniques achieved accelerated hydration and dehydration but in slightly different ways. The effects of each technique were investigated.

5.2 Accelerated Humidity Cycling of Assembled Sensors

5.2.1 Ionic Resistance of Membranes in Sensors Equilibrated in a Humidity Chamber

In this test, three sensors of different ages underwent accelerated humidity cycling to investigate the effect of sensor age on membrane resistance behavior. The sensors were first equilibrated in dehydrating conditions (30% RH) before cycling to 95% RH and then back to 50% RH. The sensors were exposed to constant temperature and RH conditions for 12 hours before being briefly removed from the humidity chamber to obtain an EIS measurement.

Figure 5.1 compares the ionic resistance sensors made in 2004, 2007 or 2010 at 25 °C while varying the hydration of the membrane. As might be expected, the fresh

sensor (2010) began with the lowest membrane resistance. However, the sensor with the highest HFR was the medium-aged sensor (2007). After the initial equilibration at 30% RH the 2010 sensor had an HFR of 2.38 Ω while the used sensors from 2004 and 2007 had HFR values of 3.10 and 4.35 Ω respectively.

All three sensors exhibited decreasing membrane resistance as the sensors were equilibrated in increasingly humid conditions. Interestingly, all three sensors achieved a minimum HFR of 0.70-0.78 Ω under fully hydrated conditions (RH> 90%). The proton conductivity of the fully hydrated sensors is comparable with the conductivity of hydrated Nafion membranes. Values reported for the proton conductivity of Nafion vary depending on the membrane pre-treatment and the conditions of the measurement.[38] Typical values are approximately 0.1 Scm^{-1} for Nafion 112 and 0.06 Scm^{-1} for Nafion 117.[56] In low humidity conditions the conductivity of Nafion decreases substantially.

As the equilibration RH decreased from 95% to 70% the HFR values remained fairly constant for all three sensors. Below 70% the three sensors showed markedly different behavior. The 2010 sensor experienced a very small increase in membrane resistance, up to 0.77 Ω at 50% RH. The resistance of the 2004 sensor increased to 1.35 Ω, just slightly lower than its value of 1.58 Ω at 50% RH during the hydration phase. The membrane resistance of the 2007 sensor jumped to 4.07 Ω at 60% RH, followed by 4.60 Ω at 50% RH.

Membrane proton conductivity appears to decrease after a sensor has been in use for a period of time. However, conductivity does not appear to be correlated with sensor age. Rather, the conditions experienced by a sensor over its lifetime probably have the greatest impact on membrane conductivity.

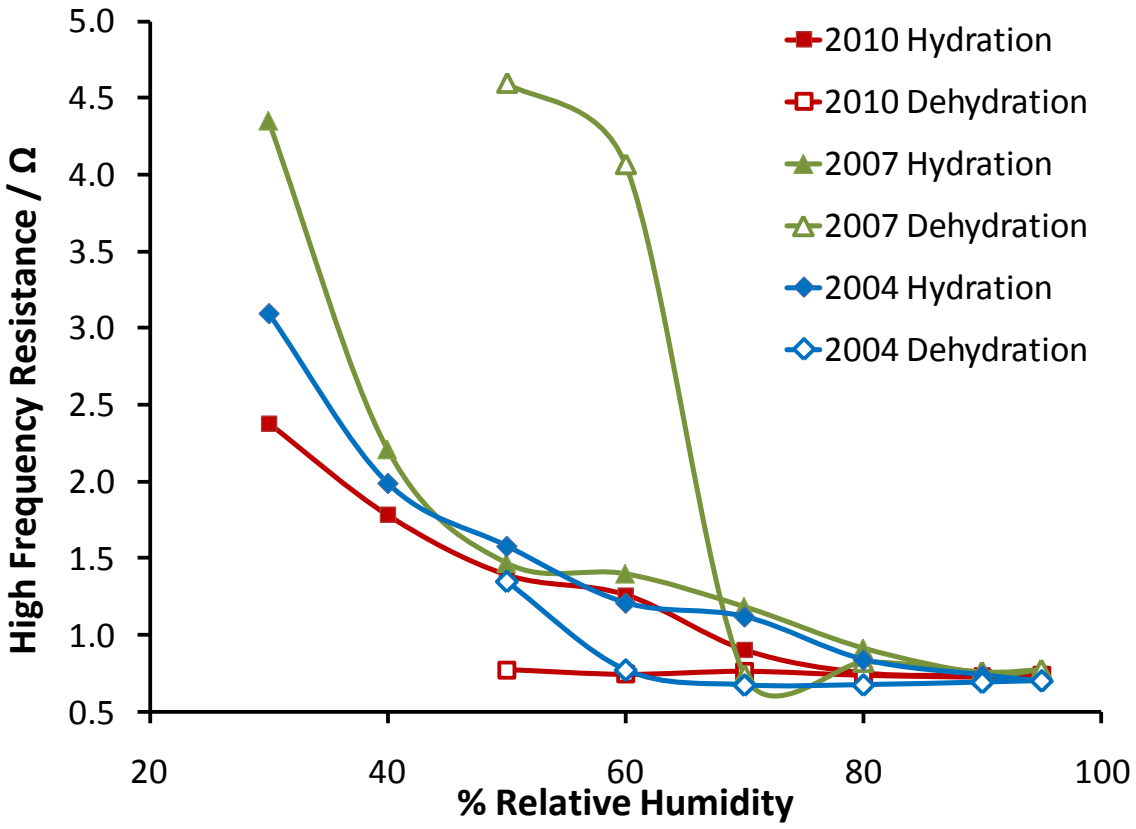

Figure 5.1: Membrane resistance for sensors equilibrated at 25 °C and different RH values

5.2.2 Ionic Resistance of Membranes in Sensors Equilibrated in Hydrating Conditions and Dehydrated by Flowing N_2

In practice, sensors typically do not equilibrate under constant temperature and humidity conditions over the long term. They are constantly exposed to changing atmospheric and operating conditions which could affect the hydration and proton conductivity of the PEM. The stability and recoverability of membrane proton conductivity was investigated as the membrane hydration was cycled. Figure 5.2 shows the Nyquist plots for a sensor undergoing accelerated membrane dehydration cycling. The HFRs move to progressively higher values over time as the membrane is dehydrated. Ionic resistance of the membrane increased with time under flowing dry N_2.

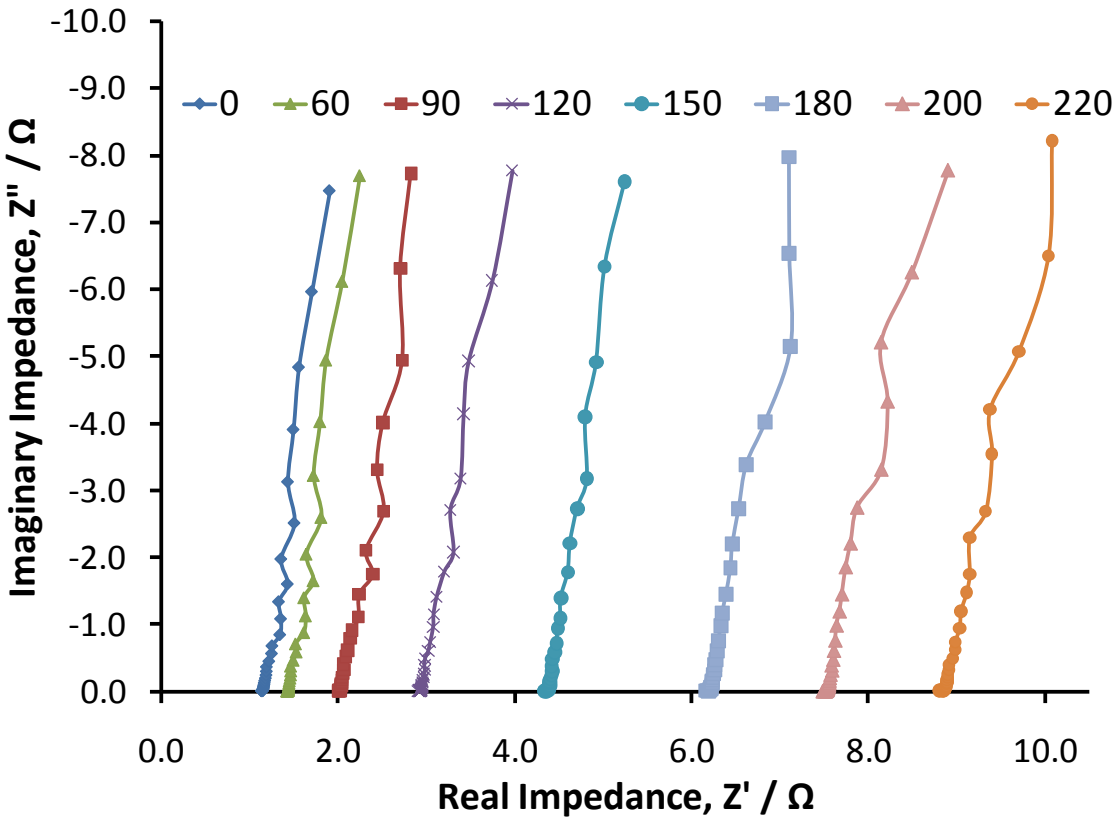

Figure 5.2: Nyquist plots for a sensor undergoing accelerated membrane dehydration cycling under flowing N_2

Figure 5.3 shows the HFR (a) and proton conductivity (b) of the sensor for two cycles of accelerated membrane dehydration cycling. Note that the ionic resistance of the membrane increased more slowly on day 2 because the flow rate of N_2 dipped after about 15 minutes. As a result, the membrane dried out more slowly and less overall on the second day.

On the first day of measurements the HFR started at 5.01 Ω and increased to 7.13 Ω. After re-hydrating the membrane overnight in the humidity chamber, the initial HFR on the second day returned to 5.06 Ω. This demonstrates that after a membrane has been dried out for a short period of time, proton conductivity can be recovered by rehydrating the membrane in a humid environment. Short-term exposure to dry conditions did not lead to an irreversible loss of proton conductivity. The next study looks at the recoverability of proton conductivity after multiple cycles of membrane

hydration and dehydration. It also uses more extreme limits for humidity cycling than were used in the current study.

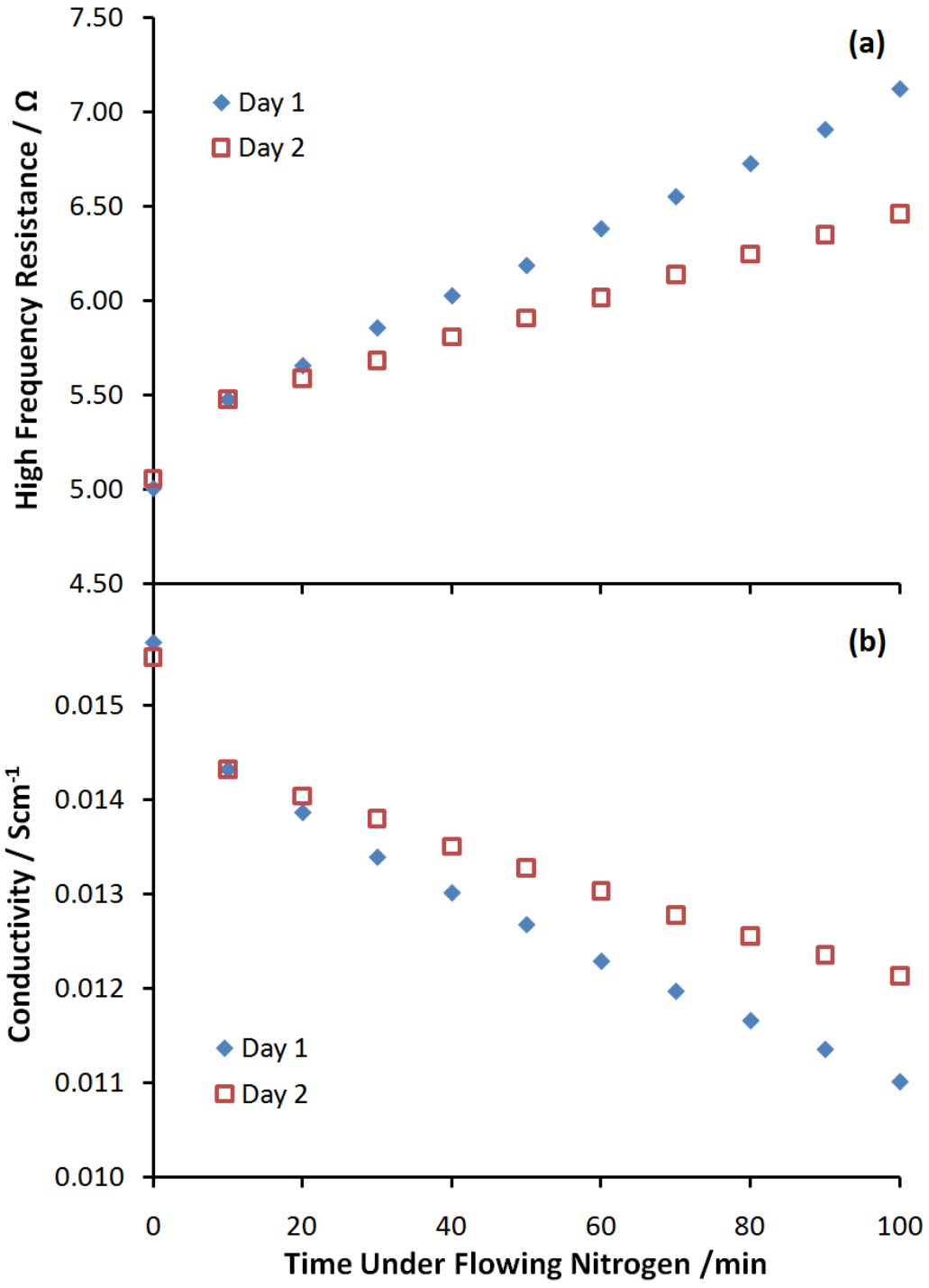

Figure 5.3: High frequency resistance and proton conductivity of a sensor undergoing accelerated membrane dehydration cycling

5.2.3 Ionic Resistance of Membrane in Sensors Hydrated and Dehydrated by Flowing N_2

The previous study showed the increase in ionic resistance of the membrane to be reversible after one cycle of membrane dehydration. In this section, the recoverability of proton conductivity after a sensor undergoes multiple cycles and greater extents of membrane dehydration. Figure 5.4 illustrates the change in ionic resistance of the membrane as it is repeatedly hydrated and then immediately dehydrated. The minima represent the ionic resistance of the membrane when it is fully hydrated. After the first hydration the HFR reaches a minimum value of 0.91 Ω. The seven subsequent cycles generated HFR values of 1.14, 0.93, 0.87, 1.03, 1.04, 1.03 and 0.96 Ω.

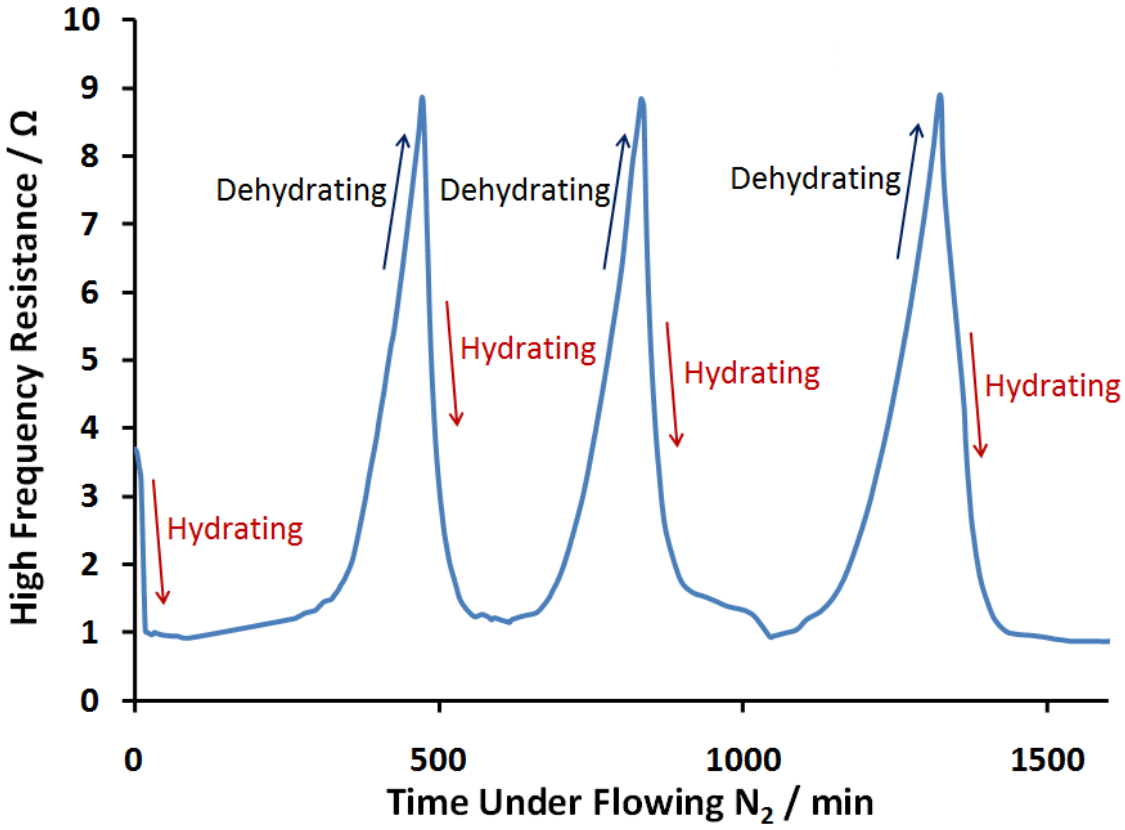

Figure 5.4: Ionic resistance of the membrane during accelerated hydration-dehydration cycling by alternating dry and humidified N_2

Figure 5.5 is a plot of the HFRs on a logarithmic scale for all seven cycles. The log scale is more convenient for displaying the data from the final two cycles along with the first five cycles. It is important to note that the membrane resistance returns to approximately its initial fully hydrated value after each cycle. Particularly after the final cycle when the membrane was drastically dehydrated. This confirms the recoverability of proton conductivity by re-hydrating the membrane after it has been dried out multiple times. It also shows that even extreme dehydration does not cause irreversible loss of membrane conductivity.

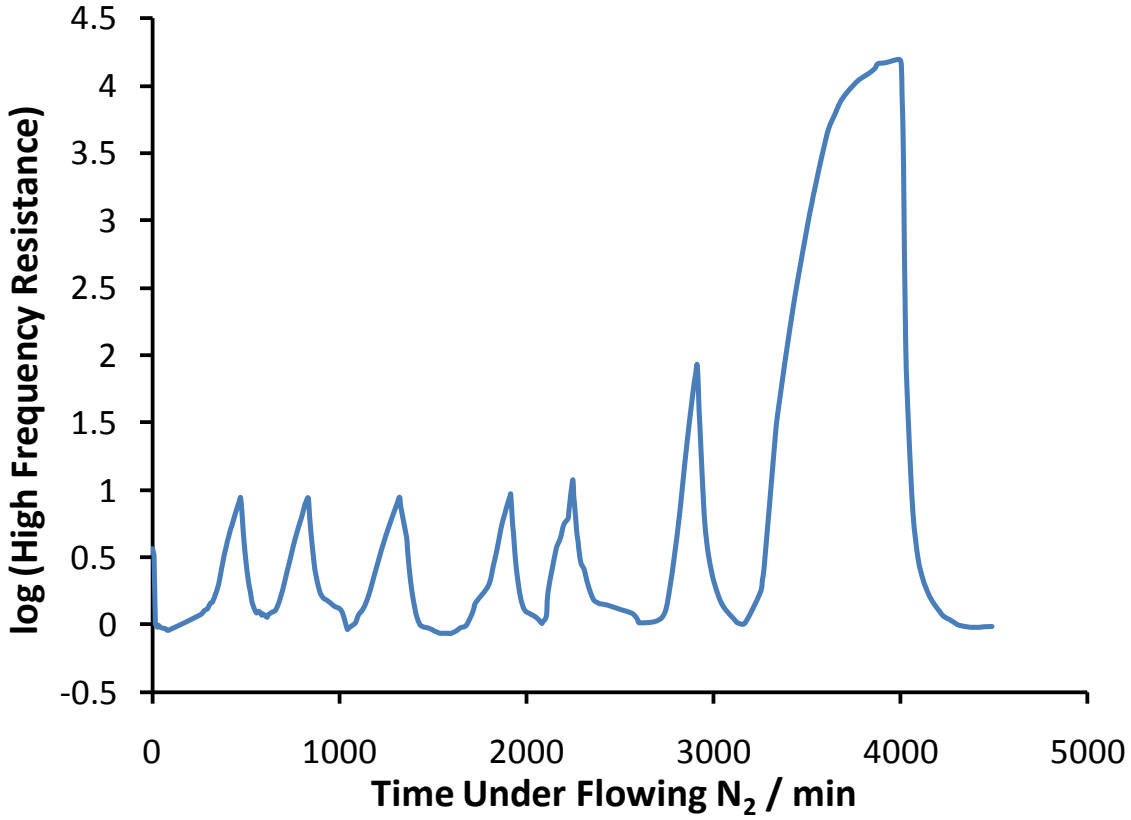

Figure 5.5: Log scale of membrane resistance during accelerated hydration-dehydration cycling under alternating dry and humidified N_2

5.2.4 Sensory Performance after Accelerated Humidity Cycling by Flowing N_2

Loss of membrane proton conductivity as a result of exposure to low-humidity conditions was demonstrated to be reversible in the previous two studies. This study looks at sensory performance after the accelerated humidity cycling. Sensitivity curves were obtained for the sensor that was used in the long-term accelerated membrane dehydration testing in the previous section (5.2.3). Dose response experiments were performed immediately before and after accelerated hydration cycling and at various levels of membrane hydration after cycling.

Figure 5.6 summarizes the sensitivity values obtained at various levels of membrane resistance before and after accelerated membrane hydration cycling. Each sensitivity value is associated with a dose response experiment, labeled DR1 through DR5. DR1 is the dose response for the fresh sensor, as discussed above. DR2 is the dose response experiment performed immediately following the final hydration step of the accelerated membrane dehydration cycling. At that point the membrane resistance was very low, with a HFR value of 1.01 Ω. The sensitivity obtained by DR2 was 1.73 μC g_{Pt}^{-1} $nmol_{ethanol}^{-1}$, nearly double the sensitivity obtained by DR1 when the membrane resistance was 3.72 Ω. Similarly, DR3 was performed with a high membrane resistance of 14.88 Ω. The sensitivity obtained by DR3 was quite low at 0.48 g_{Pt}^{-1} $nmol_{ethanol}^{-1}$.

For DR4 the membrane resistance was returned to almost the equivalent value exhibited by the fresh sensor before DR1. DR4 was performed with a resistance of 3.52 Ω, just slightly lower than 3.72 Ω for DR1. The dose response plot for DR4 is shown in Figure 5.7.

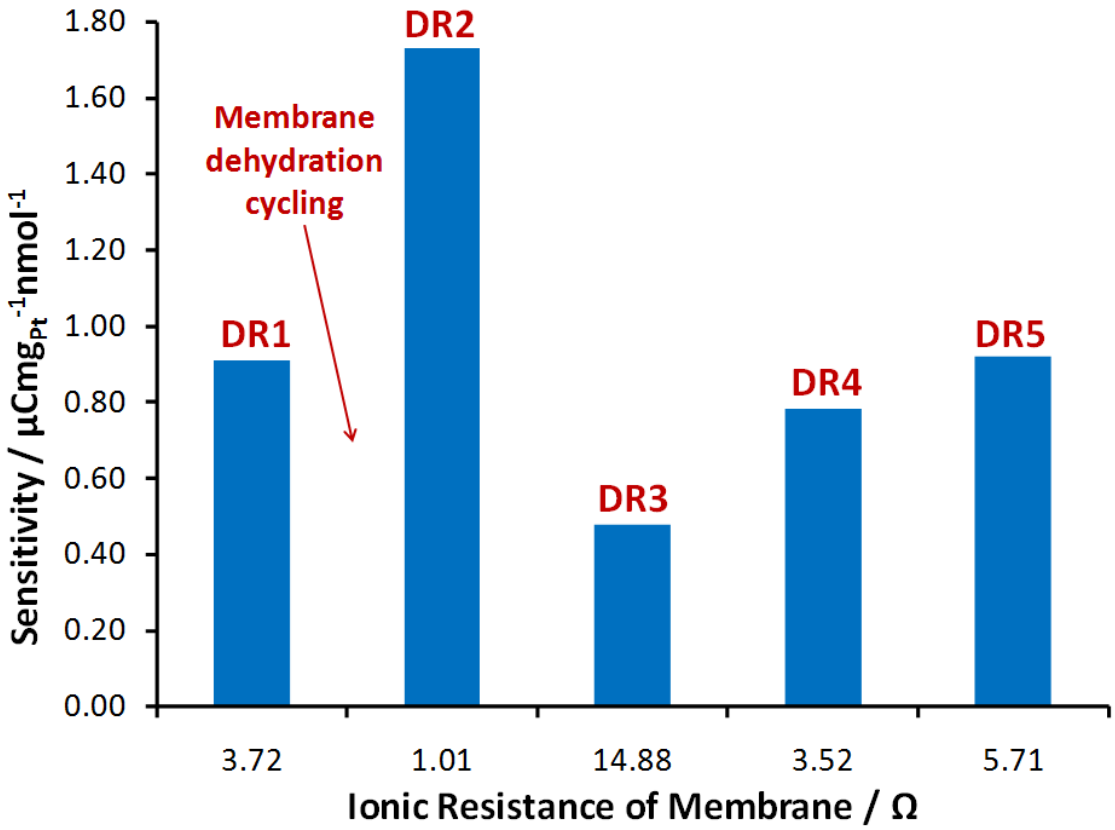

Figure 5.6: Sensitivity values corresponding to a series of dose response experiments before and after membrane hydration cycling of a sensor. DR1 corresponds to the sensitivity measured by a dose response experiment for a fresh sensor with a HFR value of 3.72. DR2 through DR5 correspond to the same sensor with different values of HFR after undergoing humidity cycling.

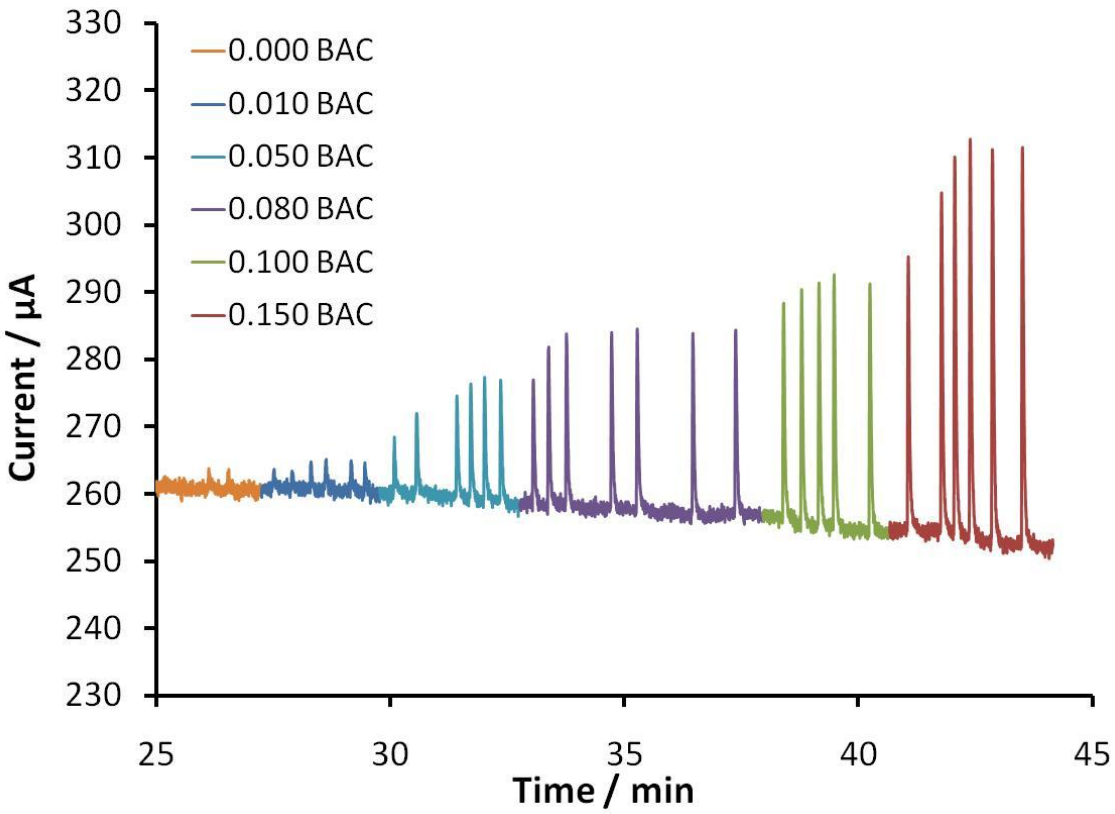

Figure 5.7: Dose response plot for sensor after accelerated membrane dehydration cycling, with a high frequency resistance value of 3.52 Ω

Figure 5.8 shows the dose responses with the same membrane resistance from before (DR1) and after (DR4) accelerated membrane dehydration cycling. DR4 had a slightly higher background current as expected since the membrane resistance was slightly higher. DR4 also produced slightly smaller peaks than DR1 at each sample concentration. It follows that the sensitivity obtained by DR4 was slightly lower than that of DR1. Figure 5.9 is the sensitivity calibration curve for DR4. The sensitivity value was 0.78 µC g_{Pt}^{-1} $nmol_{ethanol}^{-1}$. That corresponds to 14 % lower sensitivity with the same membrane resistance after dehydration cycling.

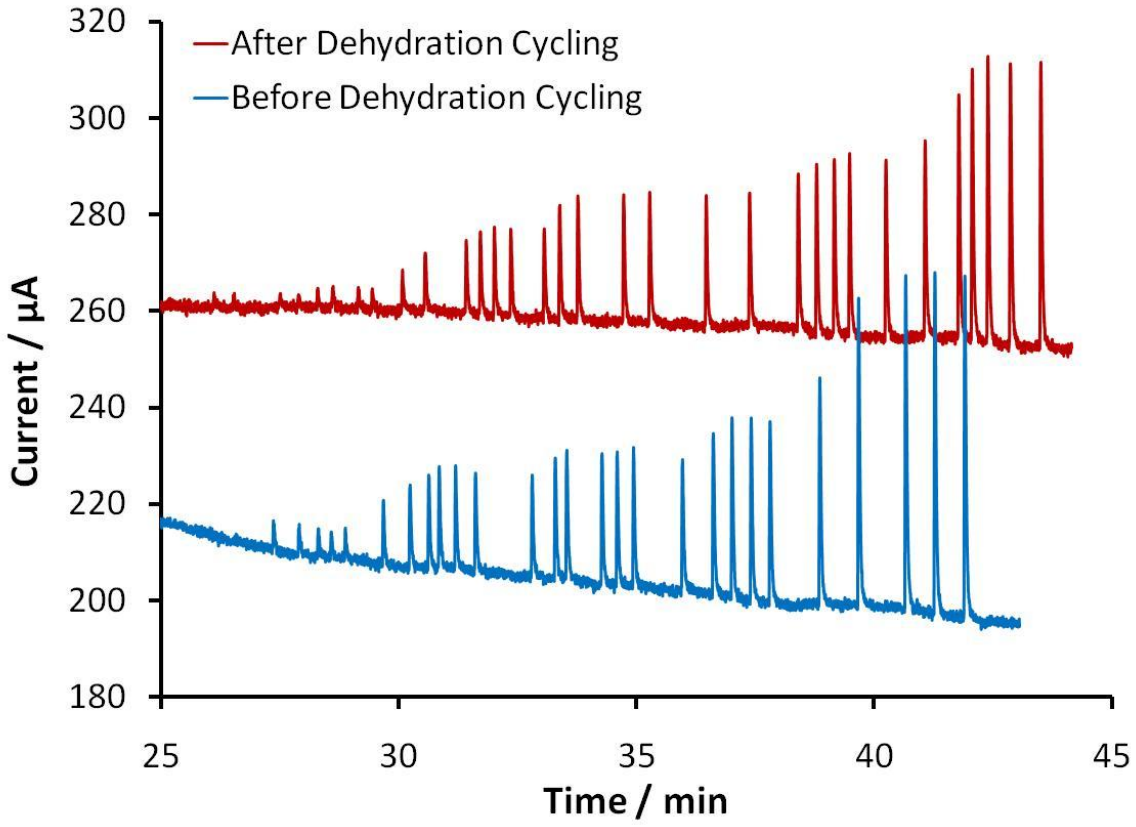

Figure 5.8: Dose response curves for sensor before and after membrane hydration cycling, with high frequency resistances of 3.72 and 3.52 Ω

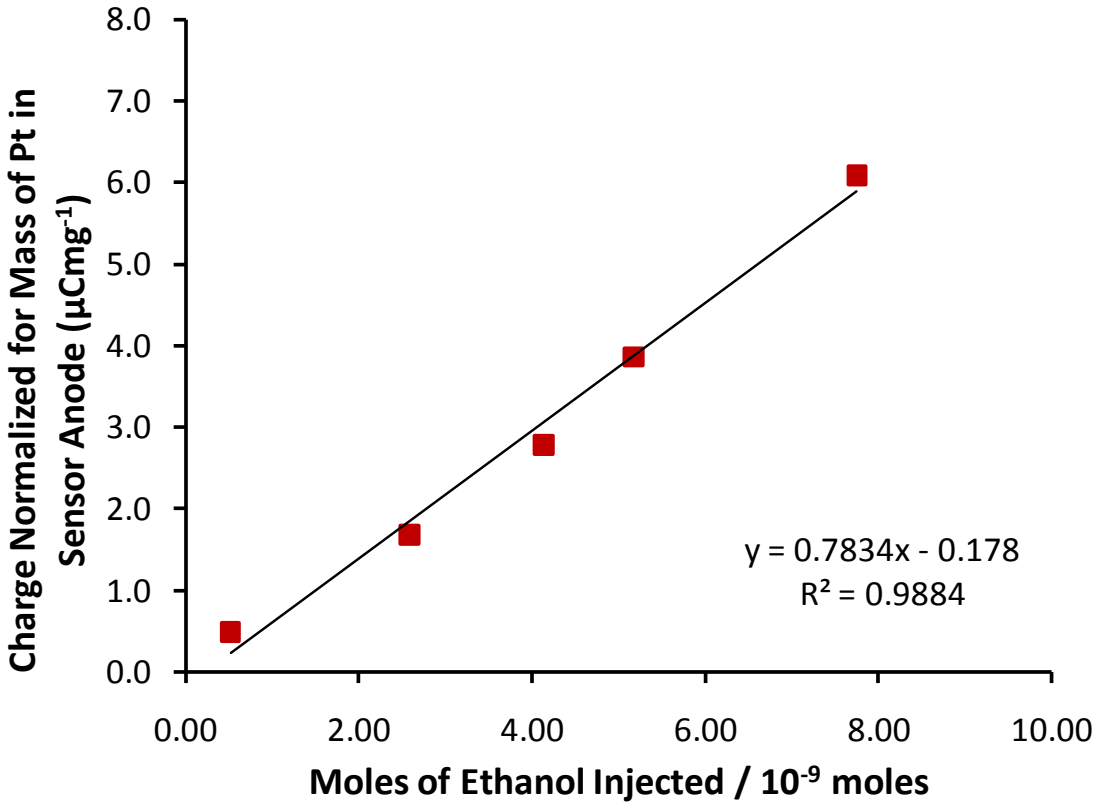

Figure 5.9: Sensitivity calibration plot for sensor after membrane hydration cycling, with a high frequency resistance of 3.52 Ω

Lastly, DR5 was performed with a HFR value of 5.71 Ω, an increase of more than 50% increase over the HFR of the fresh sensor. Interestingly, the sensitivity obtained by DR5 was almost exactly equal to the sensitivity obtained by DR1 with a value of 0.92 µC g_{Pt}^{-1} $nmol_{ethanol}^{-1}$. This indicates that the accelerated membrane dehydration cycling did not have an impact on sensitivity in subsequent dose response experiments. Although sensitivity depends upon the current hydration of the membrane, the sensitivity is reproducible over a range of membrane resistance values.

5.3 Accelerated Humidity Cycling of Sensor MEAs Removed from Cells

5.3.1 Water Uptake of MEA Equilibrated in Controlled Humidity Conditions

This study uses a different technique for accelerated humidity cycling than the previous experiments. Rather than flowing N_2 through the sensor cell, the MEA was removed and allowed to fully equilibrate in controlled humidity conditions. The sensor absorbs water from the atmosphere when it is exposed to humid conditions. Only a small amount of water would be held within the hydrophobic Teflon-bonded electrodes. The majority of absorbed water would be contained in the membrane. The water uptake behavior of the membrane was monitored as the membrane was hydrated and then dehydrated.

The original weight of the MEA was 377.5 mg at 22 °C (room temperature) and RH< 20 %. Figure 5.10 shows how the MEA weight changed as the RH changed at constant temperature. The mass of the MEA increased as the membrane absorbed water from the increasingly humid atmosphere. At 25 °C and 80% RH the MEA became saturated with water at a weight of 449.2 mg, corresponding to 71.7 mg of absorbed water. The weight of the MEA did not increase further after equilibrating the MEA in 25 °C and 90% RH conditions. The MEA weight decreased as the RH was reduced, however it is interesting to note that the weight at each RH was lower during the dehydration phase than it was at the corresponding RH during the hydration phase.

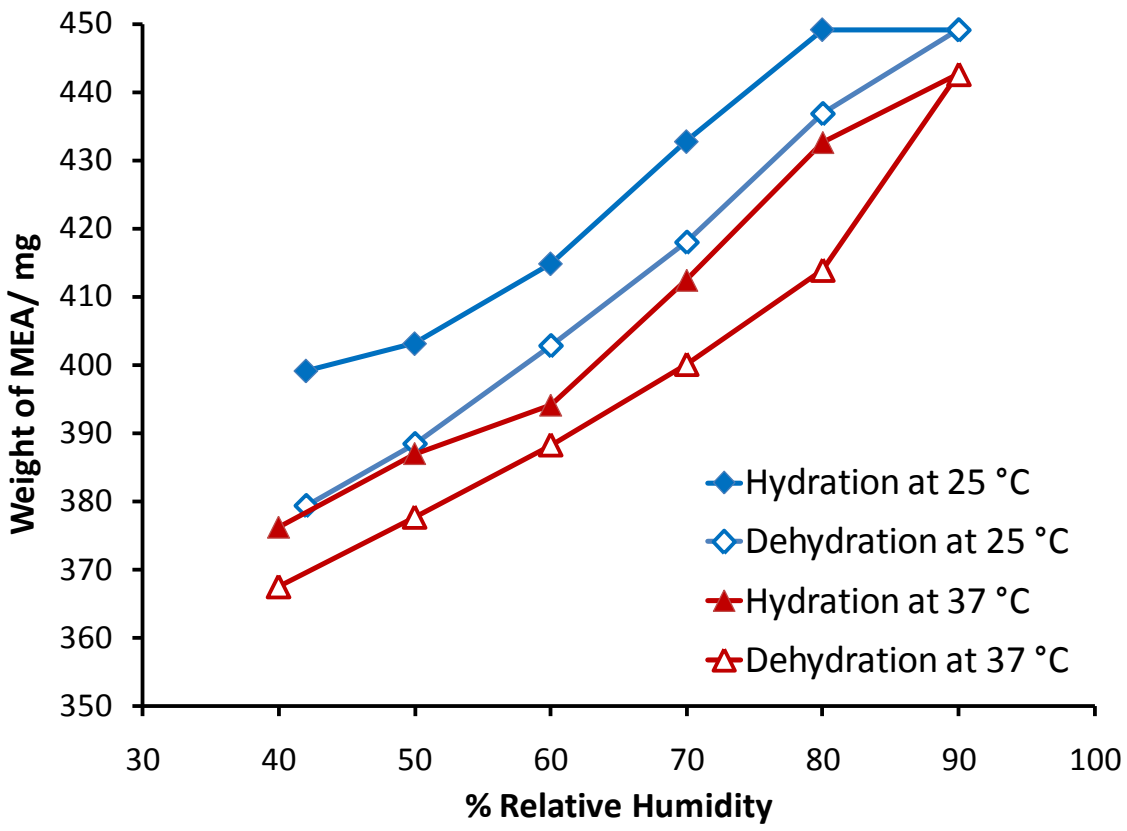

Figure 5.10: Weight of an MEA as the membrane was hydrated and dehydrated at constant temperature of 25 °C or 37 °C in a humidity chamber

During the 37 °C cycle, the MEA never reached the maximum level of hydration that was achieved between 80 and 90% RH during the first cycle. It was expected that at a given RH the membrane could absorb more water at a higher temperature. However, the previous hydration-dehydration cycle apparently caused a physical change in the membrane which reduced the amount of water that could be subsequently absorbed. We suspect there are small pores in the PVC membrane that filled with water by the process of capillary condensation during the first hydration phase (at 25°C). During the first dehydration phase the water in the small pores would exhibit a very large surface tension that could cause some of the pores to collapse as the water evaporates. Collapsed pores may be inaccessible to water in subsequent hydration processes, thereby reducing the overall volume available to hold water.

One more interesting feature is that there appears to be a change in the slope of the graph after 60% RH during the hydration phase of both cycles. The amount of water that can be added at each successive RH is larger at RH values greater than 60% than at RH values lower than 60%. This could be an indication of the average pore size in the membrane.

5.3.2 Ex-situ ECSA of Catalyst Material Removed from Fresh or Humidity-cycled MEAs

This study investigated how the ECSA of Pt in the sensor electrodes was affected by the accelerated humidity cycling performed in the previous experiment. The CVs for a series of ink deposits made using catalyst material from a fresh MEA and the humidity-cycled MEA that was tested in section 5.3.1 are shown in Figures 5.11 and 5.12 respectively. As the volume of ink deposited increases from 2 to 5 µL the size of the peaks in the hydrogen adsorption/desorption and Pt oxide regions increase as expected.

Figure 5.13 compares the CVs for the 2 µL ink deposit from the fresh and humidity-cycled MEAs. The hydrogen adsorption/desorption peaks are clearly larger in the CV for the fresh MEA indicating that the real surface area of Pt is larger in the catalyst ink made from the fresh MEA. The real surface area of Pt was calculated for each ink deposit using the area under the hydrogen desorption peak. These values were plotted against the mass of Pt in each ink deposit for both catalyst inks as shown in Figure 5.14. This takes into consideration the mass of catalyst material and volume of solvents used to prepare the ink. It is assumed that the catalyst material from both MEAs contained 90% Pt by weight, as previously determined by TGA using catalyst material from other MEAs.

A line of best fit was plotted for each MEA and the ECSA was given by the slope of the line. The humidity cycled MEA had a much lower ECSA (4.4 ± 0.7 m^2g^{-1}) than the fresh MEA (15.8 m^2g^{-1}). This suggests the process of hydrating and dehydrating the sensor in the humidity chamber greatly reduces the ECSA of Pt in the electrodes. Although the Pt was still present in the sensor, it became less catalytically active

because less of the Pt surface was accessible to reactants. This result is important because it indicates the primary cause of sensor degradation is loss of ECSA of Pt in the electrodes as a result of humidity cycling. The loss of ECSA was likely caused by an irreversible change in sensor morphology. SEM and TEM images should be obtained for sensors before and after humidity cycling to compare the Pt particle size and the morphology of the catalyst layer.

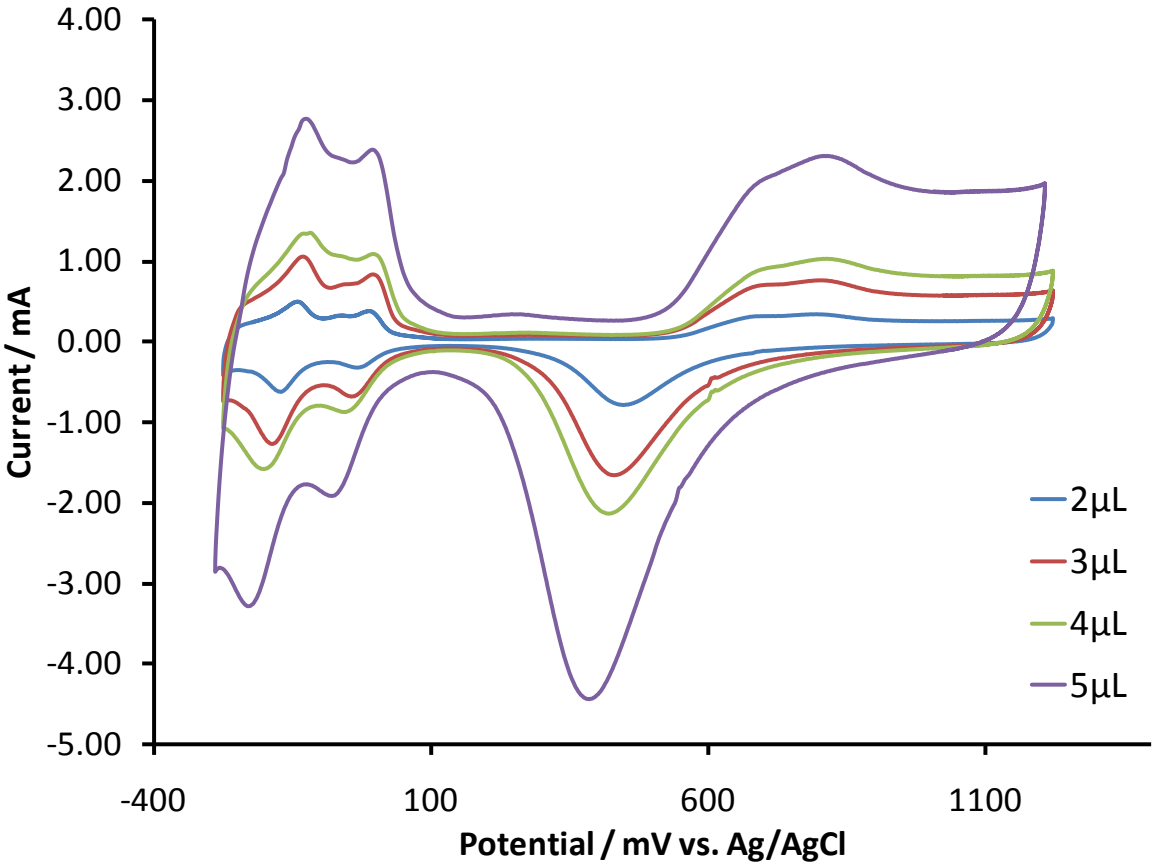

Figure 5.11: Half-cell cyclic voltammograms for catalyst ink made from fresh MEA

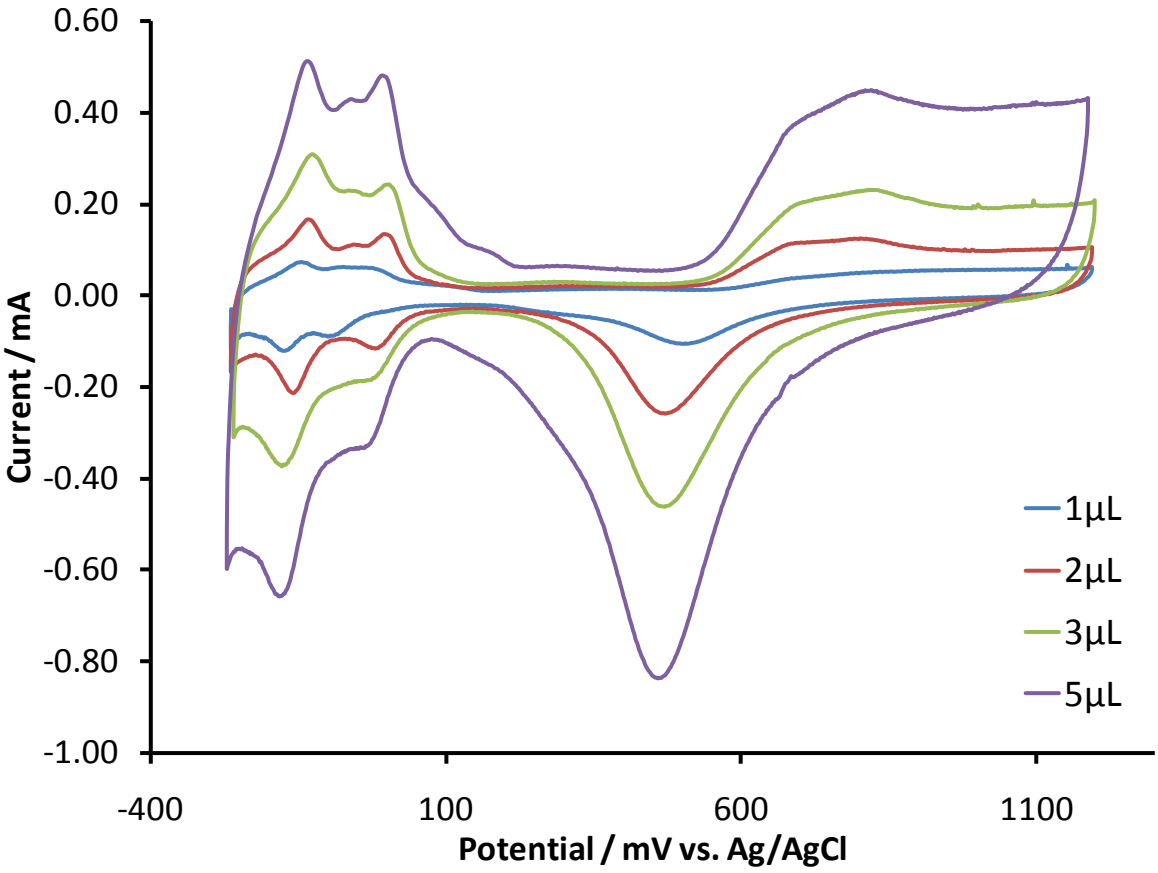

Figure 5.12: Half-cell cyclic voltammograms for catalyst ink made from humidity-cycled MEA

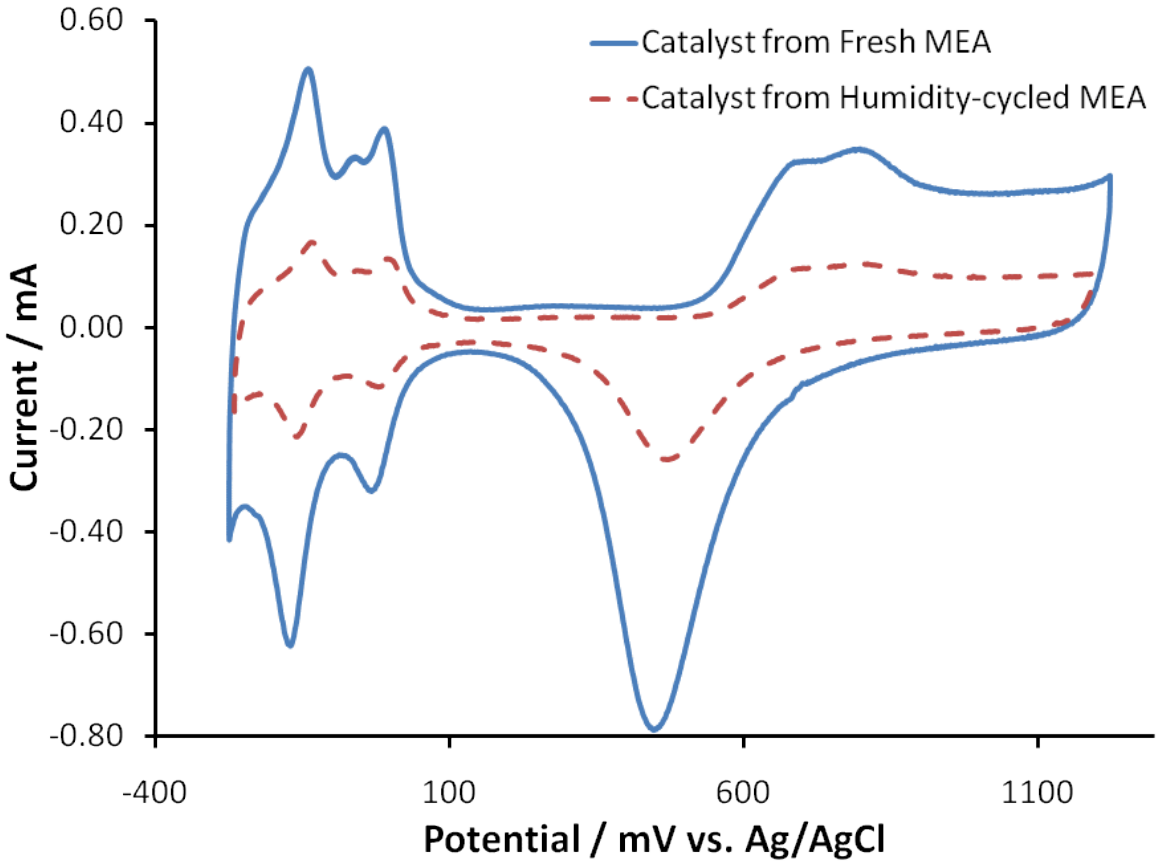

Figure 5.13: Half-cell cyclic voltammograms for 2µ L deposits of catalyst inks from fresh and humidity-cycled MEAs

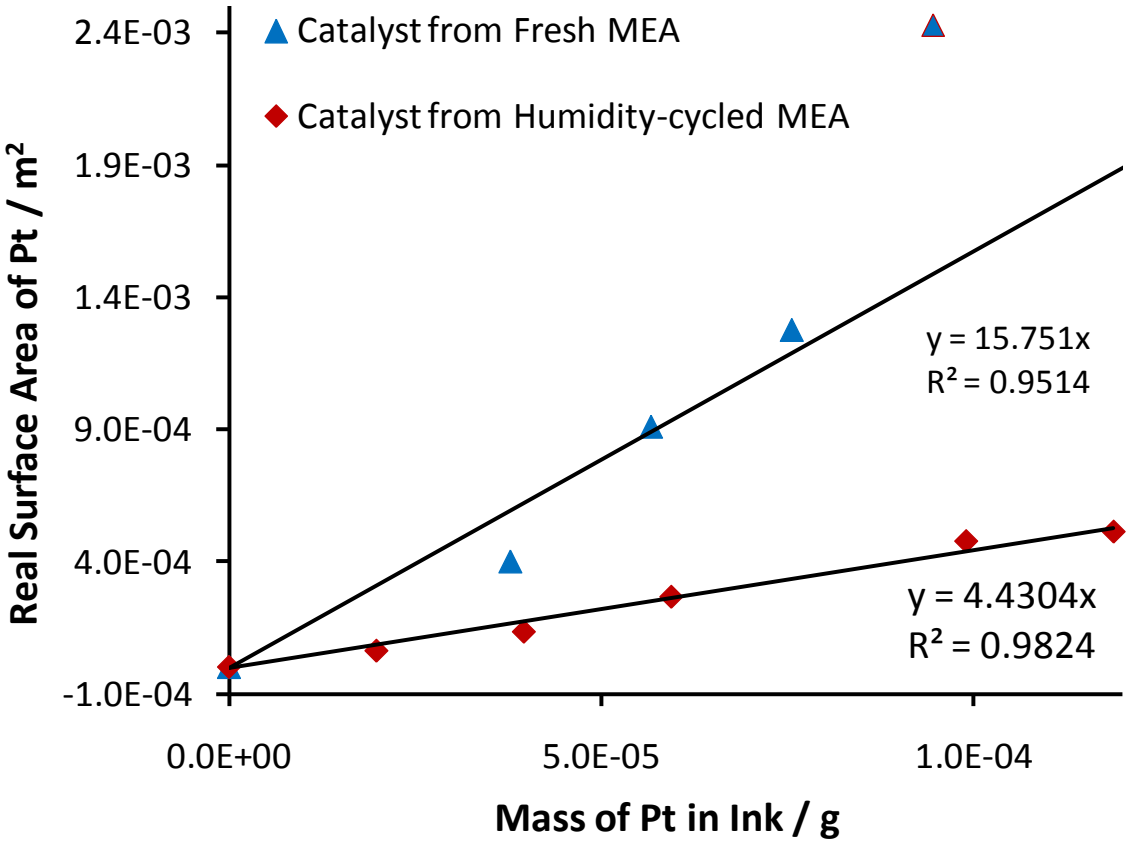

Figure 5.14: Determination of ECSA for catalyst from fresh and humidity-cycled sensors

5.4 Discussion of the Primary Cause of Sensor Degradation

The loss of ECSA of Pt in the electrodes was observed for an MEA that was removed from a sensor and equilibrated for 12 hours in controlled humidity conditions. In the previous studies, the MEA was not removed from the sensor cell. Rather, the intact sensor underwent accelerated humidity cycling and it was found that membrane conductivity and sensory performance are recoverable after the sensor has been exposed to short-term extremely dry conditions. In the studies using flowing N_2 the sensors were dehydrated and then immediately rehydrated. In the final study the sensors were constantly exposed to dehydrating conditions for 12 hours in a low-humidity environment before switching to a more humid setting. This longer-term exposure of the MEA to dry conditions seems to accelerate the sensor degradation much more than brief periods of extreme dehydration.

Poisoning of the Pt surface could cause a loss of ECSA.[57] However, loss of ECSA due to catalyst poisoning would not be observed in a half-cell cyclic voltammetry measurement because the adsorbed species would be oxidized as the applied potential is cycled between -280 mV and +1200 mV.[31] Even if the Pt surface was previously covered by adsorbed species, cyclic voltammetry has the effect of cleaning the catalyst surface. Therefore, the loss of ECSA is caused by some irreversible change to the electrodes.

Loss of ECSA has been reported for a power generating PEMFC after undergoing accelerated humidity cycling. The electrodes experienced a more than 40% loss of ECSA after undergoing 1200 cycles of alternating wet and dry gases. Each cycle consisted of flowing dry H_2 gas and air through the fuel cell for 20 min followed by wet H_2 gas and air for 5 min.[58] The loss of ECSA was due to delamination of the catalyst layer from the GDL and membrane. Delamination would reduce the three-phase boundary by reducing the amount of catalyst particles that are in contact with the PEM. A catalyst particle becomes inactive when it loses ionic contact with the membrane or ionomer. This could happen in breath alcohol sensors that experience a range of humidity.

The sensor PEM visibly swells when it becomes fully hydrated. Likewise, SEM imaging showed the PEM can contract and pull away from the catalyst layer when it dehydrates in vacuum conditions (Figure 3.4). As a PEM swells and contracts under changing humidity, it is likely that some delamination may occur between the membrane and electrodes. This would irreversibly decrease the ECSA of Pt in the electrodes. Delamination would also irreversibly increase the ionic resistance of the sensor by reducing ionic contact between the membrane and catalyst layer. The recoverability of membrane conductivity indicates delamination did not occurr to in-tact sensors during short-term exposure to dry conditions. However, delamination may have been the cause of reduced ECSA in sensors exposed to prolonged dry conditions and humidity cycling.

Chapter 6 – Conclusions and Future Directions

Commercially available breath alcohol sensors could be improved by taking advantage of some of the advances in standard materials for power generating fuel cells in the past 20 years. The Pt loadings could be reduced by half simply by replacing the Teflon-bonded Pt black electrodes with commercially available Pt nanoparticles supported on carbon black, such as E-Tek 20 wt.% Pt on Vulcan carbon XC-72. A carbon-supported catalyst would have a larger specific surface area and should reduce agglomeration of Pt particles. Agglomeration of Pt particles in the sensor electrodes severely limits the Pt utilization and ECSA of Pt. Also, Pt utilization and ECSA could be improved by adding a proton-conducting ionomer such as Nafion or a similar PFSA material to the catalyst layer. Bi-metallic Pt-Sn or other Pt alloy catalysts could be used in the sensor electrodes rather than Pt black. Pt alloy catalysts could reduce the risk of catalyst poisoning and promote more complete oxidation of ethanol to CO_2.[33] Increasing the number of electrons generated per oxidized ethanol molecule would increase the sensitivity toward ethanol.

The sulfuric acid-impregnated PVC membrane in the sensors has comparable proton conductivity to Nafion in hydrating conditions. Therefore, it is probably not necessary to replace the PVC membrane with a PFSA membrane to maximize proton conductivity.

Sensor lifetimes could be improved by mitigating sensor degradation in dry conditions. The membrane conductivity varies depending on the external environment, but any losses in proton conductivity caused by membrane dehydration can be easily recovered by rehydrating the membrane. Loss of ECSA after prolonged exposure to low-humidity is the primary cause of degradation in commercially available breath alcohol sensors. Therefore, the largest improvement to sensor lifetime would be achieved by using materials that reduce the impact of humidity on the ECSA of Pt in the electrodes. It was suggested that adding Nafion or a similar ionomer to the sensor catalyst layer would improve the ECSA of Pt. An ionomer could also help maintain ionic conductivity

between catalyst particles and the PEM while the PEM swells and contracts in varying humidity conditions.

An alternative membrane that retains water in low-humidity conditions without exhibiting substantial swelling in high-humidity could reduce the impact of humidity on sensor degradation. Composite Nafion-silica membranes have been proposed for their hygroscopic properties as well as for their good proton conductivity and lower ethanol crossover than Nafion.[16, 18, 23]

Future work in this area should involve development of new Pt-alloy catalysts and electrode structures for the next generation of fuel cell-based breath alcohol sensor. Similarly, standard membrane materials such as PFSA and sulfonated PEEK membranes will be investigated to replace the thick PVC membrane used in the existing sensor. Eventually the optimized electrodes will be combined with the new membrane to form an entirely new breath alcohol sensor. The sensor performance can be evaluated using dose response calibrations. The durability of the new sensor can be tested using accelerated humidity cycling and long-term exposure to dry conditions while monitoring the effects on ionic resistance of the membrane and ECSA of Pt in the electrodes.

Future research should also involve gaining a better understanding of the degradation of the existing sensor. It is apparent that the primary cause of sensor degradation is loss of ECSA rather than reduced proton conductivity. However, the exact mechanism of ECSA loss is unclear. Morphology changes in the membrane and electrodes causing delamination of the catalyst layer from the membrane is a proposed cause of sensor failure. Further studies should be performed to investigate this and other pathways of ECSA loss.

Future experiments should include in-situ cyclic voltammetry for MEAs still inside the sensor cells. This would allow ECSA to be monitored while dry or humidified N_2 gases are flowed through one side of the sensor cell. These measurements were attempted but were unsuccessful to date. Obtaining CVs for an MEA inside the sensor

cell requires modifications to the cell to enable gases to flow through both sides of the cell. N_2 gas should be flowed over the anode while H_2 gas is supplied to the cathode to provide a stable reference electrode. The N_2 gas flowing through the anode could be alternated between dry and humidified gas to perform accelerated humidity cycling. In-situ ECSA measurements would be superior to the ex-situ measurements performed in this study because the ECSA could be continuously monitored while the sensor is exposed to varying conditions. The ex-situ experiment using harvested catalyst material can only be performed once for a given MEA. As a result, the ECSA of a given electrode may not be compared with the ECSA of the same electrode under a different set of conditions.

Another future experiment involves performing a dose response calibration for a fresh sensor and then removing the MEA from the cell. The MEA will be equilibrated at low humidity for a prolonged period (more than 12 hours) in the humidity chamber. The MEA will then be re-assembled into the sensor cell and a second dose response calibration will be performed. This will give a comparison of sensitivity before and after long-term exposure of the MEA to dry conditions. Together, the results of these experiments will provide a better understanding of the primary degradation mechanism of the sensors in low-humidity environments. Development of the next generation of fuel cell-based breath alcohol sensors will incorporate materials and designs to overcome the shortcomings of the current sensor.

References

(1) Smith, W. C.; Harding, D. M.; Biasotti, A. A.; Finkle, B. S.; Bradford, L. W. Breathalyzer Experiences Under Operational Conditions Recommended by California Association of Criminalists. *Journal of the Forensic Science Society* **1969***, 9*, 58-&.

(2) Millet, P.; Michas, A.; Durand, R. A solid polymer electrolyte-based ethanol gas sensor. *J. Appl. Electrochem.* **1996***, 26*, 933-937.

(3) Wigmore, J. G.; Langille, R. M. Six Generations of Breath Alcohol Testing Instruments: Changes in the Detection of Breath Alcohol Since 1930. An Historical Overview. *Can. Soc. Forensic Sci. J.* **2009***, 42*, 276-283.

(4) Lucas, D. M.; Wigmore, J. G. Approved Screening Devices in Ontario. *JMVL* **1994***, 6*, 189-195.

(5) Chen, Y.; Chen, K. Y.; Tseung, A. C. C. An electrochemical alcohol sensor based on a co-electrodeposited Pt vertical bar WO3 electrode. *J Electroanal Chem* **1999***, 471*, 151-155.

(6) U.S. Department of Energy, Office of Fossil Energy In *Fuel Cell Handbook (Seventh Edition);* 2004; , pp 402.

(7) Bay, H. W.; Blurton, K. F.; Lieb, H. C.; Oswin, H. G. Electrochemical Measurements of Blood Alcohol Levels. *Nature* **1972***, 240*, 52-&.

(8) Rightmire, R. A.; Rowland, R. L.; Boos, D. L.; Beals, D. L. Ethyl Alcohol Oxidation at Platinum Electrodes. *J. Electrochem. Soc.* **1964***, 111*, 242-247.

(9) Kim, K. C.; Cho, S. M.; Choi, H. G. Detection of ethanol gas concentration by fuel cell sensors fabricated using a solid polymer electrolyte. *Sens. Actuator B-Chem.* **2000***, 67*, 194-198.

(10) Hickner, M. A.; Ghassemi, H.; Kim, Y. S.; Einsla, B. R.; McGrath, J. E. Alternative polymer systems for proton exchange membranes (PEMs). *Chem. Rev.* **2004***, 104*, 4587-4611.

(11) Elliott, J. A.; Paddison, S. J. Modelling of morphology and proton transport in PFSA membranes. *Phys. Chem. Chem. Phys.* **2007***, 9*, 2602-2618.

(12) Wilkinson, D. P.; Steck, A. E. In *General progress in the research of solid polymer fuel cell technology at Ballard;* Savadogo, O., Roberge, P. R., Eds.; ECOLE POLYTECHNIQUE MONTREAL: MONTREAL; C/O SERVICE EDITION CP 6079, SUCC CENTRE-VILLE, MONTREAL, QUEBEC H3C 3A7, CANADA, 1997; , pp 41.

(13) Drioli, E.; Regina, A.; Casciola, M.; Oliveti, A.; Trotta, F.; Massari, T. Sulfonated PEEK-WC membranes for possible fuel cell applications. *J. Membr. Sci.* **2004***, 228*, 139-148.

(14) Genies, C.; Mercier, R.; Sillion, B.; Cornet, N.; Gebel, G.; Pineri, M. Soluble sulfonated naphthalenic polyimides as materials for proton exchange membranes. *Polymer* **2001***, 42*, 359-373.

(15) Feng, S.; Voth, G. A. Proton Solvation and Transport in Hydrated Nafion. *J Phys Chem B* **2011***, 115*, 5903-5912.

(16) Rodgers, M. P.; Shi, Z.; Holdcroft, S. Transport properties of composite membranes containing silicon dioxide and Nafion (R). *J. Membr. Sci.* **2008***, 325*, 346-356.

(17) Tang, H.; Wan, Z.; Pan, M.; Jiang, S. P. Self-assembled Nafion-silica nanoparticles for elevated-high temperature polymer electrolyte membrane fuel cells. *Electrochem. Commun.* **2007***, 9*, 2003-2008.

(18) Yen, C.; Lee, C.; Lin, Y.; Lin, H.; Hsiao, Y.; Liao, S.; Chuang, C.; Ma, C. M. Sol-gel derived sulfonated-silica/Nafion (R) composite membrane for direct methanol fuel cell. *J. Power Sources* **2007***, 173*, 36-44.

(19) Ke, C.; Li, X.; Shen, Q.; Qu, S.; Shao, Z.; Yi, B. Investigation on sulfuric acid sulfonation of in-situ sol-gel derived Nafion/SiO2 composite membrane. *Int J Hydrogen Energy* **2011***, 36*, 3606-3613.

(20) Lin, Y.; Yen, C.; Ma, C. M.; Liao, S.; Lee, C.; Hsiao, Y.; Lin, H. High proton-conducting Nafion (R)/-SO3H functionalized mesoporous silica composite membranes. *J. Power Sources* **2007***, 171*, 388-395.

(21) Antolini, E. Catalysts for direct ethanol fuel cells. *J. Power Sources* **2007***, 170*, 1-12.

(22) Antolini, E.; Lopes, T.; Gonzalez, E. R. An overview of platinum-based catalysts as methanol-resistant oxygen reduction materials for direct methanol fuel cells. *J. Alloys Compounds* **2008***, 461*, 253-262.

(23) Ni, H.; Lv, C.; Zhang, C.; Liao, P. Preparation of Nafion/SiO2 Composite Membrane of Direct Ethanol Fuel Cell. *Functional Manufacturing Technologies and Ceeusro Ii* **2011***, 464*, 395-400.

(24) Sambandam, S.; Ramani, V. Influence of binder properties on kinetic and transport processes in polymer electrolyte fuel cell electrodes. *Phys. Chem. Chem. Phys.* **2010***, 12*, 6140-6149.

(25) Wilson, M. S.; Gottesfeld, S. High-Performance Catalyzed Membranes of Ultra-Low Pt Loadings for Polymer Electrolyte Fuel-Cells. *J. Electrochem. Soc.* **1992***, 139*, L28-L30.

(26) Poltarzewski, Z.; Staiti, P.; Alderucci, V.; Wieczorek, W.; Giordano, N. Nafion Distribution in Gas-Diffusion Electrodes for Solid-Polymer-Electrolyte-Fuel-Cell Applications. *J. Electrochem. Soc.* **1992***, 139*, 761-765.

(27) Esparbe, I.; Brillas, E.; Centellas, F.; Antonio Garrido, J.; Maria Rodriguez, R.; Arias, C.; Cabot, P. Structure and electrocatalytic performance of carbon-supported platinum nanoparticles. *J. Power Sources* **2009***, 190*, 201-209.

(28) Gode, P.; Jaouen, F.; Lindbergh, G.; Lundblad, A.; Sundholm, G. Influence of the composition on the structure and electrochemical characteristics of the PEFC cathode. *Electrochim. Acta* **2003***, 48*, 4175-4187.

(29) Antolini, E.; Giorgi, L.; Pozio, A.; Passalacqua, E. Influence of Nafion loading in the catalyst layer of gas-diffusion electrodes for PEFC. *J. Power Sources* **1999***, 77*, 136-142.

(30) Shi, J.; Li, X.; Hu, Y.; Hua, Y. Electro-deposition of platinum nanoparticles on 4-mercaptobenzene-functionalized multi-walled carbon nanotubes. *J. Solid State Electrochem.* **2008***, 12*, 1555-1559.

(31) Vigier, F.; Coutanceau, C.; Hahn, F.; Belgsir, E. M.; Lamy, C. On the mechanism of ethanol electro-oxidation on Pt and PtSn catalysts: electrochemical and in situ IR reflectance spectroscopy studies. *J Electroanal Chem* **2004***, 563*, 81-89.

(32) Vigier, F.; Coutanceau, C.; Perrard, A.; Belgsir, E. M.; Lamy, C. Development of anode catalysts for a direct ethanol fuel cell. *J. Appl. Electrochem.* **2004***, 34*, 439-446.

(33) Vigier, F.; Rousseau, S.; Coutanceau, C.; Leger, J.; Lamy, C. Electrocatalysis for the direct alcohol fuel cell. *Top. Catal.* **2006***, 40*, 111-121.

(34) Fatih, K.; Neburchilov, V.; Alzate, V.; Neagu, R.; Wang, H. Synthesis and characterization of quaternary PtRuIrSn/C electrocatalysts for direct ethanol fuel cells. *J. Power Sources* **2010***, 195*, 7168-7175.

(35) Vogel, W. M.; Lundquis.Jt Reduction of Oxygen on Teflon-Bonded Platinum Electrodes. *J. Electrochem. Soc.* **1970***, 117*, 1512-&.

(36) Easton, E. B.; Pickup, P. G. An electrochemical impedance spectroscopy study of fuel cell electrodes. *Electrochim. Acta* **2005***, 50*, 2469-2474.

(37) Taguchi, T.; Inagaki, H.; Atsumi, B.; Kimura, K. Study of breath alcohol detector. *JSAE Review* **1994**, 229-233.

(38) Slade, S.; Campbell, S. A.; Ralph, T. R.; Walsh, F. C. Ionic conductivity of an extruded Nafion 1100 EW series of membranes. *J. Electrochem. Soc.* **2002***, 149*, A1556-A1564.

(39) Holze, R.; Maas, A. On the Microstructure of Teflon-Bonded Platinum Carbon Electrodes. *J. Appl. Electrochem.* **1983***, 13*, 549-551.

(40) Patterson, A. L. The Scherrer formula for x-ray particle size determination. *Phys. Rev.* **1939***, 56*, 978-982.

(41) *http://www.hydrogen.energy.gov/pdfs/review04/fc_47_zelenay.pdf*.

(42) *http://www.chemicals.matthey.com/userfiles/files/Pt(1).pdf* (accessed 07/04, 2011).

(43) Anderson, M. L.; Stroud, R. M.; Rolison, D. R. Enhancing the activity of fuel-cell reactions by designing three-dimensional nanostructured architectures: Catalyst-modified carbon-silica composite aerogels. *Nano Lett.* **2002***, 2*, 235-240.

(44) Boettner, E. A.; Ball, G.; Weiss, B. Analysis of Volatile Combustion Products of Vinyl Plastics. *J Appl Polym Sci* **1969***, 13*, 377-&.

(45) Omara, M. M. Combustion of Pvc. *Pure Appl. Chem.* **1977***, 49*, 649-660.

(46) Sun, Z.; Chiu, H. C.; Tseung, A. C. C. Oxygen reduction on teflon bonded Pt/WO3/C electrode in sulfuric acid. *Electrochem. Solid State Lett.* **2001***, 4*, E9-E12.

(47) Ohyagi, S.; Matsuda, T.; Iseki, Y.; Sasaki, T.; Kaito, C. Effects of operating conditions on durability of polymer electrolyte membrane fuel cell Pt cathode catalyst layer. *J. Power Sources* **2011***, 196*, 3743-3749.

(48) Seah, M. P.; Gilmore, I. S.; Spencer, S. J. XPS: Binding energy calibration of electron spectrometers 4 - Assessment of effects for different x-ray sources, analyser resolutions, angles of emission and overall uncertainties. *Surf Interface Anal* **1998***, 26*, 617-641.

(49) *http://srdata.nist.gov/xps/* (accessed 05/20, 2011).

(50) Arico, A. S.; Shukla, A. K.; Kim, H.; Park, S.; Min, M.; Antonucci, V. An XPS study on oxidation states of Pt and its alloys with Co and Cr and its relevance to electroreduction of oxygen. *Appl. Surf. Sci.* **2001***, 172*, 33-40.

(51) Liu, H.; Zhang, H.; Chen, J. Surface analysis of long-distance oxygen plasma sterilized PTFE film. *Appl. Surf. Sci.* **2009***, 255*, 8115-8121.

(52) Conesa, J. A.; Font, R. Polytetrafluoroethylene decomposition in air and nitrogen. *Polym. Eng. Sci.* **2001***, 41*, 2137-2147.

(53) Liang, C. Y.; Krimm, S. Infrared Spectra of High Polymers .3. Polytetrafluoroethylene and Polychlorotrifluoroethylene. *J. Chem. Phys.* **1956***, 25*, 563-571.

(54) Trasatti, S.; Petrii, O. A. Real Surface-Area Measurements in Electrochemistry. *Pure Appl. Chem.* **1991***, 63*, 711-734.

(55) Lee, S. J.; Mukerjee, S.; McBreen, J.; Rho, Y. W.; Kho, Y. T.; Lee, T. H. Effects of Nafion impregnation on performances of PEMFC electrodes. *Electrochim. Acta* **1998***, 43*, 3693-3701.

(56) Rieke, P. C.; Vanderborgh, N. E. Temperature-Dependence of Water-Content and Proton Conductivity in Polyperfluorosulfonic Acid Membranes. *J. Membr. Sci.* **1987***, 32*, 313-328.

(57) Travitsky, N.; Burstein, L.; Rosenburg, Y.; Peled, E. Effect of methanol, ethylene glycol and their oxidation by-products on the activity of Pt-based oxygen-reduction catalysts. *J. Power Sources* **2009***, 194*, 161-167.

(58) Kang, J.; Kim, J. Membrane electrode assembly degradation by dry/wet gas on a PEM fuel cell. *Int J Hydrogen Energy* **2010***, 35*, 13125-13130.